Title	Multifunctional 19F MRI Contrast Agents Based on Core-shell Fluorine-encapsulated Silica Nanoparticles
Author(s)	松下, 尚嗣
Citation	大阪大学, 2014, 博士論文
Version Type	VoR
URL	https://doi.org/10.18910/34432
rights	
Note	

Doctoral Dissertation

Multifunctional ^{19}F MRI Contrast Agents Based on Core-shell Fluorine-encapsulated Silica Nanoparticles

Hisashi Matsushita

January 2014

Laboratory of Chemical Biology
Division of Advanced Science and Biotechnology
Graduate School of Engineering
Osaka University

Contents

List of Abbreviations

ACLE·HCl	7-Amino-3-chloromethyl-3-cephem-4-carboxylic acid *p*-methoxybenzyl ester hydrochloride
APTES	3-Aminopropyltriethoxysilane
BET	Brunauer–Emmett–Teller
CEST	Chemical exchange saturation transfer
CLSM	Confocal laser scanning microscopy
CT	Computed tomography
CTAB	*n*-Cetylammonium bromide
Cys	Cysteine
DLS	Dynamic light scattering
DMEM	Dulbecco’s modified Eagle medium
DMF	*N*,*N*-dimethylformamide
DOX	Doxorubicin
DSPC	Distearoyl-*sn*-glycero-3-phosphocholine
DTPA	Diethylene-triamine-pentaacetic acid
DTT	Dithiothreitol
EDTA	Ethylenediaminetetraacetic acid
EGFR	Epidermal growth factor receptor
EPR	Enhanced permeability and retention
ESI-MS	Electrospray ionization mass spectrometry
Endo	Endogenous
Exo	Exogeneous
FBS	Fetal bovine serum
FITC-FA	Fluorescein isothiocyanate-folic acid
FLAME	Fluorine accumulated silica nanoparticle for MRI contrast enhancement
FMT	Fluorescence molecular tomography
FOV	Field of view
GSH	Glutathione
HEK	Human embryonic kidney
HOBt	1-Hydroxybenzotriazole
ICP-MS	Inductively coupled plasma mass spectrometry
MBP	Maltose-binding protein

MION	Monocrystalline iron oxide nanoparticle
MRI	Magnetic resonance imaging
MRS	Magnetic resonance spectroscopy
MRSI	Magnetic resonance spectroscopy imaging
MSNs	Mesoporous silica nanoparticles
MTT	3-(4,5-dimethylthiazol-2-yl)-2,5-diphenyltetrazolium bromide
NA	Number of accumulations
NMM	*N*-Methylmorpholine
NMR	Nuclear magnetic resonance
ODS	Octadecyl silane
PBS	Phosphate-buffered saline
PEG	Polyethylene glycol
PET	Positron emission tomography
PFCE	Perfluoro-15-crown-5 ether
PFCs	Perfluorocarbons
PFONPG	4-Fluoro-2-nitrophenyl-β-D-galactopyranoside
PRE	Paramagnetic relaxation enhancement
PolyP	Polyphosphoric acid
RARE	Rapid acquisition with refocused echoes
RES	Reticuloendothelial system
RITC	Rhodamine B isothiocyanate
RP-HPLC	Reversed-phase high-performance liquid chromatography
RT	Room temperature
SPECT	Single photon emission computed tomography
SPIO	Superparamagnetic iron oxide
TBST	Tris-buffered saline and Tween 20
TCEP	Tris(2-carboxyethyl)phosphine
TEA	Triethylamine
TEM	Transmission electron microscopy
TEOS	Tetraethyl orthosilicate
WSCD	Water-soluble carbodiimide
mFLAME	Mesoporous FLAME
α-Gal	α-Galactosidase
β-Gal	β-Galactosidase
β-Glu	β-Glucuronidase
β-Lac	β-Lactamase

General Introduction

In vivo imaging techniques

The animal body is composed of a multitude of substances such as proteins, metal ions, and small molecules. These numerous biomolecules interact with each other to maintain the living system.[1–3] It is important to accurately determine their spatiotemporal interaction patterns for the development of new medical treatments, development of diagnostic methods, and discovery of pharmaceuticals.[4–9]

Molecular imaging is capable of direct visualization of molecular functions in living organisms. Fluorescence imaging with fluorescent proteins and fluorescent molecules is a powerful tool to monitor the molecular functions and interactions at the cellular level because of its high sensitivity and simplified determination.[10–14] However, the poor transmission of fluorescence limits in vivo applications. Thus, several in vivo imaging techniques are widely used to monitor biological phenomena in deep tissue (Table 1).[15] MRI is a method that can solve this problem because it yields high-resolution images of deep regions of living animal bodies without using radioactivity.[16–18] Therefore, MRI is currently considered as one of the most promising techniques for in vivo investigation of physiological events.[19–21]

Table 1. Overview of in vivo imaging systems.

Technique	Resolution	Depth	Imaging agents
MRI	10–100 µm	No limit	Paramagnetic chelates, magnetic particles
CT	50 µm	No limit	Iondinated molecules
Ultrasound	50 µm	cm	Microbubbles
PET	1–2 mm	No limit	Radioactive compounds (^{18}F, ^{64}Cu or ^{11}C)
SPECT	1–2 mm	No limit	Radioactive compounds (^{99m}Tc or ^{111}In)
Fluorescence reflectance imaging	2–3 mm	<1 cm	Fluorescent proteins, fluorochromes
FMT	1 mm	<10 cm	Near-infrared fluorochromes
Bioluminescence imaging	Several mm	cm	Luciferins
Intravital microscopy	1 µm	<400–800 µm	Photoproteins, fluorochormes

^{1}H MRI

MRI is an imaging technique based on NMR technology. In clinical ^{1}H MRI, protons of water molecules and fatty acid are observed. The characteristics of their MRI signals are dependent on the fluidity of protons and other components, which have a strong effect on the longitudinal relaxation time (T_1) and the transverse relaxation time (T_2), thus strongly affecting the MRI contrast. Clinical MRI contrast agents dramatically shorten the T_1 and T_2 of protons, resulting in enhanced or reduced the MRI signal intensity (Figure 1).[20,22–29]

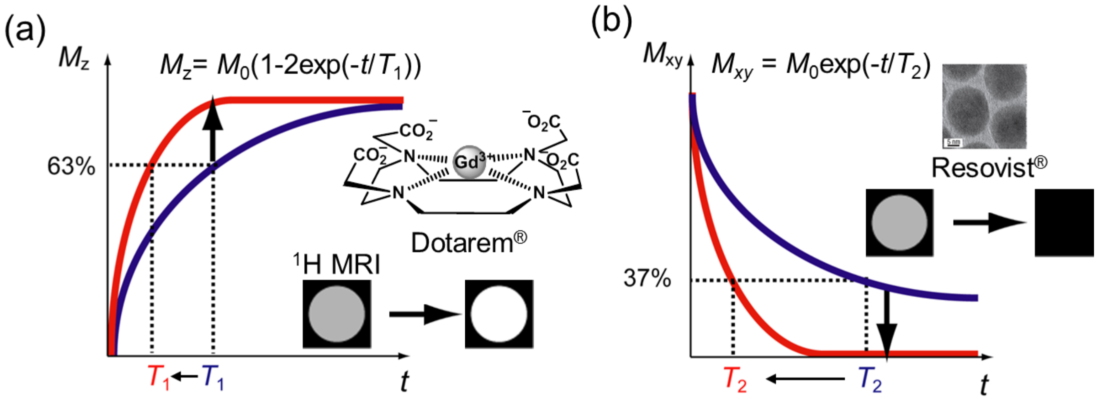

Figure 1. (a) The longitudinal relaxation time (T_1), (b) the transverse relaxation time (T_2), and MRI signal intensity in the presence (red line) or absence (blue line) of a clinical MRI contrast agent.

A milestone functional ^{1}H MRI probe for the detection of reporter enzyme activity was reported by Meade *et al.* (Figure 2),[30] who developed a ^{1}H MRI probe that can visualize gene expression by detecting β-gal activity. When the probe is hydrolyzed by β-gal, the coordination of water to Gd^{3+} is enhanced. Because an increase in the coordination

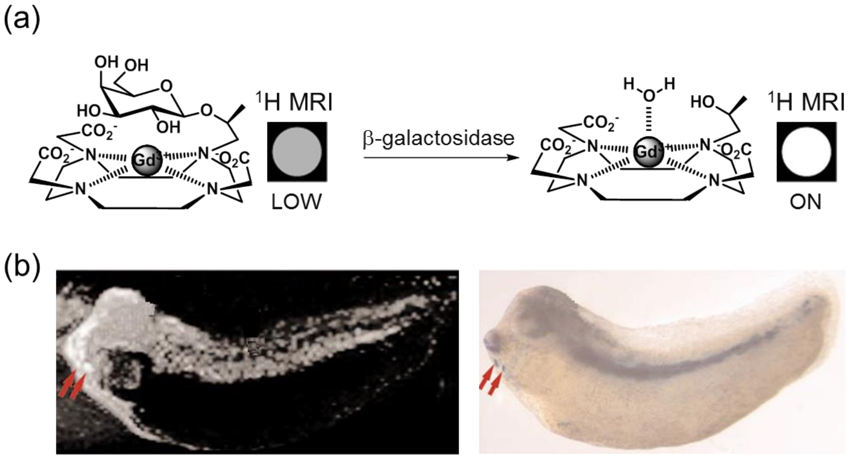

Figure 2. (a) Schematic representation of the transition of an ^{1}H MRI probe from a weak to a strong relaxivity state. (b) (left) MRI of a living embryo expressing β-galactosidase treated with an ^{1}H MRI probe. (left) Bright-field image of the same embryo fixed and stained with X-gal, which is a staining dye for β-gal.

number of water molecules induces ^{1}H MRI signal enhancement, the ^{1}H MRI signal of the probe is increased by β-gal activity. In principle, however, such ^{1}H MRI signal enhancement needs to be discriminated from the background ^{1}H MRI signals of water, fatty acids, and other biomolecules.

^{19}F MRI

To avoid limitation by background signals, the author has focused on the use of ^{19}F MRI. Fluorine (^{19}F) has a high gyromagnetic ratio (γ) of 40.05 MHz·T^{-1} and a 100% natural isotopic abundance ratio (Table 2).[31–36] Thus, ^{19}F MRI has relatively high sensitivity corresponding to 83% of ^{1}H. Although fluorine atoms are concentrated in the form of solid salts mostly in bones and teeth, almost no intrinsic ^{19}F MRI signals can be observed in living animals because of the extremely short T_2 of fluorine atoms in solid state. Thus, ^{19}F MRI can be used to reduce the intrinsic background signal (Figure 3).[37]

Table 2. Main target nuclei and sensitivity

Nuclei	Resonant frequency (MHz T^{-1})	Relative sensitivity	Natural isotopic abundance ratio (%)	NMR sensitivity
^{1}H	42.58	1	99.985	1
^{13}C	10.71	1.59×10^{-2}	1.108	1.76×10^{-4}
^{15}N	4.31	1.04×10^{-3}	0.37	3.85×10^{-6}
^{19}F	40.05	8.33×10^{-1}	100	8.33×10^{-1}
^{29}Si	8.46	7.83×10^{-3}	4.7	3.69×10^{-4}
^{31}P	17.24	6.63×10^{-2}	100	6.63×10^{-2}
^{129}Xe	11.78	2.12×10^{-2}	26.4	5.60×10^{-3}

^{19}F MRI probes that can visualize biological functions have been increasingly reported. As shown in Figure 4, ^{19}F MRI probes are categorized into several groups: (1) fluorine-containing functional compounds that accumulate in specific sites (Figure 4a),[38] (2) nanoemulsions including perfluorocarbon for cell tracking (Figure 4b),[37,39–42] (3) T_2-based ^{19}F MRI probes (Figure 4c, d, e),[43–46] and (4) chemical shift-based ^{19}F MRI probes (Figure 4f).[36,47,48]

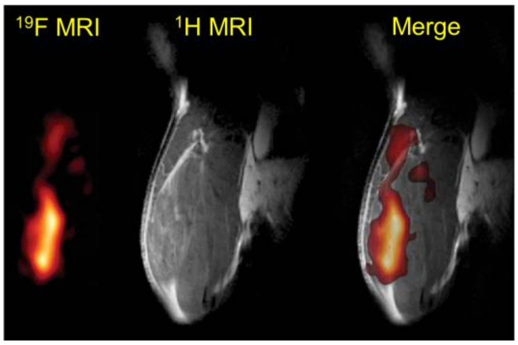

Figure 3. In vivo MRI of mouse quadriceps after intramuscular injection of fluorine-labeled dendritic cells. The ^{19}F intensity is displayed on a ‘hot-iron’ intensity scale, and the ^{1}H images are shown in gray scale.

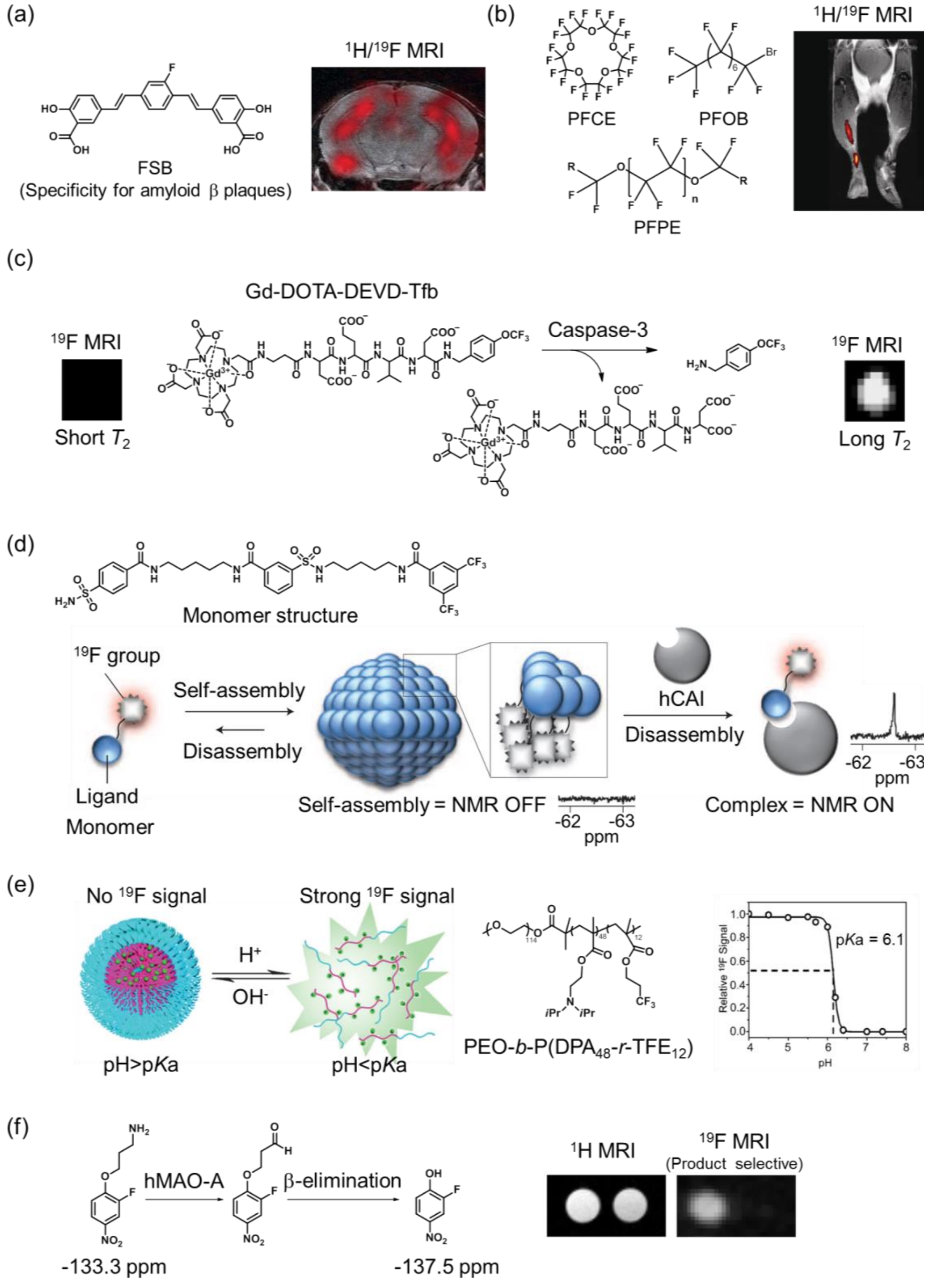

Figure 4. Smart ^{19}F MRI probes for monitoring biological phenomena. (a) ^{19}F-containing compound (FSB) that specifically labels amyloid β plaques in the brain. (b) The chemical structure of PFCs. In vivo ^{19}F MRI cell tracking with immune cells that were labeled by nanoemulsions including PFCs. (c) Paramagnetic relaxation-based ^{19}F MRI probe to detect protease activity. (d) Self-assembling ^{19}F NMR nanoprobe for protein imaging. (e) pH-activatable ^{19}F MRI nanoprobe (f) Chemical shift-based ^{19}F MRI probe for specific detection of human monoamine oxidase A.

Purpose of research

Imaging of gene expression provides us various types of information such as the expression timing of target proteins, gene transfer efficiency, and detection of disease-related gene expression. To monitor gene expression by various methods, reporter proteins are useful.[10,19] The author attempted to develop an ^{19}F MRI probe for visualizing gene expression in vivo. In the author's research group, an OFF/ON design strategy for ^{19}F MRI probes had been constructed based on the intramolecular PRE effect for modulation of T_2 of fluorine by protease activity (Figure 5).[43,44] By utilizing this probe principle, the author here reports novel ^{19}F MRI probes that detect cellular gene expression via β-gal and β-lac, which are widely used as reporter proteins (Chapter 1).

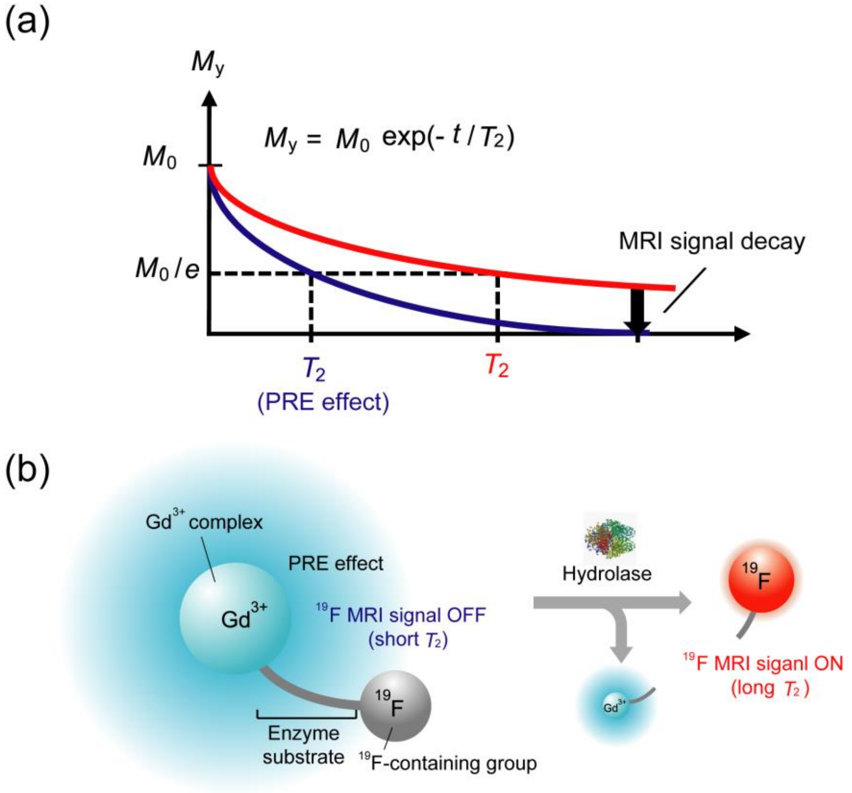

Figure 5. (a) Decay of transverse magnetization in the presence of the PRE effect. (b) PRE-based ^{19}F MRI probe for monitoring enzyme activity.

Although ^{19}F MRI detection of cellular gene expression in live cells was demonstrated by using ^{19}F probes for cell-surface-displayed β-lactamase, unsolved problems for in vivo imaging remained such as the potential diffusion of the activated probes. To overcome this limitation, the author focused on mutant β-lactamase (BL-tag). The BL-tag solves the problem of diffusion of the activated probe because it covalently binds to the ^{19}F MRI probe, which has a β-lactam ring moiety. However, no ^{19}F signal was detected from ^{19}F-labeled cells because of the low sensitivity of the ^{19}F MRI probe and the shortening of T_2 by the suppression of molecular mobility. Thus, the author developed core-shell fluorine-encapsulated silica nanoparticles to solve these limitations simultaneously (Chapter 2). The author demonstrated superior properties of these nanoparticles for ^{19}F MRI such as high sensitivity, stability, surface modifiability, and biocompatibility, together with biomedical applications such as reporter assays and in vivo tumor imaging. In Chapter 3, the PRE-based probe design and a highly sensitive ^{19}F MRI contrast agent are combined for development of a ^{19}F MRI nanoprobe. In the last chapter, the author describes a multifunctional ^{19}F MRI-traceable drug carrier, which is a useful candidate for cancer theragnosis.

References

1. Devasagayam, T. P. A.; Tilak, J. C.; Boloor, K. K.; Sane, K. S.; Ghaskadbi, S. S.; Lele, R. D. *J. Assoc. Physicians India* **2004**, *52*, 794–804.
2. Bao, G.; Suresh, S. *Nat. Mater.* **2003**, *2*, 715–725.
3. Fritz, J.; Baller, M. K.; Lang, H. P.; Rothuizen, H.; Vettiger, P.; Meyer, E.; Güntherodt, H.-J.; Gerber, C.; Gimzewski, J. K. *Science* **2000**, *288*, 316–318.
4. Albert, K. G. M. M.; Zimmet, P.; Shaw, J. *Diabet. Med.* **2006**, *23*, 469–480.
5. Marx, R. E.; Sawatari, Y.; Fortin, M.; Broumand, V. *J. Oral Maxillofac. Surg.* **2005**, *63*, 1567–1575.
6. Mammen, M.; Choi, S.-K.; Whitesides, G. M. *Angew. Chem. Int. Ed.* **2010**, *30*, 2754–2794.
7. Kumar, M. N. V. R.; Muzzarelli, R. A. A.; Muzzarelli, C.; Sashiwa, H.; Domb, A. J. *Chem. Rev*. **2004**, *104*, 6017–6084.
8. Fabian, M. A.; Biggs, W. H.; Treiber, D. K.; Atteridge, C. E.; Azimioara, M. D.; Benedetti, M. G.; Carter, T. A.; Ciceri, P., Edeen, P. T.; Floyd, M.; Ford, J. M.; Galvin, M.; Gerlach, J. L.; Grotzfeld, R. M.; Herrgard, S.; Insko, D. E.; Insko, M. A.; Lai, A. G.; Lélias, J.-M.; Mehta, S. A.; Milanov, Z. V.; Velasco, A. M.; Wodicka, L. M.; Patel, H. K.; Zarrinkar, P. P.; Lockhart, D. J. *Nat. Biotechnol.* **2005**, *23*, 329–336.
9. Koehn, F. E.; Carter, G. T. *Nat. Rev. Drug Discov.* **2005**, *4*, 206–220.
10. Chalfie, M.; Tu, Y.; Euskirchen, G.; Ward, W. W.; Prasher D. C. *Science* **1994**, *263*, 802–805.
11. Miyawaki, A.; Llopis, J.; Heim, R.; Mccaffery, J. M.; Adams, J. A.; Ikura, M.; Tsien, R. Y. *Nature* **1997**, *388*, 882–887.

12. Weiss, S. *Science* **1999**, *283*, 1676–1683.
13. Luo, S.; Zhang, E.; Su, Y.; Cheng, T.; Shi, C. *Biomaterials 2011*, **32**, 7127–7138.
14. Zhang, J.; Campbell, R. E.; Ting, A. Y.; Tsien, R. Y. *Nat. Rev. Mol. Cell Biol.* **2002**, *3*, 906–918.
15. Weissleder, R.; Pittet, M. J. *Nature* **2008**, *452*, 580–589.
16. Jasanoff, A. *Curr. Opin. Neurobiol.* **2007**, *17*, 593–600.
17. Stasiuk, G. J.; Smith, H.; Wylezinska-Arridge, M.; Tremoleda, J. L.; Trigg, W., Luthra, S. K.; Iveson, V. M.; Gavins, F. N. E.; Long, N. J. *Chem. Commun.* **2013**, *49*. 564–566.
18. McDonald, D. M.; Choyke, P. L. *Nat. Med.* **2003**, *9*, 713–725.
19. Weissleder, R.; Moore, A.; Mahmood, U.; Bhorade, R.; Benveniste, H.; Chiocca, E. A.; Basilion, J. P. *Nat. Med.* **2000**, *6*, 351–355.
20. Caravan, P. *Chem. Soc. Rev.* **2006**, *35*, 512–523.
21. Amirbekian, V.; Lipinski, M. J.; Briley-Saebo, K. C.; Amirbekian, S.; Aguinaldo, J. G. S.; Weinreb, D. B.; Vucic, E.; Frias, J. C.; Hyafil, F.; Mani, V.; Fisher, E. A; Fayad, Z. A. *Proc. Natl. Acad. Sci. U. S. A.* **2007**, *104*, 961–966.
22. Lauffer, R. B. *Chem. Rev.* **1987**, *87*, 901–927.
23. Jun, Y.; Lee, J.-H.; Cheon, J. *Angew. Chem. Int. Ed.* **2008**, *47*, 5122–5135.
24. Bulte, J. W. M.; Kraitchman, D. L. *NMR Biomed.* **2004**, *17*, 484–499.
25. Lee, J.-H.; Huh, Y.-M.; Jun, Y.; Seo, J.; Jang, J.; Song, H.-T.; Kim, S.; Cho, E.-J.; Yoon, H.-G.; Suh, J.-S.; Cheon, J. *Nat. Med.* **2007**, *13*, 95–99.
26. Luo, K.; Liu, G.; She, W.; Wang, Q.; Wang, G.; He, B.; Ai, H.; Gong, Q.; Song, B.; Gu, Z. *Biomaterials* **2011**, *32*, 7951–7960.
27. Feshitan, J. A; Vlachos, F.; Sirsi, S. R.; Konofagou, E. E.; Borden, M. A. *Biomaterials* **2012**, *33*, 247–255.
28. Tu, C.; Osborne, E. A.; Louie, A. Y. *Ann. Biomed. Eng.* **2011**, *39*, 1335–1348.
29. Mornet, S.; Vasseur, S.; Grasset, F.; Duguet, E. *J. Mater. Chem.* **2004**, *14*, 2161–2175.
30. Louie, A. Y.; Hüber, M. M.; Ahrens, E. T.; Rothbächer, U.;Moats, R.; Jacobs, R. E.; Fraser, S. E.; Meade. T. J. *Nat. Biotechnol.* **2000**, *18*, 321–325.
31. Ruiz-Cabello, J.; Barnett, B. P.; Bottomley, P. A.; Bulte, J. W. M. *NMR Biomed.* **2011**, *2*, 114–129.
32. Partlow, K. C.; Chen, J.; Brant, J. A.; Neubauer, A. M.; Meyerrose, T. E.; Creer, M. H.; Nolta, J. A.; Caruthers, S. D.; Lanza, G. M.; Wickline, S. A. *FASEB J.* **2007**, *21*, 1647–1654.
33. Janjic, J. M.; Srinivas, M.; Kadayakkara, D. K. K.; Ahrens, E. T. *J. Am. Chem. Soc.*

2008, *130*, 2832–2841.

34. Crull, G. B.; Kennington, J. W.; Garber, A. R.; Ellis, P. D.; Dawson, J. H. *J. Biol. Chem.* **1989**, *264*, 2649–2655.
35. Wolf, W.; Presant, C. A.; Waluch, V. *Adv. Drug Deliv. Rev.* **2000**, *41*, 55–74.
36. Cui, W.; Otten, P.; Li, Y.; Koeneman, K. S.; Yu, J.; Mason, R. P. *Magn. Reson. Med.* **2004**, *51*, 616–620.
37. Ahrens, E. T.; Flores, R.; Xu, H.; Morel, P. A. *Nat. Biotechnol.* **2005**, *23*, 983–987.
38. Higuchi, M.; Iwata, N.; Matsuba, Y.; Sato, K.; Sasamoto, K.; Saido, T. C. *Nat. Neurosci.* **2005**, *8*, 527–533.
39. Mason, R. P.; Antich, P. P.; Babcock, E. E.; Gerberich, J. L.; Nunnally, R. L. *Magn. Reson. Imaging* **1989**, *7*, 475–485.
40. Díaz-López, R.; Tsapis, N.; Fattal, E. *Pharm. Res*. **2010**, *27*, 1–16.
41. Diou, O.; Tsapis, N.; Giraudeau, C.; Valette, J.; Gueutin, C.; Bourasset, F.; Zanna, S.; Vauthier, C.; Fattal, E. *Biomaterials* **2012**, *33*, 5593–5602.
42. Flögel, U.; Ding, Z.; Hardung, H.; Jander, S.; Reichmann, G.; Jacoby, C.; Schubert, R.; Schrader, J. *Circulation* **2008**, *118*, 140–148.
43. Mizukami, S.; Takikawa, R.; Sugihara, F.; Hori, Y.; Tochio, H.; Wälchli, M.; Shirakawa, M.; Kikuchi, K. *J. Am. Chem. Soc.* **2008**, *130*, 794–795.
44. Mizukami, S.; Takikawa, R.; Sugihara, F.; Shirakawa, M.; Kikuchi, K. *Angew. Chem. Int. Ed.* **2009**, *48*, 3641–3643.
45. Takaoka, Y.; Sakamoto, T.; Tsukiji, S.; Narazaki, M.; Matsuda, T.; Tochio, H.; Shirakawa, M.; Hamachi, I. *Nat. Chem.* **2009**, *1*, 557–561.
46. Huang, X.; Huang, G.; Zhang, S.; Sagiyama, K.; Togao, O.; Ma, X.; Wang, Y.; Li, Y.; Soesbe, T. C.; Sumer, B. D.; Takahashi, M.; Sherry, A. D.; Gao, J. *Angew. Chem. Int. Ed.* **2013**, *52*, 8074–8078.
47. Yamaguchi, K.; Ueki, R.; Nonaka, H.; Sugihara, F.; Matsuda, T.; Sando, S. *J. Am. Chem. Soc.* **2011**, *133*, 14208–14211.
48. Yu, J.; Kodibagkar, V. D.; Liu, L.; Mason, R. P. *NMR Biomed.* **2008**, *21*, 704–712.

Chapter 1 Development of off/on switching ^{19}F MRI probe based on PRE effect

(*Chem. Sci.*, **2011**, *2*, 1151–1155, *ChemBioChem*, **2012**, *13*, 1579–1583)

Introduction

The imaging of a gene expression can be used to obtain various information such as the expression timing of target proteins, gene transfer efficiency, detection of a disease-related gene expression, and so on.[1–5] To investigate gene expression, reporter proteins such as fluorescent proteins,[6–9] luciferase,[10–12] transferrin receptor,[13] β-gal,[14,15] and β-lac,[16–20] etc. are useful. Generally, the expression of these reporter proteins can be confirmed by fluorescence, bioluminescence, MRI, or colorimetric detection.

Table 1. Examples of reporter gene monitoring systems with MRI.

Reporter protein	Modality	Reporter probe	Endo/Exo[a]	Basic principle	Ref.
Creatine kinase	^{31}P MRS	Adenosine triphosphate	Endo	Chemical shift change	Koretsky *et al.*, 1989[21]
Polyphosphate kinase	^{31}P MRS/MRI	None	Endo	Formation of PolyP	Ki *et al.*, 2007[22]
Aminocylase-1	^{13}C MRSI	[1-^{13}C]*N*-acetyl-L-methionine	Exo	Chemical shift change	Chen *et al.*, 2011[23]
β-Galactosidase	^{19}F MRSI	PFONPG	Exo	Chemical shift change	Yu *et al.*, 2008[24]
β-Galactosidase	^{1}H MRI	EgadMe	Exo	Coordinated water number change (T_1)	Louie *et al.*, 2000[15]
Transferrin receptor	^{1}H MRI	Tf-MION	Exo	Accumulation of SPIO (T_2)	Weissleder *et al.*, 2000[13]
Ferritin	^{1}H MRI	Iron	Endo/Exo	Higher iron loading (T_2)	Cohen *et al.*, 2005[25]
Lysine-rich protein	^{1}H MRI	None	Endo	CEST	Gilad *et al.*, 2007[26]

Although various gene expression imaging systems for MRI based on different principles have been reported (Table 1), each method has its own advantages and limitations. The first reporter protein monitored by MRI was creatine kinase, and it was detected by ^{31}P MRS. Since endogenous ^{31}P is detected by ^{31}P MRS/MRI, exogenous probes are not required. However, the low NMR sensitivity of ^{31}P, which is only 6.6% of ^{1}H, remains unresolved. ^{1}H MRI reporter systems such as β-gal, transferrin receptor, and ferritin have been the most frequently reported systems, and the in vivo studies have been performed.[9] However, when a particular enzyme activity was imaged by ^{1}H MRI, it is generally difficult to distinguish the probe signal from the intrinsic background signals. In contrast, ^{19}F has a great potential for monitoring gene expression because of the high NMR sensitivity close to that of ^{1}H and the negligible endogenous background signals in ^{19}F MRI. However, only a few ^{19}F MRI reporter systems have been published, and they were not applicable to living samples.

Herein, the author describes smart ^{19}F MRI probes for monitoring gene expression via reporter enzyme activities. The probe design strategy was based on the PRE effect, which is a phenomenon in which the relaxation times of NMR nuclei are dramatically shortened near paramagnetic molecules.[27–29] In particular, Gd^{3+} ion has a very strong T_2-shortening activity because of its large electron spin number. The author's group has developed ^{19}F MRI probes based on PRE effect of Gd^{3+} ion to detect caspase-3 activity.[30,31] When fluorine atoms and a Gd^{3+} ion are attached to an enzyme substrate, T_2 of fluorine is decreased by a strong PRE effect from Gd^{3+} ion, resulting in the attenuation of ^{19}F MRI signal. The magnitude of the PRE is proportional to r^{-6}. Therefore, the cleavage of the substrate by enzyme induces the extension of the T_2, and the enhancement of the ^{19}F MRI signal. The author attempted to develop ^{19}F MRI probes that visualize gene expression by utilizing this principle.

1-1 ^{19}F MRI probe to detect β-gal activity

First, the author chose β-gal as the target reporter protein for gene expression because it has several advantages which reporter proteins are concerned.[32] The advantages are as follows: (1) induction of β-gal synthesis occurs over a large dynamic range, (2) β-gal is tolerated and is functional in many organisms including mammals, (3) various substrates of β-gal are available or feasibly synthesized, (4) many assay methods that use β-D-galactopyranoside-coupled aglycones are available, and (5) there is almost no intrinsic β-gal activity in mammalian cells. For these reasons, β-gal is one of the most widely used reporter proteins for imaging of gene expression, even though it has a few disadvantages such as a large molecular weight, no activity after extracellular secretion, etc. In this chapter, the author reports the design and synthesis of a novel ^{19}F MRI probe that detects β-gal activity and the ^{19}F MRI detection of gene expression in HEK293T cells.

Probe design concept, synthesis, and physical properties

Several probes have been developed that can detect β-gal activity.[33,34] X-gal is one of the most widely used probes among them. Such β-D-galactopyranoside-coupled aromatic compounds are known to be the substrates of β-gal, and several fluorescent probes for β-gal have been developed. Taking this substrate recognition property of β-gal into consideration, the author designed a ^{19}F MRI probe Gd-DFP-gal for detecting β-gal activity by combining the PRE based probe design principle with the structures of conventional β-gal probes (Figure 1). The T_2 of the ^{19}F nucleus near Gd^{3+} is expected to be reduced by the PRE from Gd^{3+}. Thus, the T_2 of the trifluoromethyl (CF_3) group of Gd-DFP-gal was expected to be strongly reduced.

Another designed function of Gd-DFP-gal is the self-immolative property that can be induced by enzymatic cleavage. When Gd-DFP-gal is hydrolyzed by β-gal, the probe is expected to be automatically converted to the corresponding quinone methide by the successive elimination of the substituent at the benzyl position.[35–37] Therefore, the T_2 of the trifluoromethyl group extends after the β-galactoside bond is cleaved because of the cancellation of the intramolecular PRE. Thus, the T_2 extension leads to an increase in the MRI signal. On the basis of this principle, the author expected that initially quenched ^{19}F MRI signal of Gd-DFP-gal would be recovered by the enzyme reaction.

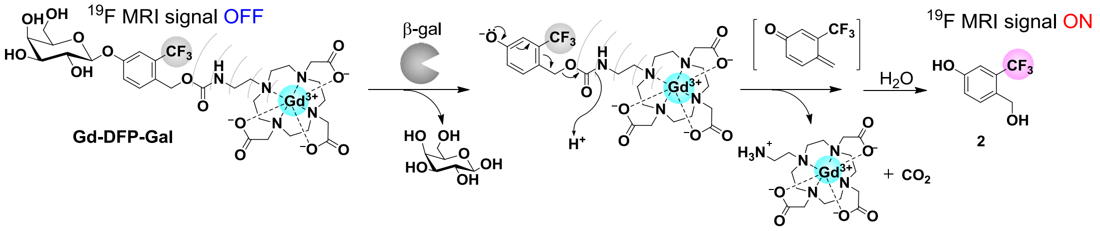

Figure 1. Principle of probe design. Structure of Gd-DFP-gal and the principle for ^{19}F MRI detection of β-gal activity.

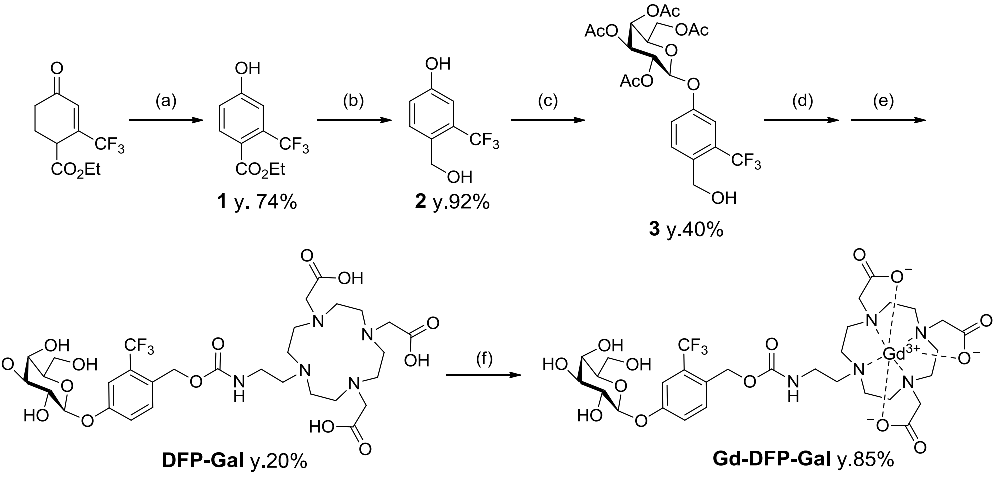

Scheme 1. Synthetic route to Gd-DFP-gal. (a) $CuBr_2$, NaBr, CH_3CN; (b) diisobutylaluminium hydride, THF; (c) 1-bromo-β-galactose tetraacetate, Cs_2CO_3, DMF; (d) 4-nitrophenyl chloroformate, pyridine, CH_2Cl_2; (e) 1) 1-(2-aminoethyl)-4,7,10-(triscarboxymethyl)-(1,4,7,10-tetraazacyclododecane), triethylamine, DMF, 2) NaOMe, MeOH; (f) $GdCl_3·6H_2O$, 100 mM HEPES buffer (pH 7.4).

Gd-DFP-gal was synthesized in five steps (Scheme 1). As the author expected, the NMR peak of Gd-DFP-gal was not observed, although that of the Gd-free probe DFP-gal was a sharp single peak (Figure 2). Disappearance of the ^{19}F NMR peak of Gd-DFP-gal indicates that the T_2 was markedly reduced because of the strong intramolecular PRE.

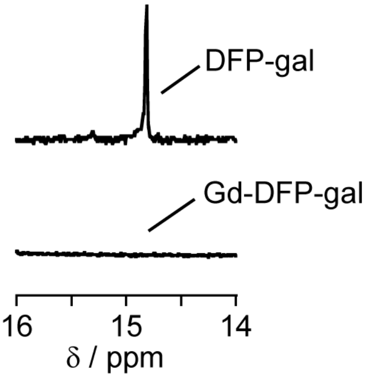

Figure 2. ^{19}F NMR spectra of DFP-gal (1mM) and Gd-DFP-gal (1 mM).

In vitro detection of β-gal activity by ^{19}F NMR and ^{19}F MRI

Because the relaxation times of Gd-DFP-gal were dramatically reduced, it was expected that the enzymatic degradation of Gd-DFP-gal would induce the recovery of the disappeared ^{19}F NMR peak. Gd-DFP-gal was incubated with β-gal at 37 °C in the reaction buffer, and the time course of the ^{19}F NMR peak was monitored (Figure 3a). A single peak appeared at around 16 ppm and increased in a time-dependent manner. To confirm the probe specificity, Gd-DFP-gal was incubated with other similar enzymes, α-gal and β-glu. After Gd-DFP-gal (1 mM) was incubated with α-gal or β-glu at 37 °C in the 100 mM phosphate buffer (pH 6.4) containing 5% D_2O for 2 h, the ^{19}F NMR

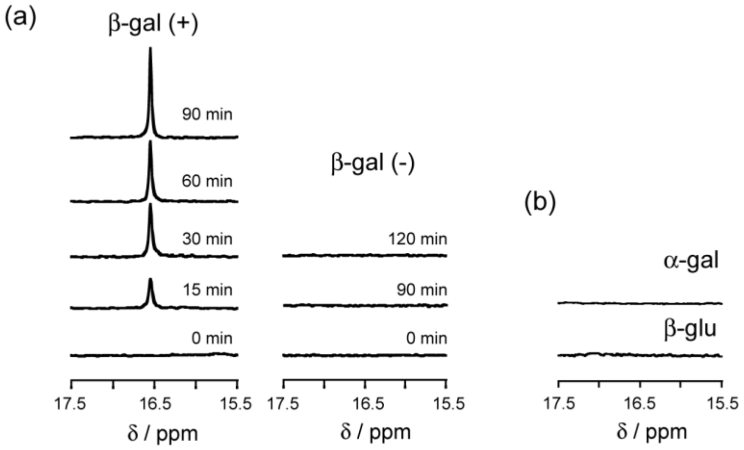

Figure 3. Detection of β-gal activity by Gd-DFP-gal. (a) Time-dependent ^{19}F NMR spectral change of Gd-DFP-Gal (1 mM) under incubation with β-gal (3 U). Sodium trifluoroacetate was used as the internal standard (0 ppm). (b) ^{19}F NMR spectra of Gd-DFP-Gal (1 mM) under incubation with α-galactosidase (top) or β-glucuronidase (bottom). Sodium trifluoroacetate was added as an internal standard (0 ppm).

spectra were obtained. However, ^{19}F NMR signal of Gd-DFP-gal were not recovered by incubation with such related enzymes (Figure 3b).

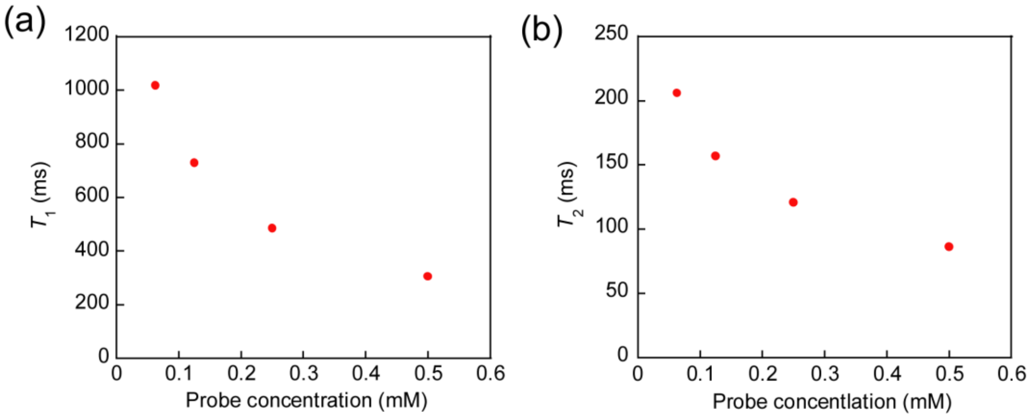

Figure 4. Plots of longitudinal and transverse relaxation times vs. concentration of Gd-DFP-gal after the complete cleavage by β-gal.

The relaxation times T_1 and T_2 of the reaction sample became 0.31 s and 0.086 s, respectively, after the enzyme reaction. Both of them showed considerable extension compared to those of Gd-DFP-gal, probably due to the cancellation of the intramolecular PRE from Gd^{3+}. These values are still less than those of the Gd^{3+}-free probe DFP-gal: 1.293 s for T_1 and 0.271 s for T_2. When the relaxation times of Gd-DFP-gal were measured at various probe concentrations after the enzymatic cleavage, both T_1 and T_2 extended as the concentration decreased (Figure 4). This concentration dependency of the relaxation times indicates that the intermolecular PRE is effective under the experimental condition even after the enzyme reaction is

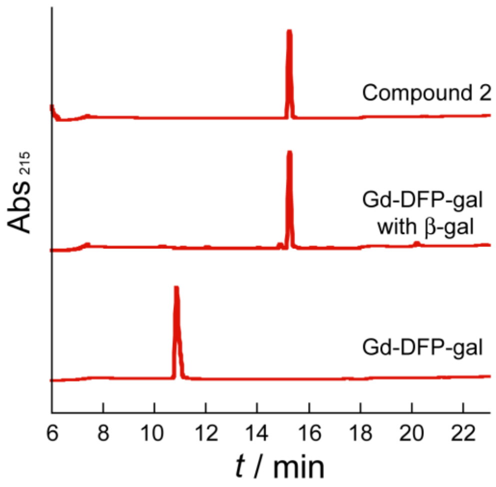

Figure 5. Confirmation of the enzymatic cleavage by RP-HPLC (eluent: H_2O/acetonitrile containing 0.1% TFA).

complete.

As the progress of the enzyme reaction was confirmed by RP-HPLC, the peak of Gd-DFP-gal disappeared and a new peak appeared (Figure 5). The new peak was identified to be 4-hydroxymethyl-3-trifluoromethylphenol (compound **2**) from the retention time. In addition, the ESI-MS of the HPLC peak fraction gave a molecular weight identical to **2** (m/z = 192). No other noticeable peaks in the reaction solution HPLC diagram suggest that Gd-DFP-gal was converted to **2** by β-gal activity with nearly complete efficiency.

To demonstrate the possibility of further application, ^{19}F MRI detection of β-gal activity was performed using Gd-DFP-gal. ^{19}F MRI phantom images were measured using an MRI instrument. Gd-DFP-gal was mixed with E. coli β-gal before being poured into a 1-mm-inner radius capillary. The density-weighted MR images were then captured by the fast spin-echo method. As expected from the ^{19}F NMR results, Gd-DFP-gal showed no ^{19}F MRI signals in the absence of β-gal. After the probe was mixed with β-gal, however, the ^{19}F MRI signals gradually increased in a time-dependent manner (Figure 6). These results demonstrate that this novel mechanism-based probe Gd-DFP-gal enables the specific ^{19}F MRI detection of β-gal activity.

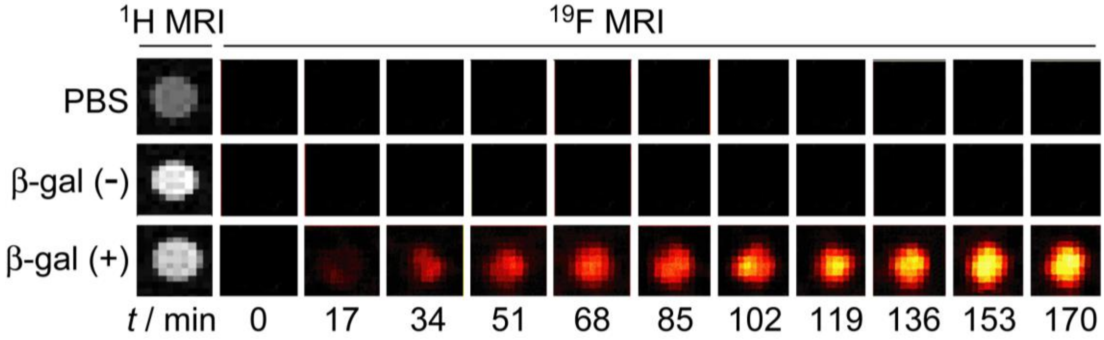

Figure 6. Time course of the ^{19}F MR phantom images of Gd-DFP-gal (1 mM) at 37°C after β-gal was added.

^{19}F NMR and MRI detection of cellular gene expression in HEK293T cell

Next, the application of Gd-DFP-gal to the detection of intracellular gene expression was performed. β-Gal was expressed in HEK293T cells, and the cells were fixed with formaldehyde and detergent. Then, Gd-DFP-gal was incubated with the cells, and β-gal activity in the medium supernatant was analyzed by ^{19}F NMR and MRI (Figure. 7a). As a result, incubation of Gd-DFP-gal only with the cells expressing β-gal induced the clear increase of a single ^{19}F NMR peak (Figure 7b).

Then, the ^{19}F MRI detection of β-gal gene expression was attempted. HEK293T cells expressing or not expressing β-gal were cultured on glass vessels. After the fixation of the cells, Gd-DFP-gal was added and incubated at 37°C for 2 h in the glass vessels. The vessels were stacked in an NMR tube, and the ^{1}H and ^{19}F MR images were captured. Although both vessels showed indistinguishable signal intensity in ^{1}H MRI (Figure 7c), only the vessel that included HEK293T cells expressing β-gal showed remarkable ^{19}F MRI signals. These results indicate that Gd-DFP-gal can specifically detect gene expression in fixed HEK293T cells by means of reporter β-gal activity.

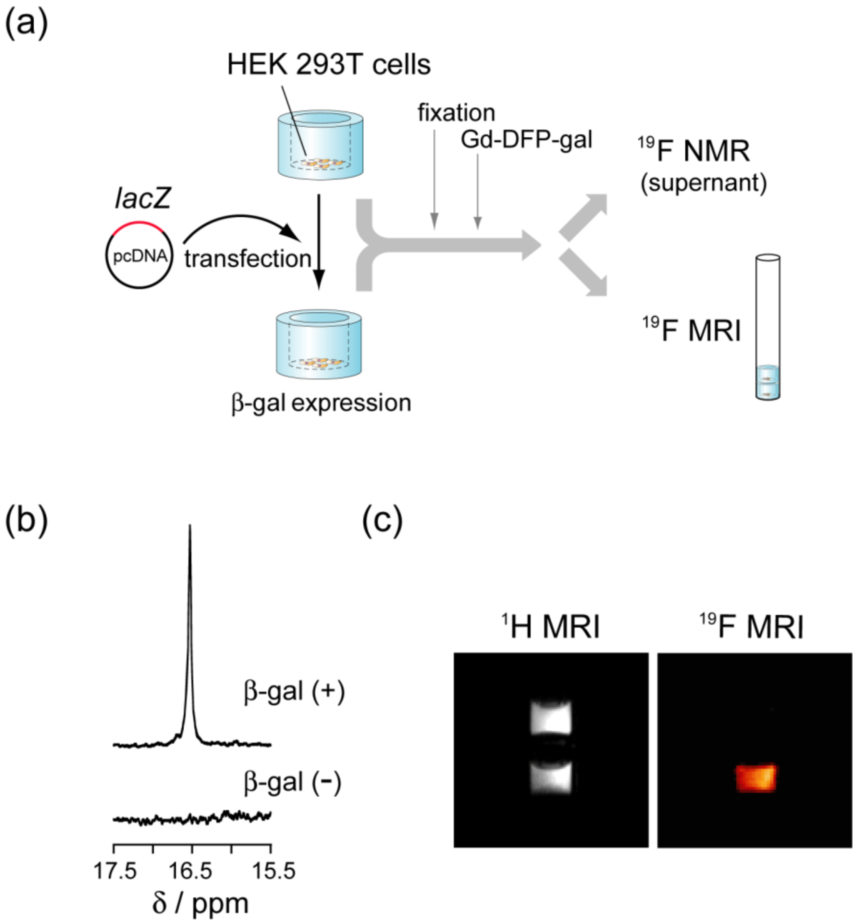

Figure 7. ^{19}F NMR and ^{19}F MRI detection of gene expression in HEK293T cells. (a) Illustration of the experimental procedures for the ^{19}F NMR and MRI measurements. (b) ^{19}F NMR spectra of the culture medium containing 1 mM Gd-DFP-gal incubated with fixed cells expressing (top) or not expressing (bottom) β-gal. (c) ^{1}H (left) and ^{19}F (right) MR images of culture vessels containing 1 mM Gd-DFP-gal fixed cells.

1-2 ^{19}F MRI probe to detect β-lac activity

The author detected β-gal activity for gene expression in cells with a specific ^{19}F MRI probe. However, the method required fixation of cells to image intracellular β-gal activity, because the probe did not permeate through intact plasma membrane. However, for further applications, probes must function in experiments involving living cells.

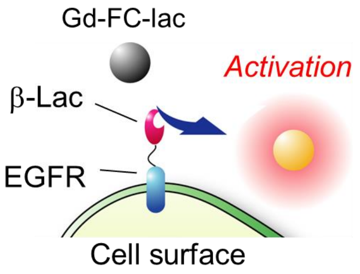

Figure 8. Surface-displayed β-lac reporter gene expression system with the specific ^{19}F MRI probe Gd-FC-lac.

Therefore, the author choses β-lac as the target reporter protein for gene expression. β-Lac, encoded by the *bla* gene, has various bioorthogonal advantages as a reporter protein, including the lack of an endogenous counterpart among eukaryotic cells and high substrate specificity.[17] Importantly, β-lac can be displayed on the bacterial membrane surface without losing activity.[38] Thus, the imaging system was constructed by exploiting β-lac displayed on the plasma membrane as a reporter enzyme and a specific ^{19}F MRI probe Gd-FC-lac rationally developed on the basis of the PRE effect (Figure 8).

Probe design, synthesis, and physical properties

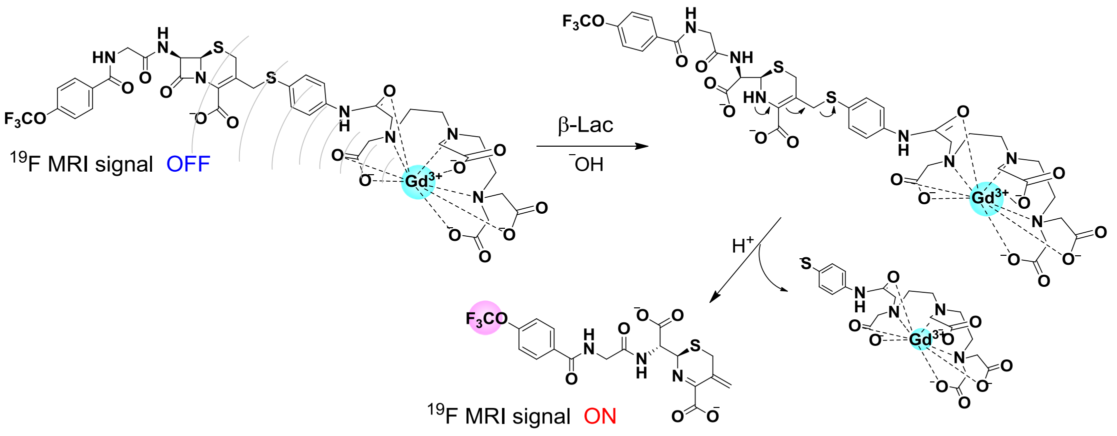

Figure 9. Structure of Gd-FC-lac and principles of ^{19}F MRI detection of β-lac activity.

The Gd-FC-lac probe was designed with three main components: the ^{19}F group, cephalosporin, and the Gd^{3+} complex (Figure 9). The T_2 of the probe was expected to be shortened by the intramolecular PRE effect from Gd^{3+} and the ^{19}F MRI signal would be attenuated. When the cephalosporin β-lactam ring of Gd-FC-lac is hydrolyzed by β-lac, the intermediate spontaneously decomposes, with self-elimination of the Gd^{3+} complex moiety. Thus, the T_2 of the fluorine is expected to increase due to cancellation of the intramolecular PRE. Since the T_2 values affect the apparent ^{19}F MRI signal intensity, the enzymatic degradation of Gd-FC-lac would lead to recovery of the ^{19}F MRI signal.

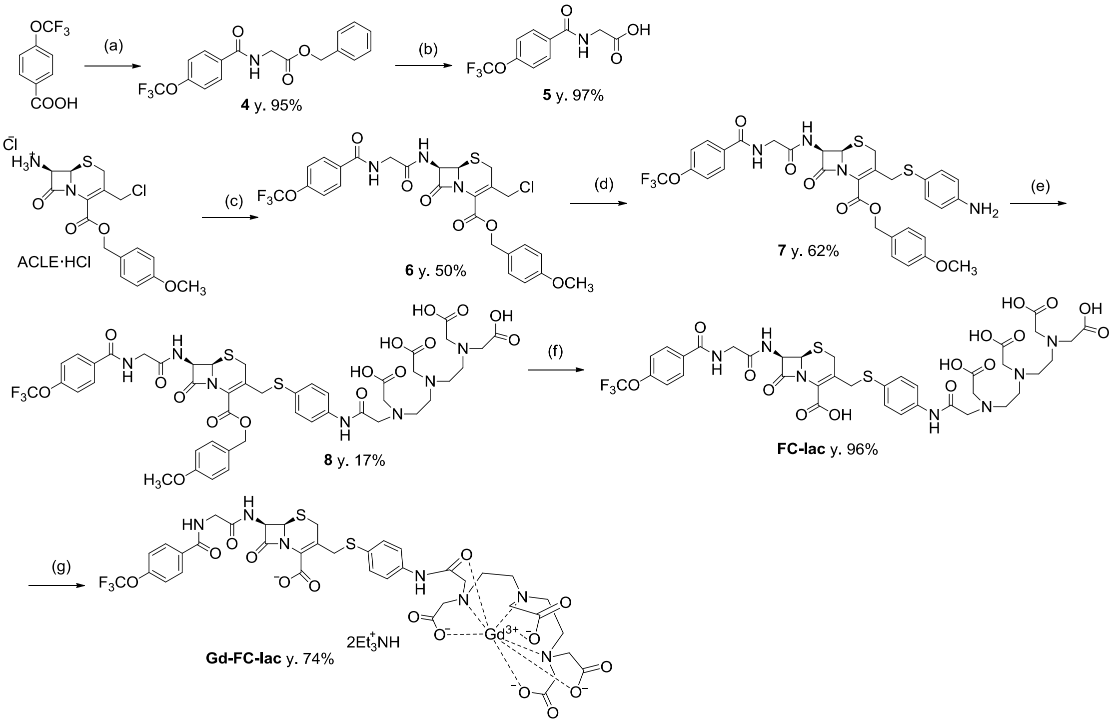

Scheme 2. Synthetic route to Gd-FC-lac. (a) Gly-OBn, WSCD·HCl, HOBt, TEA, DMF; (b) H_2, Pd-C, MeOH; (c) **5**, $POCl_3$, Pyridine, CH_2Cl_2; (d) 4-Aminothiophenol, NMM, DMF; (e) DTPA bisanhydride, TEA, DMF; (f) TFA, CH_2Cl_2, anisole; (g) $GdCl_3·6H_2O$, 100 mM HEPES buffer (pH 7.4).

Gd-FC-lac was synthesized from ACLE·HCl in five steps (Scheme 2). The final compound was purified by RP-HPLC, and the HPLC diagram of purified Gd-FC-lac showed a single peak. The structure was identified by ESI-MS.

In vitro detection of β-lac activity by ^{19}F NMR and ^{19}F MRI

Although the ^{19}F NMR spectrum of Gd^{3+}-free FC-lac showed a sharp single peak (T_1 = 1.63 s and T_2 = 0.368 s), the corresponding peak in the ^{19}F NMR spectrum of Gd-FC-lac was broader because of the intramolecular PRE effect (Figure 10a). The ^{19}F NMR relaxation times of Gd-FC-lac could not be precisely determined owning to the overwhelming PRE effect.^{19}F NMR analyses of the enzyme activity were performed by treating Gd-FC-lac with β-lac in the reaction buffer at 37°C. As expected, the ^{19}F NMR broad peak of Gd-FC-lac at around 18.5 ppm became sharper with the addition of the enzyme, and the peak height increased in a time-dependent manner (Figure 10b). This result indicates that the intramolecular PRE effect from Gd^{3+} was cancelled owing to the cleavage of cephalosporin followed by self-elimination of the Gd^{3+} complex. Next, the author monitored β-lac activity with ^{19}F MRI phantoms (Figure 10c). As expected from the NMR spectrum, ^{19}F MRI of Gd-FC-lac showed no signal because of the extremely short T_2. When the Gd-FC-lac solution sample with β-lac were scanned for a time-lapse measurement, the ^{19}F MRI intensity of the phantom increased gradually in a time-dependent manner, while the image of the control without β-lac did not change.

After the enzyme reaction, the relaxation times T_1 and T_2 of the reaction solution were 0.128 s and 0.033 s, respectively, at a probe concentration of 1 mM. Both relaxation times were considerably longer than those of Gd-FC-lac, and shorter than those of FC-lac. When Gd-FC-lac was completely cleaved by β-lac, both T_1 and T_2 were increased with decreasing concentration. The reciprocal plots of T_1 and T_2 showed linear correlations with the probe concentration. These data indicates that the intermolecular PRE remained effective despite the fact that the intramolecular PRE was cancelled after probe hydrolysis by the enzyme. Decrease in T_2 due to the intermolecular PRE after the enzyme reaction is an intrinsically undesirable phenomenon because it lowers the MRI signal intensity. However, the intermolecular PRE simultaneously decreased the T_1, and T_1 shortening to enable a shorter repetition time (T_R) in MRI measurements; therefore, the total acquisition time can be shorter for the same number of accumulations.[39] As a result, T_R for the ^{19}F MRI measurement of Gd-FC-lac was set at 0.25 s, which is much shorter than the TR suitable for the measurement of Gd-free FC-lac. The moderate intermolecular PRE effect was advantageous for reducing the total measurement time.

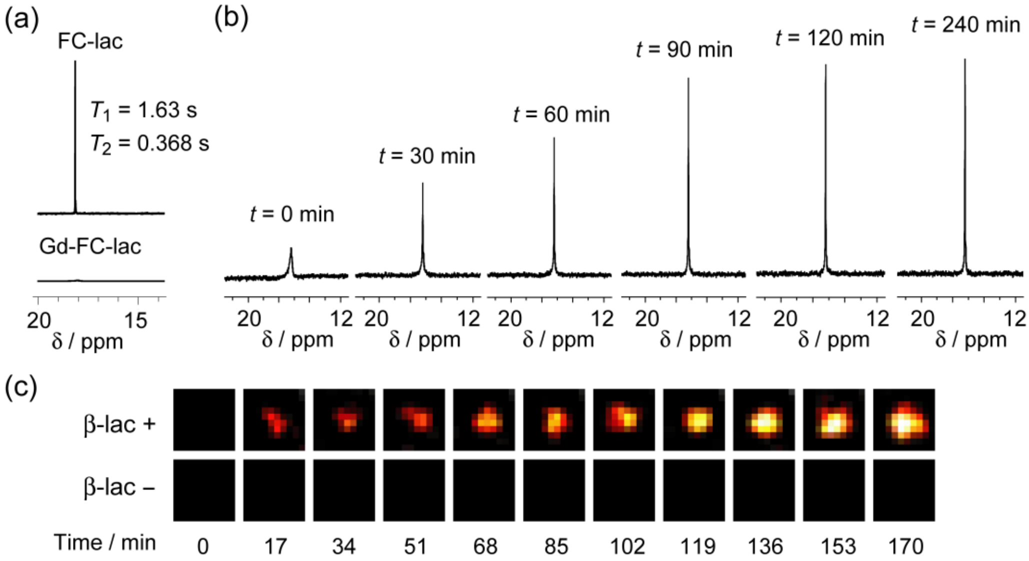

Figure 10. (a) ^{19}F NMR spectra of FC-lac (1mM) and Gd-FC-lac (1 mM). (b) Time-dependent ^{19}F NMR spectral change of Gd-FC-lac (1 mM) with β-lac (320 nM). (c) Time course of ^{19}F MR phantom images of Gd-FC-lac (1 mM) incubated with and without β-lac (320 nM).

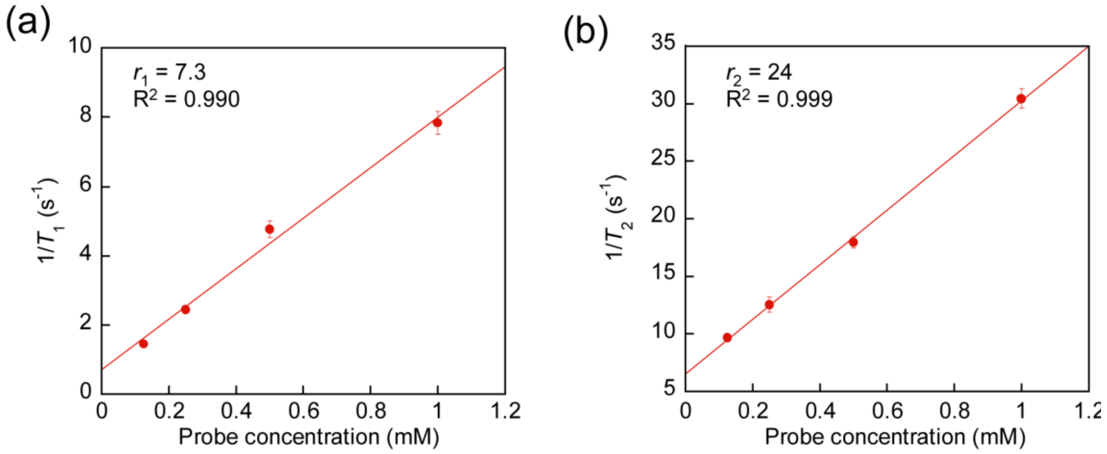

Figure 11. Concentration dependency of Gd-FC-lac with β-lac on (a) longitudinal and (b) transverse relaxation times.

^{19}F MRI detection of cellular gene expression via cell surface β-lac activity in live cell

The ^{19}F MRI detection of cellular gene expression without cell fixation was then investigated via cell surface-displayed β-lac activity. As described in the system design (Figure 8), β-lac was fused to the 170-kDa membrane-associated glycoprotein EGFR,[40] and the construct was expressed in HEK293T cells. The expression of β-lac-EGFR was confirmed by western blot analysis, and a single band corresponding to the fusion protein was detected from the transfected HEK293T cell lysate (Figure 12a).

For ^{19}F NMR, HEK293T cells expressing β-lac-EGFR were transferred to an NMR tube containing Gd-FC-lac, and the ^{19}F NMR spectra were monitored at 37°C (Figure 12b). The single ^{19}F NMR peak of Gd-FC-lac was recovered in a time-dependent manner, and the ^{19}F MRI signal increase was saturated in almost 6 h (Figure 12c). For ^{19}F MRI, the same sample tubes were attached with a surface coil, and the ^{1}H and ^{19}F MR images were captured. ^{19}F MRI signals were observed from the tube containing cells expressing β-lac-EGFR, whereas almost no signal was detected from the control, which contained EGFR-expressing cells (Figure 12d). These results indicate that gene expression in living cells was imaged by ^{19}F MRI. Results in this study are important for the development of innovative methodologies to visualize gene expression in living animals.

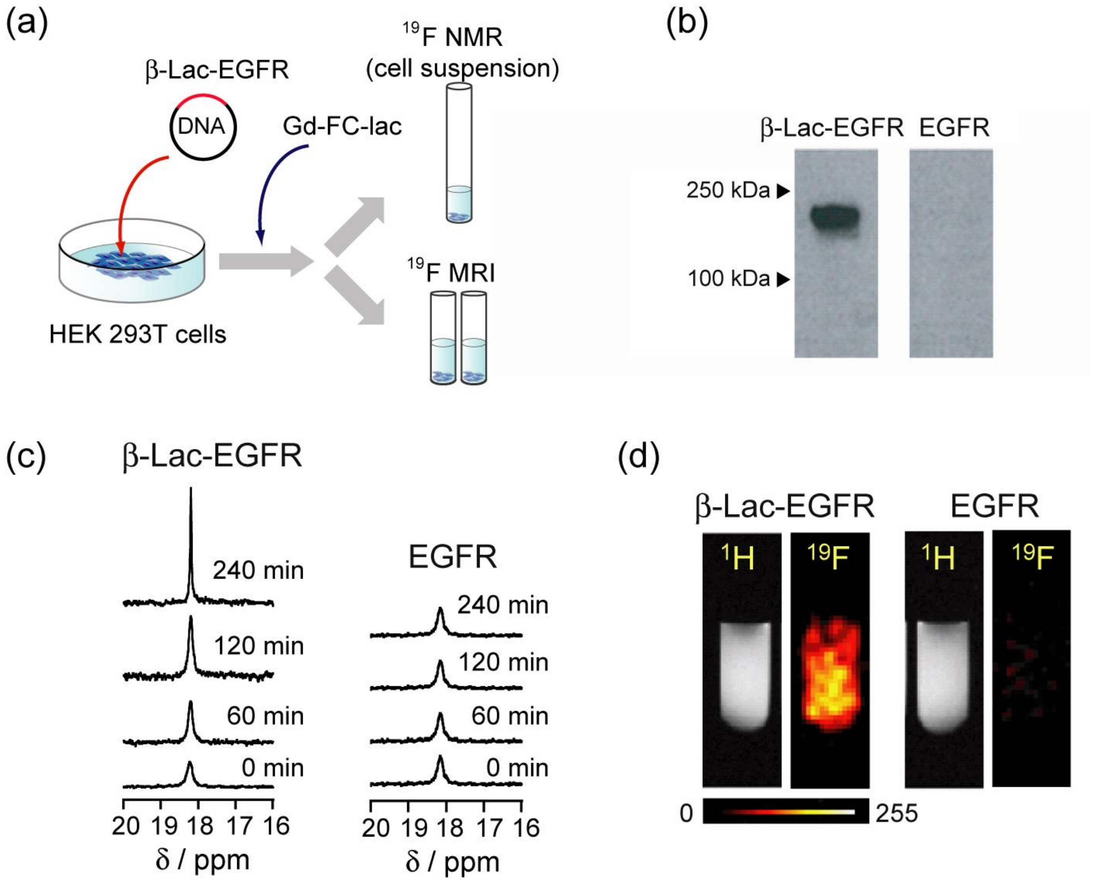

Figure 12. (a) Illustration of the experimental protocol to detect cell surface-displayed β-lac activity (b) Western blot of HEK 293T cell lysate expressing β-lac-EGFR or EGFR (c) Time course of ^{19}F NMR spectra of Gd-FC-lac (1 mM) incubated with HEK293T cells expressing β-lac-EGFR or EGFR (d) ^{1}H and ^{19}F MR images of Gd-FC-lac (1 mM) incubated with HEK293T cells expressing EGFR and β-lac-EGFR.

Experimental Sections for Gd-DFP-gal

Materials. General chemicals were of the best grade available, supplied by Tokyo Chemical Industries, Wako Pure Chemical, Aldrich Chemical Co., and Novabiochem. They were used without further purification. β-gal (G6008), β-glu (G7396), and α-gal (G8507) were purchased from Sigma Aldrich Life Science. The pcDNA^{TM}4/TO/*myc*-His/*lacZ* plasmid was purchased from Invitrogen (35-1614). Silica gel column chromatography was performed using BW-300 (Fuji Silysia Chemical Ltd.).

Instrument. NMR spectra were recorded using a JEOL JNM-AL400 instrument at 400 MHz for ^{1}H, at 100.4 MHz for ^{13}C NMR using tetramethylsilane as an internal standard, and for ^{19}F NMR at 376 Hz using sodium trifluoroacetate as an internal standard. ^{19}F NMR spectra were recorded using a JEOL JNM-AL400 instrument at 376 MHz using sodium trifluoroacetate as an internal standard. The T_1 and the T_2 were measured by inversion recovery method and spin-echo method, respectively. ESI-MS were measured using a Waters LCT-Premier XE. MRI images were recorded using a Bruker Avance DRX-500 spectrometer equipped with a standard bore (54 mm), an 11.7 T magnet, and a Micro-5-imaging probe head with an insert coil 8 mm in diameter. The RARE method was used for ^{1}H and ^{19}F MRI. For ^{19}F MRI, the matrix size was 32 × 32 (zero filled to 64 × 64) with a field of view of 16 × 16 mm, a slice depth of 15 mm, and a RARE factor of 32. The sweep width was 59523.8 Hz and the repetition time, and effective echo time were 250 and 28.4 ms, respectively. Gaussian-shaped pulses were used for excitation and refocusing. The number of accumulations was 3600. MRI image acquisition and processing were carried out using Para Vision software (Bruker BioSpin).

Synthesis of compounds

Ethyl 4-hydroxy-2-(trifluoromethyl)benzoate (1). To the acetonitrile solution of 4-carbethoxy-3-trifluoromethylcyclohex-2-enone (200 mg, 0.85 mmol, 1.0 eq.) were added $CuBr_2$ (380 mg, 1.7 mmol, 2.0 eq.) and NaBr (86.7 mg, 0.85 mmol, 1.0 eq.). The mixture was stirred at 60°C for 1 h. The solvent was removed under vacuum, and the crude product was diluted with ethyl acetate, and washed with 2 M hydrochloric acid and brine. The organic layer was dried over $MgSO_4$ and removed under vacuum to give the crude product. The product was dissolved in CH_2Cl_2, then purified with silica gel chromatography, eluted with CH_2Cl_2 to afford **1** (167 mg, 0.71 mmol, y. 84%). ^{1}H NMR (400 MHz, $CDCl_3$): δ 1.37 (t, J = 7.2 Hz, 3H), 4.36 (q, 2H, J = 7.2 Hz), 5.47 (s, 1H), 7.01 (dd, J = 2.4, 8.6 Hz, 1H), 7.20 (d, J = 2.4 Hz, 1H), 7.80 (d, J = 8.6 Hz, 1H); ^{13}C NMR (100 MHz, $CDCl_3$) δ13.8, 62.0, 115.4, 119.0, 123.3, 124.0, 132.1, 137.2, 159.0, 168.1; MS (ESI^{+}) *m/z*: 235 ($[M+H]^+$).

4-Hydroxymethyl-3-trifluoromethyl-phenol (2). A solution of **1** (124 mg, 0.53 mmol, 1.0 eq.) in dry THF was cooled to 0 °C. Diisobutylaluminium hydride (3.25 mL, 3.25 mmol, 6.0 eq. in toluene) was added and the solution was stirred at 0 °C for 30 min. Then, the solution was allowed to warm RT and stirred for 5 h. The mixture was added to 10% NH_4Cl aq. (1.0 mL) and extracted with diethyl ether. The organic layer was dried over $MgSO_4$ and removed under vacuum to give the pure product **2** (98 mg, 0.51 mmol, y. 97%). ^{1}H NMR (400 MHz, CD_3OD): δ 4.66 (s, 2H), 6.99 (dd, J = 2.8, 8.4 Hz, 1H), 7.04 (d, J = 2.8 Hz), 7.50 (d, J = 8.4 Hz, 1H); ^{13}C NMR (100 MHz, CD_3OD) δ

61.0, 113.5, 119.7, 127.1, 129.4, 131.3, 132.1, 158.0; HRMS (EI$^+$) *m/z*: 192.0395 (Calcd for $[M]^+$ 192.0398).

Tetraacetyl-β-galactopylanocyl-2-trifluoromethyl-benzylarcohol (3). 1-Bromo-β-galactose tetraacetate was prepared according to the literature.[41] Compound **2** (1.1 g, 5.7 mmol, 1.0 eq.) was dissolved in DMF, and cesium carbonate (7.41 g, 22.8 mmol, 4.0 eq.) was added to the solution at 0°C. 1-Bromo-β-galactose tetraacetate (10.6 g, 25.9 mmol, 4.5 eq.) in DMF was added dropwisely under Ar atmosphere, and the solution was stirred at RT for 3 h. Cooled 2 M hydrochloric acid was poured into the reaction mixture on ice bath. The product was extracted with ethyl acetate, and dried over $MgSO_4$, filtered, and evaporated. The crude product was purified by silica gel chromatography, eluted with ethyl acetate / hexane to afford **3** (1.7 g, 3.2 mmol, y. 57%). ^{1}H NMR (400 MHz, $CDCl_3$): δ 2.02 (s, 3H), 2.07 (s, 3H), 2.08 (s, 3H), 2.19 (s, 3H), 4.08–4.11 (m, 1H), 4.18–4.20 (m, 2H), 4.82–4.83 (m, 2H), 5.06–5.14 (m, 2H), 5.46–5.52 (m, 2H), 7.19 (dd, *J* = 2.4, 8.4 Hz, 1H), 7.30 (d, *J* = 2.4 Hz, 1H), 7.64 (d, *J* = 8.4 Hz, 1H); MS (ESI$^+$) *m/z*: 545 ($[M+Na]^+$).

DFP-gal. Compound **3** (513 mg, 0.98 mmol, 1.0 eq.) with one drop of anhydrous pyridine was dissolved in dry CH_2Cl_2 and placed under argon. Then, 4-nitrophenyl chloroformate (590 mg, 2.94 mmol, 3.0 eq.) were poured onto the mixture. After leaving for 3 h at RT, water was added and organic layer was carefully washed with 100 mM Na_2CO_3 solution, and with H_2O, then dried Na_2SO_4, filtered, and evaporated. The crude product was partly purified by silica gel chromatography, eluted with 2% $MeOH/CH_2Cl_2$ to afford activated carbonate. The activated carbonate (762 mg, 1.09 mmol, 1.0 eq.) and 1-(2-aminoethyl)-4,7,10-(triscarboxymethyl)-(1,4,7,10-tetraazacyclododecane) TFA salt[36] (850 mg, 2.18 mmol, 2.0 eq.) with anhydrous triethylamine (3.0 mL, 21.8 mmol, 20 eq.) were dissolved in dry DMF and placed under argon. The mixture was stirred at 50 °C for overnight. Then, the solvent was removed under vacuum to give the crude product. It was dissolved in MeOH, and sodium methoxide (2.9 g, 54.5 mmol, 50 eq.) in MeOH was slowly added on ice. Then, the solution was stirred on ice for 2 h. After neutralization by formic acid, the solvent was evaporated. The residue was dissolved in water containing 0.1% formic acid. RP-HPLC, eluted with H_2O/acetonitrile containing 100 mM ammonium formate to afford pure DFP-gal (y. 16%). ^{1}H NMR (400 MHz, CD_3OD): δ 2.87–3.90 (m, 36H), 5.19 (s, 2H), 7.36 (dd, *J* = 2.6, 8.0 Hz, 1H), 7.41 (d, *J* = 2.6 Hz, 1H), 7.57 (d, *J* = 8.0 Hz, 1H), 8.27 (s, 1H); ^{13}C NMR (100 MHz, CD_3OD): δ 9.58, 28.5, 60.8, 62.3, 70.1, 72.1, 74.7, 77.1, 103.0, 115.4, 115.5, 121.0, 131.4, 134.6, 158.0; ^{19}F NMR (376 MHz, CD_3OD with TFANa): δ 14.81 (s, 3F); HRMS (ESI$^+$) *m/z*:

770.2769 (Calcd for $[M+H]^+$ 770.3072).

Gd-DFP-gal. Crude DFP-gal was dissolved in 100 mM HEPES buffer (pH 7.4), and $GdCl_3 \cdot 6H_2O$ (1.2 eq.) was added. Then, the mixture was stirred at RT for 12 h. The product was purified with reversed-phase HPLC, eluted with H_2O/acetonitrile containing 100 mM ammonium formate to yield Gd-DFP-gal (y. 23%). HRMS (ESI^+) *m/z*: 925.1270 (Calcd for $[M+H]^+$ 925.2078).

^{19}F NMR relaxation time measurements. Samples were prepared at 500 µM concentration in 10 mM Tris buffer (pH 7.3) containing 10 mM magnesium chloride and 5% D_2O. The T_1 was measured by an inversion recovery method and the transverse relaxation time T_2 was measured by the spin-echo method.

Enzyme reaction. Gd-DFP-gal was dissolved at 500 µM in 10 mM Tris buffer (pH 7.3) containing 10 mM magnesium chloride and 5% D_2O. Samples (500 µL) were incubated with β-gal (5.03 U) at 37°C for 2 h. The reaction progress was monitored by ^{19}F NMR and RP-HPLC using an ODS column. For the ^{19}F MRI experiment, 1 mM Gd-DFP-gal was dissolved in 10 mM Tris buffer solution (pH 7.3) containing 10 mM magnesium chloride and 5% D_2O. Samples with or without β-gal (1.2 mU) were filled into glass capillaries (inner diameter: approximately 1 mm; Hischmann Laborgerate). The capillaries were then inserted into an 8 mm NMR tube and the ^{19}F MR images were captured.

Cellular experiments. HEK293T cells were grown at 37°C in DMEM supplemented with 10% FBS, 100 U/mL penicillin G, and 100 µg/mL streptomycin in a humidified atmosphere with 5% CO_2. The cells were plated at 1.2×10^6 cells in 60 mm dishes or 1.2×10^5 cells/cm^2 on 24-well plates. Next, the cells were transfected with pcDNA^{TM}4/TO/*myc*-His/*lacZ* plasmid using Lipofectamine 2000, and the cells were incubated for 24 h at 37°C in a CO_2 incubator. After the cells were washed three times with PBS, they were incubated with trypsin-EDTA at 37 °C for 5 min under 5% CO^2. For ^{19}F NMR analysis, the cells were cultured with 1 mM Gd-DFP-gal for 2 h at 37°C in the reaction buffer (10 mM Tris-sodium buffer (pH 7.3) and 10 mM magnesium chloride) on 24-well plates. Then, the supernatants were moved into NMR tubes and the ^{19}F NMR spectra were measured. For ^{19}F MRI, the cells were moved onto 7 mm (outer diameter) glass vessels (Hilgenberg GmbH), and were incubated for 7 h at 37°C in DMEM with 10% FBS. After the cells were washed three times with PBS, they were incubated with 3.7% formaldehyde for 10 min at room temperature. Then, cells were washed three times with PBS and incubated with 1 mM Gd-DFP-gal for 2 h at 37°C in the reaction buffer (Tris-sodium buffer (pH 7.3) and 10 mM magnesium chloride). The vessels were put into an 8 mm NMR tube, and the ^{1}H and ^{19}F MRI were measured.

Experimental Sections for Gd-FC-lac

Synthesis of compounds

Synthesis of 4. 4-(Trifluoromethoxy)benzoic acid (2.3 g, 11 mmol, 1.5 eq), Gly-OBn-Tos (2.5 g, 7.4 mmol, 1.0 eq), and HOBt (1.7 g, 11 mmol, 1.5 eq) were dissolved in dry DMF (100 mL), and then WSCD·HCl (2.1 g, 11 mmol, 1.5 eq) and dried TEA (2.1 mL, 15 mmol, 2.0 eq) were added at 0 °C. The mixture was stirred at 0°C for 30 min under Ar, and warmed to RT for 7 h. The solvent was diluted with ethyl acetate and washed with 4% $NaHCO_3$ aq., 10% citric acid, water and brine. The organic layer was dried over Na_2SO_4 and evaporated under reduced pressure to afford **1** (1.7 g, 4.8 mmol, y. 64 %). ^{1}H NMR ($CDCl_3$, 400 MHz) δ 4.22 (d, 2H), 5.17 (s, 2H), 6.53 (s, 1H), 7.19–7.31 (m, 7H); MS (ESI^{+}) *m/z*: 354.10 (Calcd for $[M+H]^{+}$: 354.09); ^{13}C NMR ($CDCl_3$, 100 MHz) δ 41.9, 67.4, 119.0, 120.6, 121.6, 128.4, 128.6, 128.7, 132.0, 135.0, 151.7, 166.1, 169.9.

Synthesis of 5. Compound **4** (1.7 g, 4.8 mmol) was dissolved in MeOH (340 mL), and 10% Pd/C (0.17 mg) was added. The reaction mixture was vigorously stirred under H2 at RT for 4 h. The reaction mixture was filtered and the filtrate was evaporated under reduced pressure to afford **5** (1.2 g, 4.9 mmol, y. 96%). ^{1}H NMR (DMSO-d_6, 400 MHz) δ 3.92 (d, 2H), 7.49 (d, 2H) 7.99 (d, 2H), 8.94 (t, 1H); MS (ESI^{+}) *m/z*: 264.03 (Calcd for $[M+H]^{+}$: 264.04); ^{13}C NMR (DMSO-d_6, 100 MHz) δ 41.3, 118.7, 120.7, 129.6, 132.9, 150.4, 165.2, 171.2.

Synthesis of 6. ACLE·HCl (4.0 g, 9.8 mmol, 2.0 eq) and **5** (1.2 g, 4.9 mmol, 1.0 eq) were dissolved in dry CH_2Cl_2 (150 mL) and dry pyridine (40 mL), and then distilled $POCl_3$ was added at -30°C. The mixture was stirred at -30°C for 2 h under Ar. The solvent was removed under reduced pressure, and the crude product was diluted with ethyl acetate and washed with 4% $NaHCO_3$ aq., 10% citric acid, and brine. The organic layer was dried over Na_2SO_4 and removed under vacuum to give the crude product **6**. The product was dissolved in 30% hexane/ethyl acetate, purified with silica gel chromatography, and eluted with 30% hexane/ethyl acetate to afford **6** (3.0 g, 4.9 mmol, 50%). ^{1}H NMR (DMSO-d_6, 400 MHz) δ 3.45–3.69 (m, 2H), 3.75 (s, 2H), 3.99 (t, 2H), 4.50 (dd, 2H), 5.10–5.21 (m, 2H), 5.25 (d, 1H), 5.74 (s, 1H), 6.92 (d, 2H), 7.34 (d, 2H), 7.47 (d, 2H), 7.98 (d, 2H), 8.86 (t, 1H), 8.99 (d, 1H); MS (FAB^{+}) *m/z*: 614.08 (Calcd for

$[M+H]^+$: 614.09); ^{13}C NMR (DMSO-d_6, 100 MHz) δ 26.1, 41.2, 42.2, 43.8, 55.1, 57.8, 59.0, 67.3, 113.8, 120.6, 121.2, 124.8, 125.3, 126.9, 129.7, 130.3, 133.0, 159.4, 161.1, 165.0, 165.3, 169.6.

Synthesis of 7. Compound **6** (1.8 g, 3.0 mmol, 1.0 eq) and 4-aminothiophenol (0.66 g, 4.5 mmol, 1.5 eq) were dissolved with dry DMF, and NMM (0.66 mL, 6.0 mmol, 2.0 eq) was added. Then, the mixture was stirred at RT for 2 h under Ar. The solvent was removed under vacuum, and the crude product was dissolved in CH_2Cl_2, purified with silica gel chromatography, and eluted with 3% MeOH/CH_2Cl_2 to afford **7** (1.3 g, 1.9 mmol, 63%). ^1H NMR ($CDCl_3$, 400 MHz) δ 3.75 (s, 3H), 3.99 (t, 2H), 4.60 (dd, 2H), 5.00–5.13 (m, 1H), 5.24 (d, 1H), 5.74 (s, 1H), 6.48 (d, 2H), 6.92 (d, 2H), 7.04 (d, 2H), 7.34 (d, 2H), 7.47 (d, 2H), 7.98 (d, 2H), 8.85 (t, 1H), 8.95 (d, 1H); MS (ESI^+) *m/z*: 703.16 (Calcd for $[M+H]^+$: 703.14); ^{13}C NMR ($CDCl_3$, 100 MHz) δ 28.6, 31.4, 43.3, 55.3, 57.7, 58.9, 67.5, 113.9, 115.4, 120.4, 151.5, 123.9, 127.0, 129.2, 133.4, 136.0, 147.0, 151.7, 159.8, 161.3, 162.6, 164.3, 166.6, 170.0.

Synthesis of FC-lac. DTPA bisanhydride (0.40 g, 0.90 mmol, 2.0 eq) and TEA (0.090 mL) were dissolved with dry DMF (38 mL), and a solution of compound **7** (0.33 g, 0.45 mmol, 1.0 eq) in DMF (12 mL) was slowly added. The solution was stirred at -30°C for 3 h, and the reaction was quenched by adding 2.5 mL of H_2O. The reaction mixture was evaporated to dryness. The residue was dissolved in water-acetonitrile containing 0.1% TFA (1:1 *v/v*, 3.0 mL). The residue was purified by RP-HPLC. A mixture of compound **8** and FC-lac (0.075 g) was obtained as a colorless solid. A mixture of compound **8** and FC-lac was dissolved in anhydrous CH_2Cl_2 (1.5 mL), and then thioanisole (0.30 mL) and TFA (1.5 mL) were added at 0°C. The mixture was stirred at 0°C for 2 h, and poured into cold ether (5.0 mL). The precipitate was collected and washed with ether to afford FC-lac (0.069 g, 0.072 mmol, y. 16%). ^1H NMR (CD_3OD, 400 MHz) δ 3.23–3.70 (m, 18H), 3.89 (t, 2H), 4.12 (dd, 2H), 4.35 (m, 3H), 4.99 (m, 2H), 5.67 (s, 1H), 6.91 (t, 1H), 7.25 (d, 2H), 7.27–7.39 (m, 4H), 7.98 (d, 2H); MS (ESI^+) *m/z*: 958.22 (Calcd for $[M+H]^+$: 958.21); ^{13}C NMR (CD_3OD, 100 MHz) δ 15.4, 29.2, 38.7, 43.6, 50.6, 51.2, 54.7, 55.0, 56.0, 56.3, 59.0, 59.4, 60.5, 67.0, 81.8, 114.8, 121.7, 130.1, 132.6, 134.0, 135.2, 139.4, 152.9, 163.6, 164.7, 166.0, 169.1, 169.6, 171.5, 172.1, 174.6, 174.8.

Synthesis of Gd-FC-lac. FC-lac (0.050 g, 0.051 mmol) was dissolved in 100 mM HEPES buffer (pH 7.4), and $GdCl_3 \cdot 6H_2O$ (0.039 g, 0.11 mmol) was added. Then, the mixture was stirred at RT for 12 h. The product was purified with RP-HPLC and eluted with H_2O/acetonitrile containing 100 mM triethylamine acetate solution to yield Gd-FC-lac (0.043 g, 0.040 mmol, y. 74%) and HRMS (ESI^-) *m/z*: 1111.1048 (Calcd for $[M-H]^-$: 1111.1060).

Nitrocefin assay of β-lac-EGFR expressed in HEK293T cells. Transfected HEK293T cells were prepared according to the aforementioned procedure. After 6 h, the culture medium was replaced with DMEM and the cells were incubated at 37°C for 24 h under 5% CO_2. After washing three times with PBS, HEK293T cells expressing each protein were cultured in a solution (phenol red free) containing nitrocefin (100 µM) at 37°C for 30 min. Then, the absorbance of the supernatant solution was measured at 488 nm.

In vitro enzyme assays. Gd-FC-lac was dissolved in 100 mM Tris-HCl (pH 7.4) containing 5% D_2O. The solution was incubated with β-lac (320 nM) at 37 °C for 4 h. Enzymatic reaction progress was monitored by ^{19}F NMR and ^{19}F MRI. For the ^{19}F NMR experiments, 1 mM Gd-FC-lac was dissolved in 100 mM Tris-HCl buffer solution (pH 7.4) containing 5% D_2O. Sodium trifluoroacetate was used as an internal standard. The NA was 16. For the ^{19}F MRI, Gd-FC-lac (1 mM) was dissolved in 100 mM Tris-HCl buffer solution (pH 7.4). Samples with or without β-lac (320 nM) were put into glass capillaries (inner diameter: approximately 1 mm; Hirschmann Laborgeräte). The capillaries were then inserted into an 8-mm NMR tube and the ^{19}F MRI images were obtained. The RARE method was used for ^{1}H and ^{19}F MRI. For ^{19}F MRI, the matrix size was 32 × 32 (zero filled to 64 × 64) with a FOV of 16 × 16 mm, a slice depth of 15 mm, and RARE factor of 32. The sweep width was 59,523.8 Hz, and the T_R and effective echo times ($T_{E,eff}$) were 250 ms and 28.4 ms, respectively. Gaussian shaped pulses were used for excitation and refocusing. The NA was 3600.

Western blot analysis of β-lac-EGFR expressed in HEK293T cells. HEK293T cells maintained in DMEM (Invitrogen) containing 10% FBS at 37°C under 5% CO_2 were transfected with a plasmid coding for β-lac-EGFR, which was prepared as reported previously,[42] by using Lipofectamine 2000. After 6 h, the culture medium was replaced with DMEM, and the cells were incubated at 37°C for 24 h under 5% CO_2. After washing three times with PBS, the cells were lysed with 200 µL of 1× SDS gel loading buffer (50 mM Tris-HCl buffer (pH 6.8), 1.3% SDS, 10% glycerol, and 5% mercaptoethanol). After scraping, the lysates were boiled at 95 °C for 3 min. Subsequently, samples underwent electrophoresis on a 10% SDS-polyacrylamide gel, and were transferred to a PVDF membrane for western blot analysis. Membranes were blocked by incubation for 1 h with TBST buffer (0.01% Tween 20, 138 mM NaCl, 20 mM Tris-HCl buffer (pH 7.6)) containing 5% skim milk. Then, anti-β-lac antibody was added to the membrane. After incubation for 16 h at 4°C with shaking, the membrane was washed three times with TBST buffer, incubated with horseradish peroxidase-linked secondary antibody, washed with TBST buffer, and visualized using ECL Western Blotting Detection Reagents.

^{19}F NMR and MRI analysis. Transfected HEK293T cells were prepared according to the western blot‘s experimental procedure. After 6 h, the culture medium was replaced with DMEM containing 10% FBS and kanamycin (100 μg mL^{-1}), and cells were incubated at 37°C for 24 h under 5% CO_2. After cells were washed with PBS three times, cells were harvested with trypsin-EDTA, washed with PBS, and mixed with DMEM (without phenol red). One portion of the mixture was used to confirm the cell surface β-lac activity by nitrocefin (100 μM), and the other fraction was transferred into NMR tubes containing Gd-FC-lac (1 mM), and the ^{19}F NMR spectra were measured at 37°C. A glass capillary containing sodium trifluoroacetate was set as an internal standard and NEX was 64. For ^{19}F MRI analysis, cells were transferred into an NMR tube containing DMEM with Gd-FC-lac (1 mM) and were incubated for 6 h at 37°C. The NMR tubes were fixed to a surface coil, and ^{1}H and ^{19}F MRI were performed. For the ^{1}H MRI, the matrix size was 256 × 256 with a FOV of 20 × 20 mm, a slice depth of 1 mm, and RARE factor of 16. The sweep width was 100,000 Hz, and T_R and $T_{E,eff}$ were 4000 ms and 35.4 ms, respectively. Gaussian-shaped pulses were used for excitation and refocusing. The NEX was 4. For the ^{19}F MRI, the matrix size was 32 × 32 (zero filled to 64 × 64) with FOV of 20 × 20 mm, a slice depth of 4 mm, and RARE factor of 8. The sweep width was 10,000 Hz, and T_R and $T_{E,eff}$ were 250 ms and 20.0 ms, respectively. Gaussian-shaped pulses were used for excitation and refocusing. The NEX was 4000.

References

1. Ray, P.; Bauer, E.; Iyer, M.; Barrio, J. R.; Satyamurthy, N.; Phelps, M. E.; Herschman, H. R.; Gambhir, S. S. Semin. *Nucl. Med.* **2001**, *31*, 312–320.
2. Gambhir, S. S.; Barrio, J. R.; Phelps, M. E.; Iyer, M.; Namavari, M.; Satyamurthy, N.; Wu, L.; Green, L. A.; Bauer, E.; MacLaren, D. C.; Nguyen, K.; Berk, A. J.; Cherry, S. R.; Herschman, H. R. *Proc. Natl. Acad. Sci. U. S. A.* **1999**, *96*, 2333–2338.
3. MacLaren, D. C.; Gambhir, S. S.; Satyamurthy, N.; Barrio, J. R.; Sharfstein, S.; Toyokuni, T.; Wu, L.; Berk, A. J.; Cherry, S. R.; Phelps, M. E.; Herschman, H. R. *Gene Therapy* **1999**, *6*, 785–791.
4. Kang, J. H.; Chung, J.-K. *J. Nucl. Med.* **2008**, *49*, 164–179.
5. Shah, K.; Jacobs, A.; Breakefield, X. O.; Weissleder, R. *Gene Therapy* **2004**, *11*,

1175–1187.

6. Tsien, R. Y. *Annu. Rev. Biochem*. **1998**, *67*, 509–544.
7. Shaner, N. C.; Campbell, R. E.; Steinbach, P. A.; Giepmans, B. N. G.; Palmer, A. E.; Tsien, R. Y. *Nat. Biotechnol*. **2004**, *22*, 1567–1572.
8. Elowitz, M. B.; Levine, A. J.; Siggia, E. D.; Swain, P. S. *Science* **2002**, *297*, 1183–1186.
9. Crameri, A.; A., Whitehorn. E. A.; Tate, E.; Stemmer, W. P. C. *Nat. Biotechnol*. **1996**, *14*, 315–319.
10. Degenfeld, G. Von; Wehrman, T. S.; Blau, H. M. *Methods Mol Biol.* **2009**, *574*, 249–259.
11. Yamazaki, S. *Science* **2000**, *288*, 682–685.
12. Bhaumik, S.; Gambhir, S. S. *Proc. Natl. Acad. Sci. USA* **2001**, *99*, 377–382.
13. Weissleder, R.; Moore, A.; Mahmood, U.; Bhorade, R.; Benveniste, H.; Chiocca, E. A.; Basilion, J. P. *Nat. Med.* **2000**, *6*, 351–355.
14. Nolan, G. P.; Fiering, S.; Nicolas, J. F.; Herzenberg, L. A. *Proc. Natl. Acad. Sci. U. S. A*. **1988**, *85*, 2603–2607.
15. Louie, A. Y.; Hüber, M. M.; Ahrens, E. T.; Rothbächer, U.;Moats, R.; Jacobs, R. E.; Fraser, S. E.; Meade. T. J. *Nat. Biotechnol.* **2000**, *18*, 321–325.
16. Zlokarnik, G.; Negulescu, P. A.; Knapp, T. E.; Mere, L.; Burres, N.; Feng, L.; Whitney, M.; Roemer, K.; Tsien, R. Y. *Science* **1998**, *279*, 84–88.
17. Campbell, R. E. *Trends Biotechnol*. **2004**, *22*, 208–211.
18. Gao, W.; Xing, B.; Tsien, R. Y.; Rao, J. *J. Am. Chem. Soc.* **2003**, *125*, 11146–11147.
19. Xu, C.; Xing, B.; Rao, J. *Biochem. Biophys. Res. Commun.* **2006**, *344*, 931–935.
20. Xing, B.; Khanamiryan, A.; Rao, J. *J. Am. Chem. Soc.* **2005**, *127*, 4158–4159.
21. Koretsky, A. P.; Traxler, B. A. *FEBS Lett*. **1989**, *243*, 8–12.
22. Ki, S.; Sugihara, F.; Kasahara, K.; Tochio, H.; Shirakawa, M.; Kokubo, T. *Biotechniques* **2007**, *42*, 209–215.
23. Chen, A. P.; Hurd, R. E.; Gu, Y.; Wilson, D. M.; Cunningham, C. H. *NMR Biomed.* **2011**, *24*, 514–520.
24. Cui, W.; Otten, P.; Li, Y.; Koeneman, K. S.; Yu, J.; Mason, R. P. *Magn. Reson. Med.* **2004**, *51*, 616–620.
25. Cohen, B.; Dafni, H.; Meir, G.; Harmelin, A.; Neeman, M. *Neoplasia* **2005**, *7*, 109–117.
26. Gilad, A. A.; McMahon, M. T.; Walczak, P.; Winnard, P. T.; Raman, V.; van Laarhoven, H. W. M.; Skoglund, C. M.; Bulte, J. W. M.; van Zijl, P. C. M. *Nat. Biotechnol*. **2007**, *25*, 217–219.

27. Belorizky, E.; Fries, P. H.; Helm, L.; Kowalewski, J.; Kruk, D.; Sharp, R. R.; Westlund, P.-O. *J. Chem. Phys.* **2008**, *128*, 052315.
28. Iwahara, J.; Schwieters, C. D.; Clore, G. M. *J. Am. Chem. Soc.* **2004**, *126*, 5879–5896.
29. Clore, G. M.; Tang, C.; Iwahara, J. *Curr. Opin. Struct. Biol.* **2007**, *17*, 603–616.
30. Mizukami, S.; Takikawa, R.; Sugihara, F.; Hori, Y.; Tochio, H.; Wälchli, M.; Shirakawa, M.; Kikuchi, K. *J. Am. Chem. Soc.* **2008**, *130*, 794–795.
31. Mizukami, S.; Takikawa, R.; Sugihara, F.; Shirakawa, M.; Kikuchi, K. *Angew. Chem. Int. Ed.* **2009**, *48*, 3641–3643.
32. Nielsen, D. A.; Chou, J.; Mackrell, A. J.; Casadaban, M. J.; Steiner, D. F. *Proc. Natl. Acad. Sci. USA* **1983**, *80*, 5198–5202.
33. Horwitz, J. P.; Chua, J.; Curby, R. J.; Tomson, A. J.; Rooge, M. A. D.; Fisher, B. E.; Mauricio, J.; Klundt, I. *J. Med. Chem.* **1964**, *7*, 574–575.
34. Pardee, A. B.; Jacob, F.; Monod, J. *J. Mol. Biol.* **1959**, *1*, 165–178.
35. Shabat, D.; Amir, R. J.; Gopin, A.; Pessah, N.; Shamis, M. *Chem. Eur. J.* **2004**, *10*, 2626–2634.
36. Duimstra, J. A.; Femia, F. J.; Meade, T. J. *J. Am. Chem. Soc.* **2005**, *127*, 12847–12855.
37. Komatsu, T.; Kikuchi, K.; Takakusa, H.; Hanaoka, K.; Ueno, T.; Kamiya, M.; Urano, Y.; Nagano, T. *J. Am. Chem. Soc.* **2006**, *128*, 15946–15947.
38. Francisco, J. A.; Earhartt, C. F.; Georgiou, G. *Proc. Natl. Acad. Sci. USA* **1992**, *89*, 2713–2717.
39. Chalmers, K. H.; Kenwright, A. M.; Parker, D.; Blamire, A. M. *Magn. Reson. Med.* **2011**, *66*, 931–936.
40. Herbst, R. S. *Int. J. Radiat. Oncol. Biol. Phys*. **2004**, *59*, 931–936.
41. Montero, J.; Winum, J.; Leydet, A.; Kamal, M.; Pavia, A. A.; Roque, J. *Carbohydr. Res.* **1997**, *297*, 175–180.
42. Mizukami, S.; Watanabe, S.; Hori, Y.; Kikuchi, K. *J. Am. Chem. Soc.* **2009**, *131*, 5016–5017.

Chapter 2 Multifunctional core-shell silica nanoparticles, FLAME, for highly sensitive ^{19}F MRI

(*Angew. Chem. Int. Ed.* **2014**, *53*, 1008–1011)

2-1 Limitations of small-molecule based ^{19}F MRI probes

In the previous chapter, the author described ^{19}F MR imaging of gene expression in live cells. However, several problems remain unresolved for in vivo imaging, such as the potential diffusion of the activated probes. In other words, the ^{19}F MRI signals of the activated probes diffuse over time after catalytic activation of ^{19}F MRI probes, as MRI measurements are often repeated over hours or days. In these cases, the observed MRI signals do not reflect the position of gene expression. Therefore, the author focused on mutant β-lac (BL-tag) to overcome the diffusion of activated ^{19}F MRI probes. Previous studies have shown that Glu166 of β-lac (TEM-1, class A) has critical role for the deacylation step as the base for hydrolysis of the acyl-intermediate.[1–3] Thus, the E166N mutant of β-lac is stopped at the acyl-enzyme intermediate through marked slowing of deacylation relative to acylation (Scheme 1).[4–6] The author aimed to exploit the properties of BL-tag to covalently attach a fluorine-containing substrate to the gene expression product.

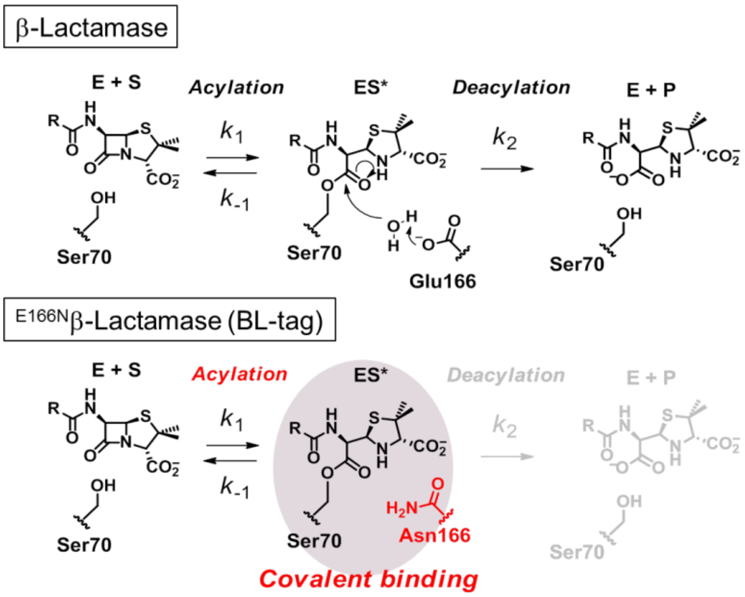

Scheme 1. Mechanism of β-lactam cleavage by ^{WT}β-lac (class A) and ^{E166N}β-lac. (BL-tag).

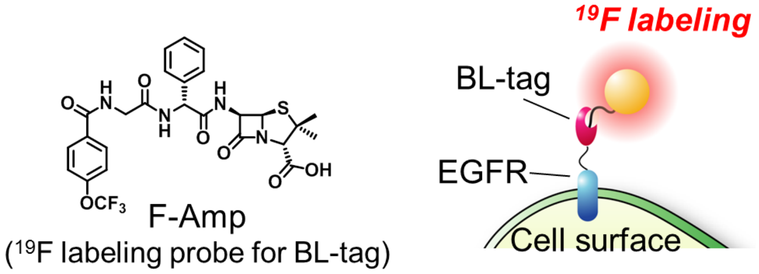

Figure 1. (a) ^{19}F labeling of BL-tag on the cell surface with F-Amp.

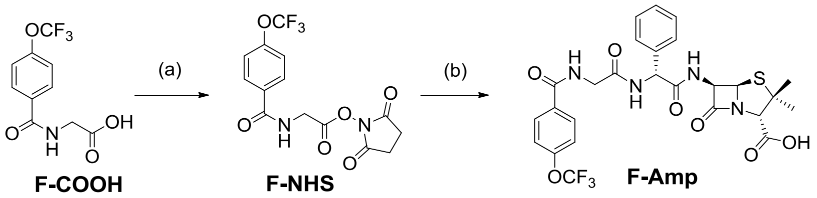

Scheme 2. Synthetic route to F-Amp (a) *N*-hydroxysuccinimide, WSCD·HCl, TEA, DMF; (b) ampicillin, TEA, DMF

The author designed and synthesized a penicillin-based fluorine probe (F-Amp) to investigate the feasibility of ^{19}F-labeling of the cell surface using a BL-tag (Figure 1a). The synthetic scheme for F-Amp is presented in Scheme 2. Substrate consumption was confirmed by RP-HPLC. The HPLC peak of F-Amp did not change for 240 min. In contrast, the peak of F-Amp treated with β-lac disappeared and a new peak appeared (Figure 2). The new peak was identified as the hydrolysate of F-Amp by ESI-MS. These results indicate that F-Amp was reacted with β-lac with nearly complete efficiency.

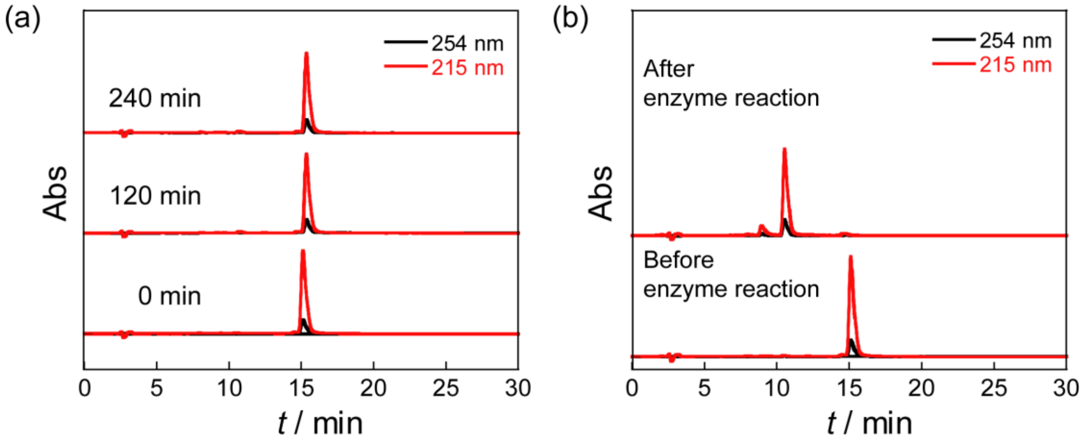

Figure 2. RP-HPLC diagram of F-Amp (100 μM). (a) Stability of F-Amp at 37°C. (b) HPLC analysis of F-Amp incubated with or without a wild-type β-lactamase (500 nM) at 37°C for 30 min. Elute: 40% acetonitrile/60% water containing 0.1% TFA (0 min) → 0.1% TFA (aq.) 70% acetonitrile/30% water containing 0.1% TFA (30 min).

In this experiment, the BL-tag was fused to the EGFR; the recombinant protein was expressed on the surface of HEK293T cells,[4,7–9] and BL-EGFR expressing cells were treated with F-Amp. After the cells were rinsed with PBS, ^{19}F NMR was measured. However, no ^{19}F NMR signal was detected from the cell suspension (Figure 3a), probably because of the following two reasons. First, the probe's fluorine moiety was attached covalently to the protein and could not be catalytically amplified. Second, the free molecular mobility of the fluorine can be hindered by the protein attachment. To address these limitations, it is important to increase the number of fluorine atoms that possess an equivalent chemical shift.[10–12] However, simple multiplication of the fluorine atoms does not provide higher sensitivity because increasing the number of fluorine atoms also decreases the solubility of the molecular probes.[13] Second, T_2 relaxation of fluorine is accelerated through restriction of the molecular mobility resulting from attachment to the reporter protein on the cell surface (Figure 3b). The suppression of molecular mobility induced by the increase in molecular size shortens the T_2, resulting in attenuation of the MRI signal.[14–17] Therefore, improvements of small-molecule based ^{19}F MRI probes are required for their further practical applications.

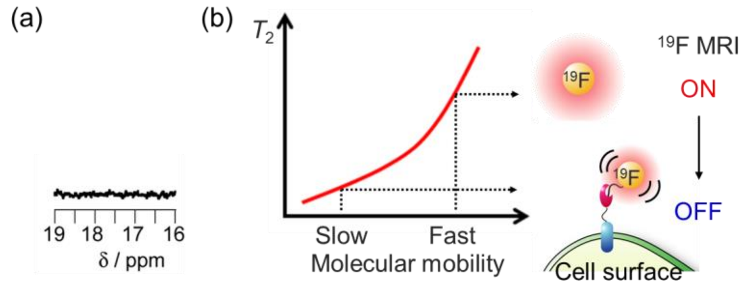

Figure 3. (a) ^{19}F NMR spectra of suspended BL-EGFR expressing HEK293T cells suspension treated with F-Amp (9.6 mM) at 37 °C for 2 h. (b) Molecular mobility and T_2.

2-2 Design and preparation of highly sensitive ^{19}F MRI contrast agent

To solve these two problems simultaneously, the author designed a novel ^{19}F MRI probe consisting of a core-shell nanoparticle based on a PFCE. PFCE has various attractive characteristics as a ^{19}F MRI contrast agent.[11,12,18–20] First, it has 20 equivalent fluorine atoms, which show a sharp single ^{19}F NMR peak to yield a strong signal. Second, many liquid PFCEs are expected to maintain their high molecular mobility in a nanoparticle. Based on these advantages, PFCE nanoemulsions have been reported for in vivo cell tracking. However, the instability of PFCE nanoemulsions in organic solvents significantly limits their applications that rely on surface modification. Even under neutral buffer conditions, Ostwald ripening, which is a molecular diffusion

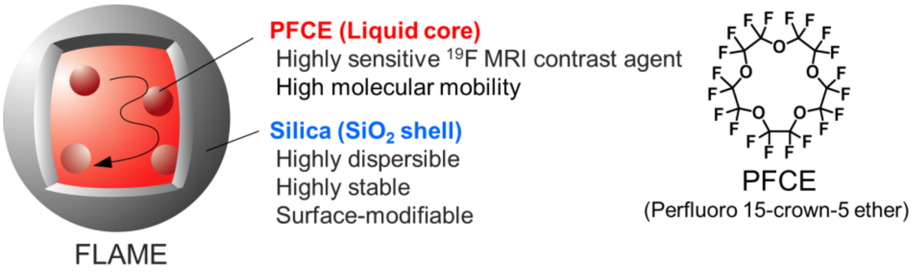

Figure 4. The components of FLAME.

phenomenon resulting in the gradual growth of larger particles, can be a major problem for the stability.[21–23] To overcome this limitation, the author covered the PFCE nanoemulsion with a silica shell (Figure 4). Silica nanoparticles possess attractive features such as biological inertness and favorable colloidal properties.[24–29] In addition, the silica surface can be variously modified with functional groups to realize targeted delivery and specific functions.[30–32] Herein, the author reports a multifunctional ^{19}F MRI contrast agent, FLAME, and demonstrates its superior properties for ^{19}F MRI such as high sensitivity, stability, surface modifiability, and biocompatibility together with biomedical applications such as reporter assays and in vivo tumor imaging.

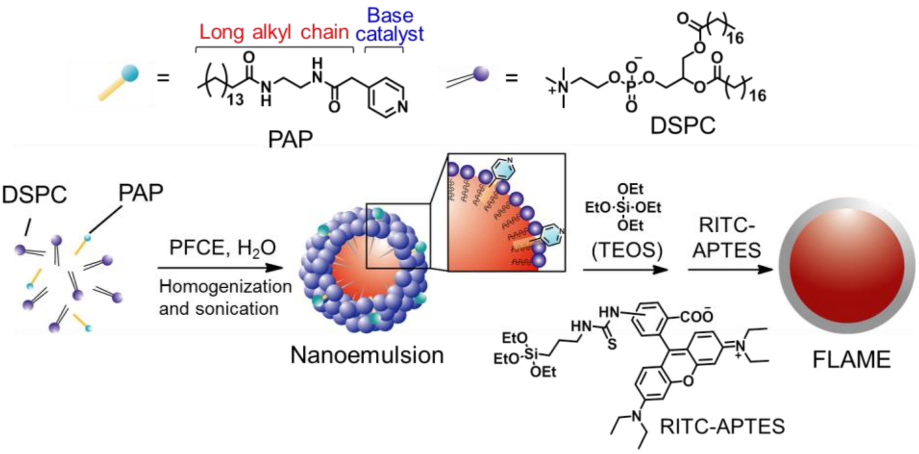

Scheme 2. Preparation of FLAME.

The synthetic protocol of FLAME is presented in Scheme 2. To cover the PFCE-phospholipid nanoemulsion with silica gel, the author developed a novel surfactant, PAP (Scheme 3), which consists of an alkyl part to interact with phospholipids[33] and a basic pyridinyl group. When template nanoemulsions are formed in the presence of PAP, the basic site of PAP was expected to be displayed on the nanoemulsion surface and to initiate the sol-gel process of tetraethyl orthosilicate.[34] As a result, the silica polymerization reaction occurred only near the nanoemulsion surface,

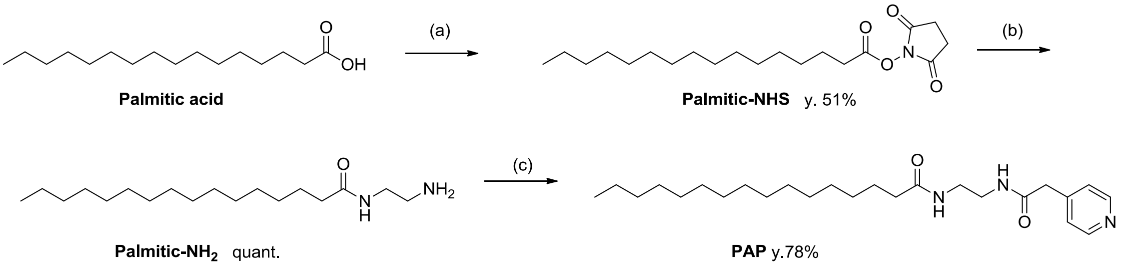

Scheme 3. Synthetic route to PAP. (a) *N*-hydroxysuccinimide, WSCD·HCl, DMF; (b) 1, 2-Ethylenediamine, CH_2Cl_2; (c) 4-Pyridylacetic acid hydrochloride, WSCD·HCl, HOBt, TEA

and silica coating of the PFCE nanoemulsion was achieved. RITC was covalently attached to the silica shell, which allowed for the fluorescence detection.

DLS measurements also indicated the silica coating of nanoemulsion. The hydrodynamic diameter was changed from 80 nm of the nanoemulsion to 131 nm of FLAME, and the ζ-potential decreased from +29.5 mV of the nanoemulsion to –4.5 mV of FLAME (Figure 5a, b). The core-shell structures of FLAME were clearly observed by TEM (Figure 5c). The average diameter of the particles was 76 ± 9 nm, which was calculated from the TEM images (*n* = 200). On the other hand, the silica shell was not well formed in the absence of PAP.

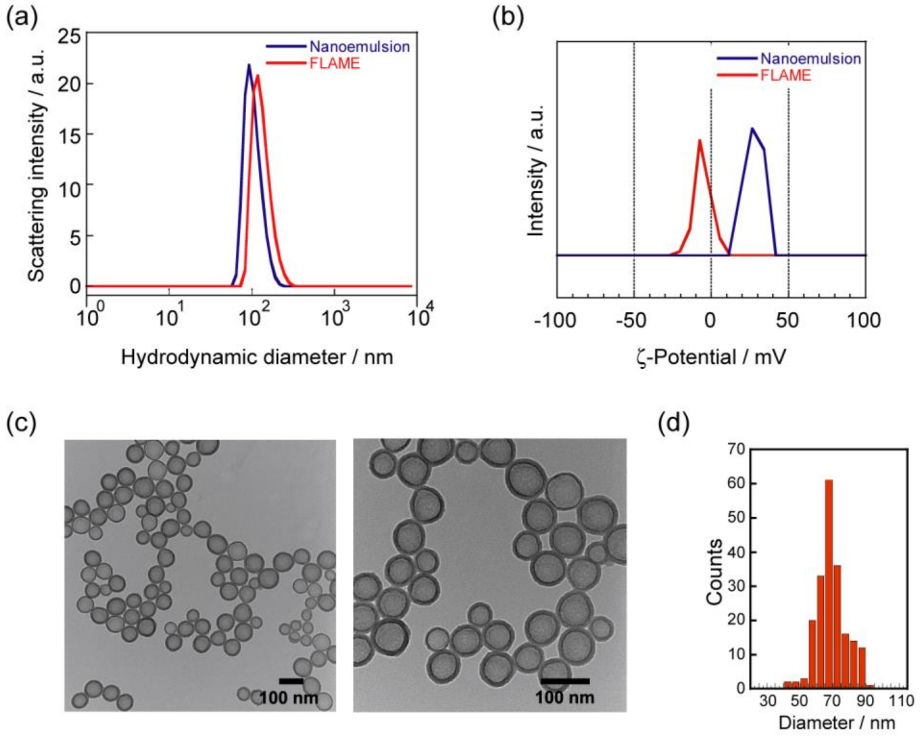

Figure 5. (a) Hydrodynamic diameter of the nanoemulsion (red) and FLAME (blue) by DLS. (b) ζ-Potential graphs of the nanoemulsion (blue) and FLAME (red). (c) TEM image of FLAME. (c) Particle size distribution histogram calculated from TEM images

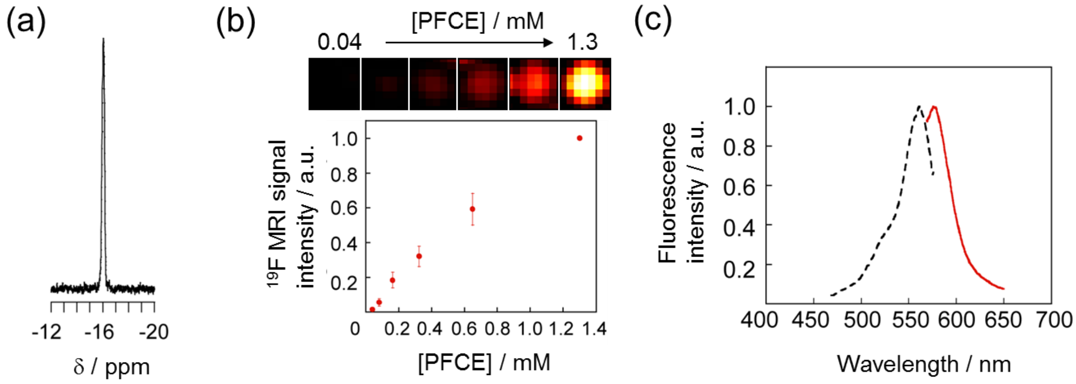

Figure 6. (a) ^{19}F NMR spectrum of FLAME. (b) MR images properties of FLAME. (b) Excitation and emission spectra of FLAME.

Inclusion of PFCE in the particle was confirmed by NMR spectroscopy. The ^{19}F NMR of FLAME dispersed in PBS solution showed a PFCE-derived single peak at –16.4 ppm (Figure 6a). In the ^{19}F MRI measurements, strong ^{19}F MRI signals were observed from FLAME (Figure 6b). The ^{19}F MRI signal intensity was proportional to the PFCE concentration. FLAME showed the typical fluorescence emission of RITC (Figure 6c).

2-3 Monitoring of gene expression via BL-tag

To demonstrate the high ^{19}F MRI sensitivity, FLAME was applied to a ^{19}F MRI-based reporter assay with BL-tag. Thus, ampicillin-modified FLAME (FLAME-Amp) was prepared for the specific ^{19}F MRI detection of the reporter protein (Figure 7). The synthetic scheme of FLAME-Amp was presented in Scheme 4.

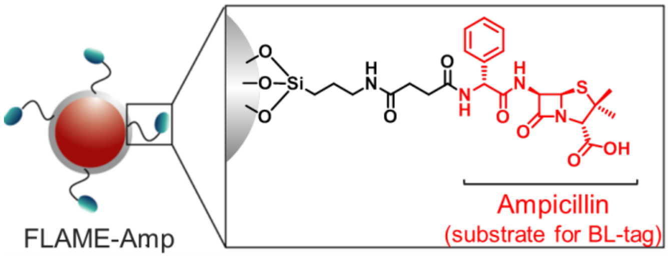

Figure 7. The chemical structure of FLAME-Amp.

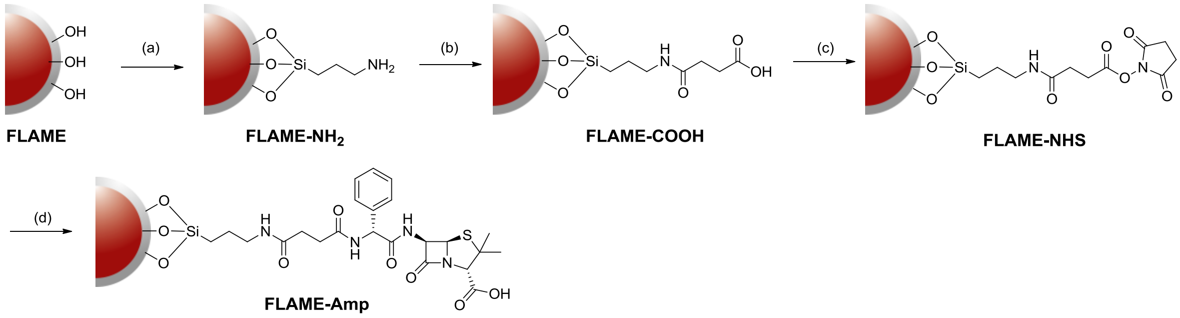

Scheme 4. Synthetic route to FLAME-Amp. (a) 3-aminopropyltetraethoxysilane, 2-propanol; (b) Succinic anhydride, DMF, TEA; (c) *N*-hydroxysuccinimide, TEA, DMF; (d) ampicillin, TEA, DMF.

Table 1. ζ-Potential values and hydrodynamic diameters of the nanoemulsion and FLAMEs.

Materials	Hydrodynamic diameter (nm)	ζ-Potential (mV)
FLAME	131 ± 1	-4.5 ± 0.2
FLAME-NH_2	161 ± 32	12.5 ± 0.9
FLAME-COOH	90 ± 2	-62.0 ± 1.2
FLAME-Amp	96 ± 2	-55.8 ± 2.0

To confirm the specific binding of FLAME-Amp to the BL-tag protein, the author used a fusion protein of BL-tag and MBP, which non-covalently bind to an amylose with high affinity (Figure 8a).[35,36] After FLAME-Amp was incubated with an

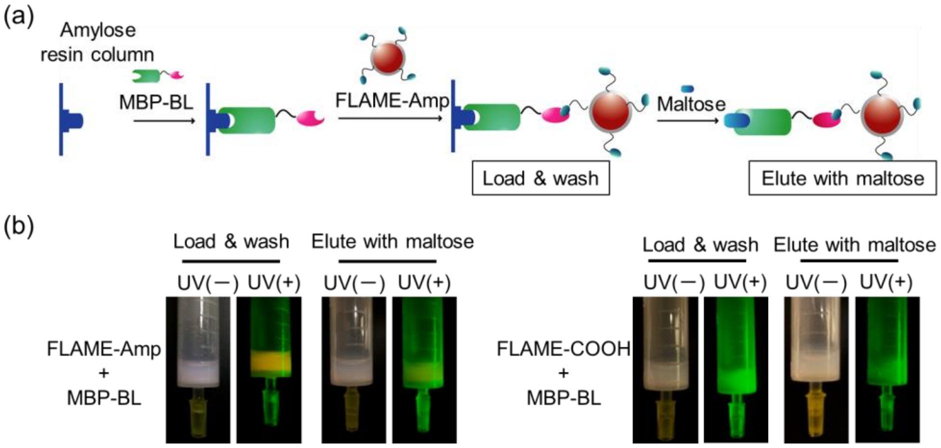

Figure 8. (a) Schematic procedure for purification of FLAME-Amp conjugated with MBP-BL. (b) Photographs of amylose resin (a) after washing with wash buffer or (b) elution buffer containing 10 mM maltose under irradiation with white light (left) and UV light (right). The fluorescence of the amylose resin shows that FLAME-Amp bound to MBP-BL. Fluorescence visualization also showed that FLAME-COOH did not bind to MBP-BL. These results indicate that the ampicillin part of FLAME-Amp is essential for the specific binding to MBP-BL.

MBP-BL-bound amylose resin, the non-bound components were removed by washing with a buffer solution. The fluorescence of the amylose resin showed that FLAME-Amp bound to MBP-BL, and MBP-BL conjugated with FLAME-Amp was eluted by a maltose-containing solution (Figure 8b).

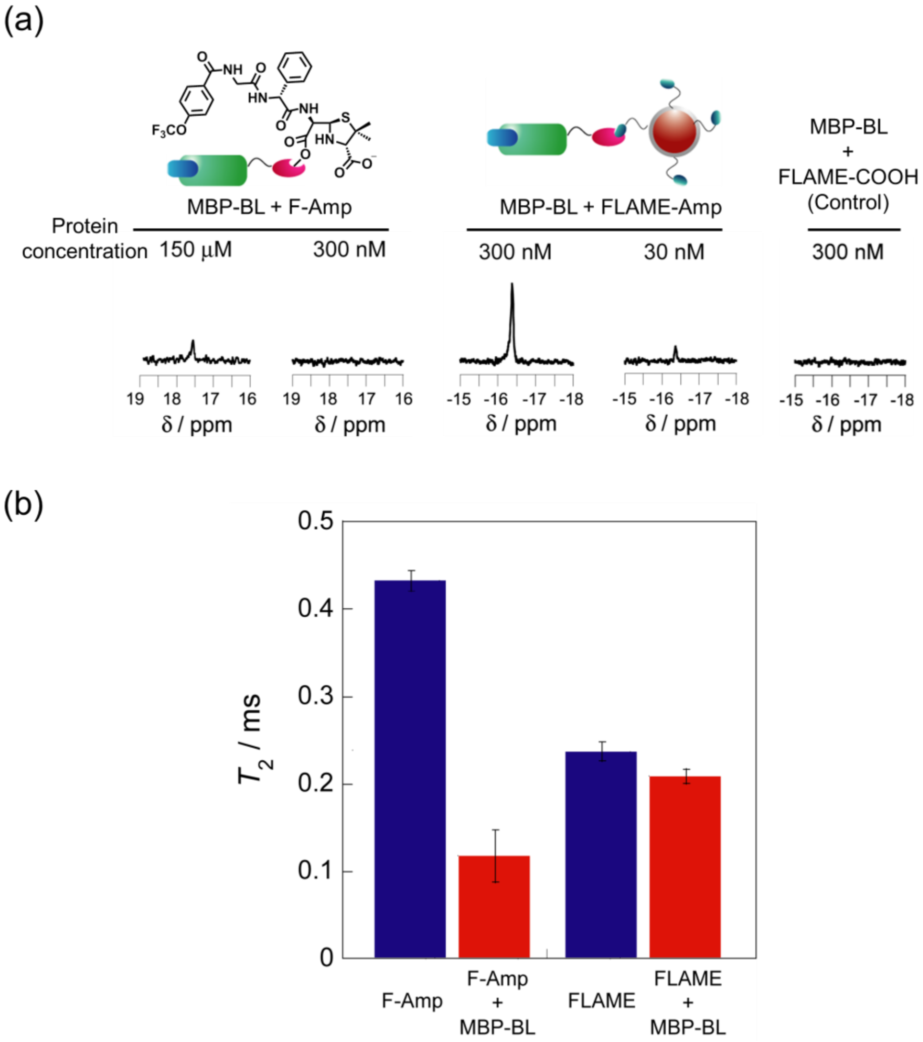

Figure 9. (a) Highly sensitive ^{19}F NMR detection of MBP-BL proteins with FLAME-Amp. The accumulation time was 21 min 50 s. (b) T_2 of FLAME-Amp and F-Amp conjugated with MBP-BL.

Then, the fractions eluted with a maltose solution were analyzed by ^{19}F NMR. A sufficiently high and sharp ^{19}F NMR peak was detected from MBP-BL incubated with FLAME-Amp (Figure 9a). The ratio of fluorine atoms to protein was 4.7×10^3. The ^{19}F NMR peak was detected even at a MBP concentration of 30 nM. In contrast, the ^{19}F NMR signal of F-Amp was not observed at a MBP-BL concentration of 300 nM. At least concentrations of the target protein in the µM range were required for NMR detection by the small-molecule probe due to the low ^{19}F density per probe. In contrast, FLAME-Amp encapsulating a large amount of fluorine atoms enabled the detection of the target proteins in the nM range. Another important factor for the sensitivity improvement is the molecular mobility of fluorine atoms. The mobility of small-molecule probes is largely decreased by the binding to proteins; furthermore, it causes the T_2 reduction, which decreases the NMR signal. The T_2 of F-Amp drastically shortened from 0.434 s to 0.119 s by the covalent binding to MBP-BL and the ^{19}F NMR signal was decreased (Figure 9b). On the other hand, the T_2 of FLAME-Amp conjugated to MBP-BL was 0.210 s, which is comparable to that of FLAME-Amp (0.238 s). These results demonstrate that the molecular mobility of PFCE was maintained even after FLAME was attached to a protein.

Next, ^{19}F MRI detection of gene expression was attempted via a cell surface-displayed reporter protein (Figure 10a). After FLAME-Amp was incubated with cells expressing BL-EGFR, NMR and MRI experiments were performed (Figure 10b). The strong ^{19}F NMR and MRI signals were clearly observed from BL-EGFR-expressing cells incubated with FLAME-Amp, whereas almost no signal was detected from the control EGFR-expressing cells. As a result, specific and highly sensitive ^{19}F MRI detection of gene expression in living cells was successfully demonstrated by FLAME-Amp.

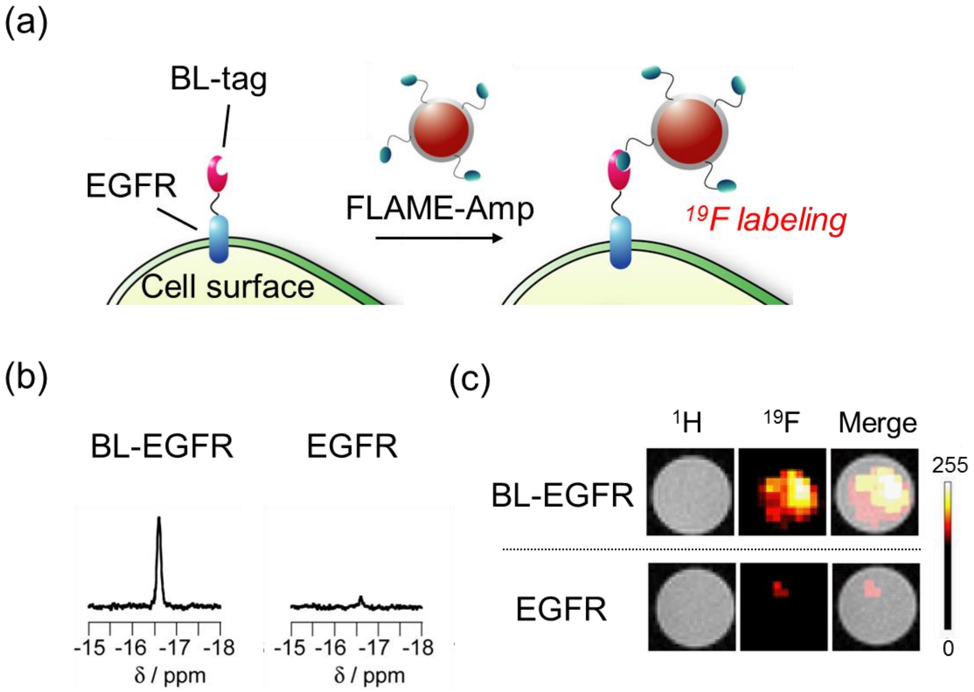

Figure 10. (a) ^{19}F MRI detection of gene expression using BL-EGFR and FLAME-Amp. (b) ^{19}F NMR spectra and MRI of BL-EGFR-expressing HEK293T cells treated with FLAME-Amp and EGFR-expressing HEK293T cells. Cells: 6.0 × 10^5, C_{PFCE} = 2.6 mM, incubation time: 5 min, temperature: 4°C, accumulation times were 10 min 55 s for ^{19}F NMR, 8 min 32 s for ^{19}F MRI, respectively.

2-4 In vivo ^{19}F MRI with FLAME for tumor imaging

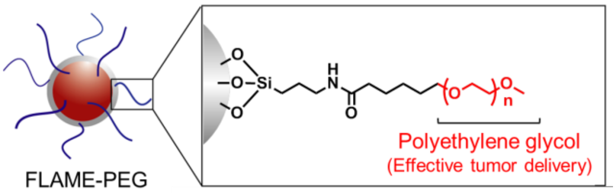

Figure 11. The chemical structure of FLAME-Amp.

Finally, the potential of FLAMEs for in vivo targeting were evaluated in tumor-bearing mice. The nanomaterials were delivered to the tumor via the EPR effect, which promotes nanoparticle accumulation in cancerous tissues by a combination of leaky angiogenic blood vessels and deficient tumor lymphatics.[37–41] However, the naked nanoparticles should be trapped immediately by the RES and show decreased circulation time.[42–45] Therefore, FLAME was modified with PEG for the effective delivery to tumors (FLAME-PEG, Figure 11). PEGylation reduces the uptake by increasing the electrostatic interactions with proteins and small molecules.[46–54]

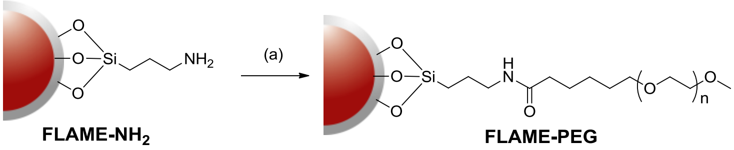

Scheme 5. Synthetic route to FLAME-PEG. (a) methoxy-PEG-$(CH_2)_5$-COO-NHS (MW 5000), TEA, DMF

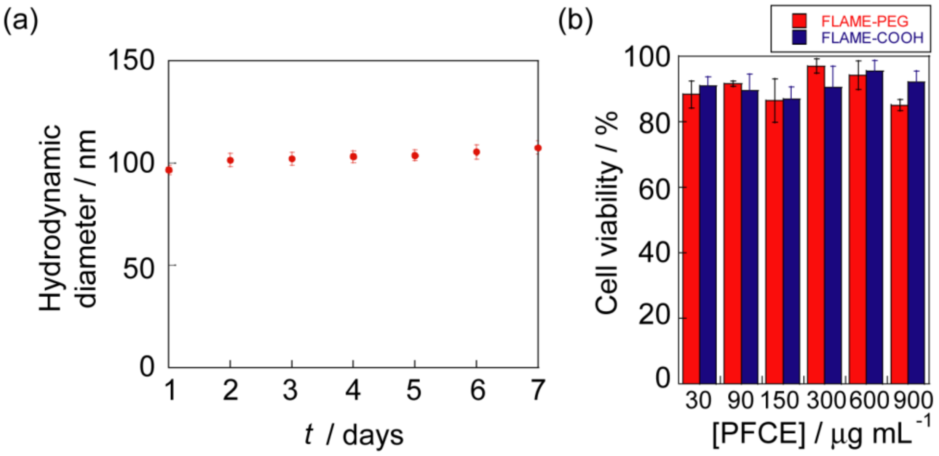

Figure 12. (a) DLS analysis of FLAME-PEG followed over time at 4°C storage temperature. (b) Cytotoxicity of FLAME-PEG and FLAME-COOH against cultured colon-26 cells.

FLAME-PEG was synthesized from FLAME-NH_2 (Scheme 5). DLS analysis to determine the stability of FLAME-PEG showed that there was almost no change in the particle size for 1 week (Figure 11a). The biocompatibility of FLAME-PEG was evaluated in the MTT assay. The viability of colon-26 cells was not affected by 24-h exposure of FLAME-PEG and up to 900 μg mL^{-1} of PFCE (Figure 12b).

Passive targeting and accumulation of FLAME-PEG via the EPR effect were demonstrated by MRI (Figure 13). Mice bearing a tumor were given intravenous injections of FLAMEs. Strong ^{19}F MRI signals of FLAME-PEG at the tumor site indicated passive targeting of the nanoparticles. The ^{19}F NMR measurements of homogenized tissue samples showed that NMR signals were detected only from liver (C_{PFCE} = 113 nmol g^{-1}) and tumor (C_{PFCE} = 28.8 nmol g^{-1}), but not from spleen, lungs, brain, kidneys, and heart (Figure 14a). However, the ^{19}F MRI signals of non-PEGylated FLAME (FLAME-COOH) was detected only in the liver, indicating that FLAME-COOH was immediately trapped by the RES. These results indicate that the intensity of the ^{19}F MRI signal of FLAME is sufficient for in vivo studies and that the distribution of FLAME in living animals can be controlled by changing its chemical properties through surface modification of FLAME. The accumulation of FLAME-PEG in tumor and liver sections was verified by the RITC fluorescence (Figure 14b). Meanwhile, in the case of FLAME-COOH, fluorescence signals were detected only in the livers and spleens, not at the tumors. These results demonstrate that the ^{19}F MRI

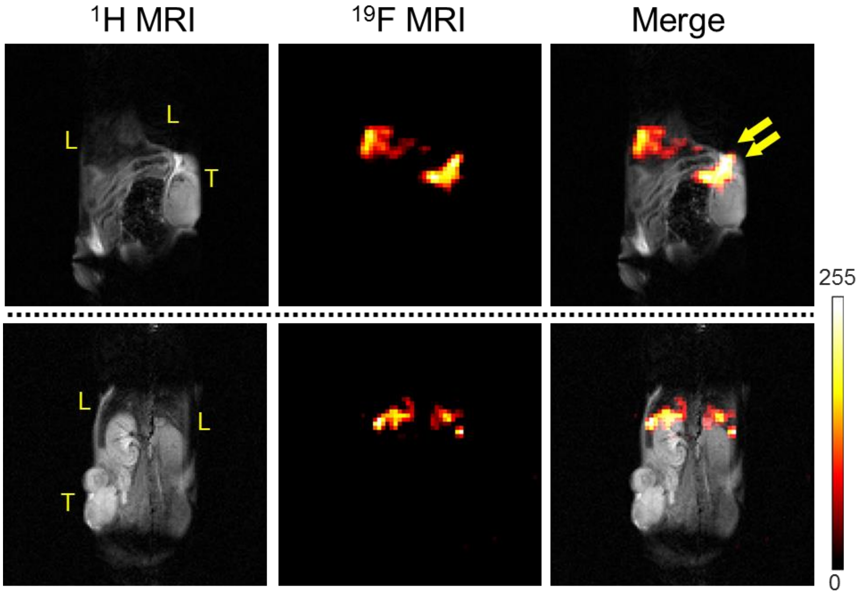

Figure 13. In vivo MRI of FLAME-PEG and FLAME-COOH in tumor-bearing mice at 3 hours after intravenous injection. The positions of the liver and tumor are represented as L and T, respectively. Injection volume: 200 μL, C_{PFCE} = 2.6 mM, acquisition time: 8 min 32 s.

signal localization reflect the actual accumulation position of FLAMEs in animal bodies.

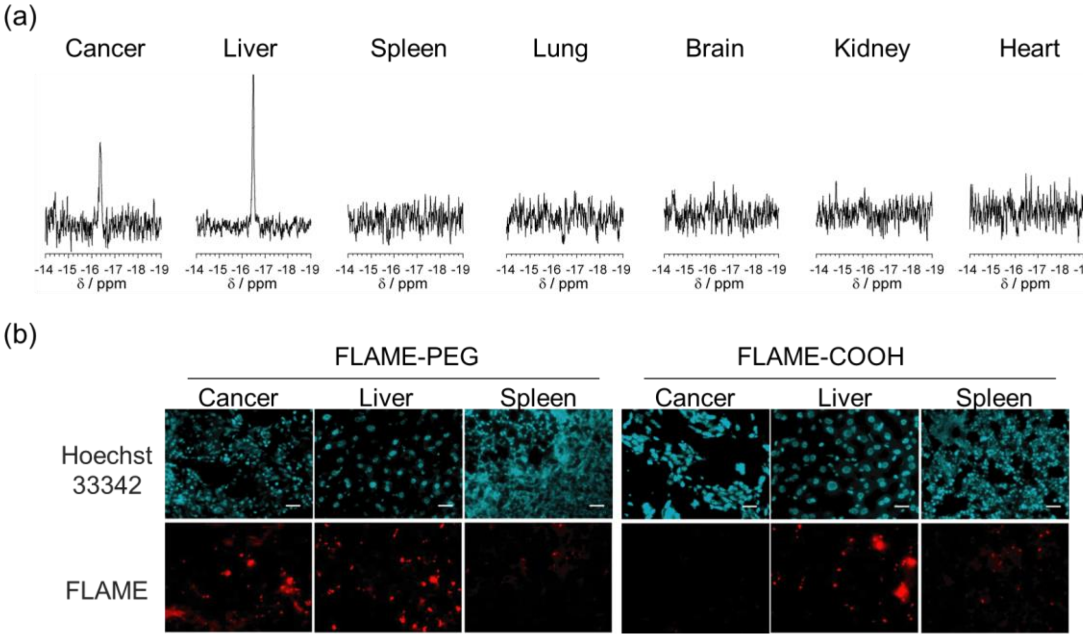

Figure 14. (a) ^{19}F NMR spectra of homogenized tissue samples of a FLAME-PEG-injected mouse. acquisition time: 8 min 32 s. (b) Fluorescence images of tumor, liver, and spleen sections. Scale bar: 20 µm. Excitation wavelength ranges were 510–550 nm for RITC and 330–385 nm for Hoechst33342.

Experimental Sections

Materials and instruments. General chemicals were of the highest grade available, supplied by Tokyo Chemical Industries, NOF Corporation, Wako Pure Chemical, and Aldrich Chemical Co., and used without further purification. NMR spectra and the the T_1 and the T_2 relaxation times were measured on a JEOL JNM-AL 400 instrument at 400 MHz for ^{1}H, at 100.4 MHz for ^{13}C NMR using tetramethylsilane as an internal standard, and at 376 MHz for ^{19}F NMR using sodium trifluoroacetate as an internal standard. Mass spectra were taken on a JEOL JMS-DX for fast atom bombardment and on a Waters LCT-Premier XE for ESI. Fluorescence spectra were recorded using a Hitachi F4500 spectrometer. The slit width was 5.0 nm for both excitation and emission. The photomultiplier voltage was 700 V. MR images were recorded on a Bruker Avance II 500WB spectrometer equipped with a wide bore (89 mm), 11.7-T magnet, and a micro-2.5-imaging probe head operating at frequencies of 500 MHz for ^{1}H and 471 MHz for ^{19}F measurements. A volume coil of 25 mm in diameter was used. Image acquisition and processing were carried out using the ParaVision software (Bruker

BioSpin). TEM images were acquired by using the HITACHI H-9000 (300 V). Particle size distribution and ζ-potential were measured by DLS on the particle analyzer nano partica SZ-100 from HORIBA. Fluorescence microscopic images were obtained using the IX71 (Olympus) for the inverted fluorescence microscope, Cool SNAP HQ (Photometrics) for the cooled CCD camera, and a light engine (Lumencor Spectra X®, Olympus) with emission filters (Semrock). The imaging software MetaMolph (Universal Imaging Corporation) was used for data analysis.

Synthesis of compounds

Preparation of F-NHS. F-COOH (compound **5**) was synthesized according to procedures described in Chapter 1. F-COOH (0.50 g, 1.9 mmol) was dissolved in dry DMF (15 mL) under argon atmosphere. Then, WSCD·HCl (0.54 g, 2.9 mmol), *N*-hydroxysuccinimide (0.33 g, 2.9 mmol), and dry TEA (0.83 mL, 5.7 mmol) were added to the solution. The mixture was stirred at RT under argon atmosphere. After the reaction solution was evaporated, the residue was dissolved in ethyl acetate (100 mL) and washed with 4% $NaHCO_3$ (aq.), 10% citric acid, water, and brine. The organic layer was dried over Na_2SO_4 and evaporated under reduced pressure. The crude F-COOH (0.47 g) was obtained as a white solid and used in the next step without further purification.

Preparation of F-Amp. The crude product F-NHS (70 mg) was dissolved in dry DMF (1.0 mL) under argon atmosphere. Then, ampicillin (81 mg, 0.23 mmol) and dry TEA (54 µL, 0.39 mmol) were added to the solution. The mixture was stirred at RT for 12 h. After the reaction solution was evaporated, the product was purified by RP-HPLC and eluted with H_2O/acetonitrile containing 0.1% formic acid to yield F-Amp (36 mg, y. 31%). ^1H NMR (CD_3OD, 400 MHz) δ 1.40 (s, 3H) 1.54 (s, 3H) 4.00 (t, 2H) 4.20 (s, 1H) 5.39 (d, 1H) 5.51 (dd, 1H) 5.76 (d, 1H) 7.28 (d, 1H) 7.33 (t, 2H) 7.43 (d, 2H) 7.48 (d, 2H) 8.00 (d, 2H) 8.65 (s, 1H) 8.87 (t, 1H) 9.23 (d, 1H); ^{13}C NMR (100 MHz, $CDCl_3$) δ 26.6, 29.9, 42.3, 55.2, 58.0, 63..6, 66.9, 70.2, 120.6, 126.9, 127.6, 128.3, 129.6, 133.0, 128.1, 150.3, 165.2, 168.4, 168.9, 170.0, 173.3; HRMS (ESI^-) *m/z*: 595.1433 (calculated for 595.1469).

Synthesis of Palmitic-NHS. Palmitic acid (1.5 g, 6.0 mmol, 1 eq) and WSCD·HCl (1.7 g, 9.0 mmol, 1.5 eq) were dissolved in dry DMF (60 mL) at 0°C, and *N*-hydroxysuccinimide (1.0 g, 9.0 mmol, 1.5 eq) was added. The mixture was stirred for 6 h at RT under argon atmosphere. The solvent was evaporated by using a rotary evaporator, and the obtained product was dissolved with ethyl acetate and washed with water and brine. The organic layer was dried over Na_2SO_4 and evaporated under reduced pressure. The product was dissolved in dichloromethane, purified by silica gel chromatography, and eluted with dichloromethane to afford Palmitic-NHS (1.1 g, y. 51%). ^{1}H NMR ($CDCl_3$, 400 MHz) δ 0.89 (s, 3H) 1.20–1.40 (m, 24H) 1.74 (dt, 2H), 2.62 (t, 2H), 2.85 (s, 4H).

Synthesis of Palmitic-NH$_2$. 1,2-Ethylenediamine (2.7 mL, 40 mmol) was added to CH_2Cl_2 (30 mL) under argon atmosphere at RT. Palmitic-NHS (0.71 g, 2 mmol, 1 eq) was added drop-wise to the solution. The mixture was stirred for 2 h. The solvent was diluted with $CHCl_3$ and washed with water and brine. The organic layer was dried over Na_2SO_4 and evaporated under pressure to afford Palmitic-NH$_2$ (0.60 g, quant.). ^{1}H NMR (400 MHz, $CDCl_3$) δ 0.89 (s, 3H) 1.22–1.29 (m, 24H) 1.64 (dt, 2H), 2.19 (t, 2H), 2.84 (t, 2H), 3.32 (t, 2H), 5.90 (s, 1H); MS (ESI$^+$) *m/z*: 299.19 (calculated for $[M+H]^+$: 299.40)

Synthesis of PAP. 4-Pyridylacetic acid hydrochloride (0.43 g, 5.0 mmol, 5 eq) was dissolved in dry DMF (30 mL) under argon atmosphere at RT. Then, WSCD·HCl (1.2 g, 6.0 mmol, 6 eq), hydroxybenzotriazole (0.92 g, 6 mmol, 6 eq), and dry triethylamine (1.3 mL, 9.3 mmol, 10 eq) were added to the solution. Palmitic-NH$_2$ (0.30 g, 1 mmol, 1 eq) was added to the mixture, which was then stirred for 15 h at 50°C. DMF was evaporated under reduced pressure. The residue was added to saturated $NaHCO_3$ (aq.); the precipitate was then collected and washed with saturated $NaHCO_3$ (aq.) and water. The product was recrystallized from MeOH to afford PAP (0.36 g, y. 85%). ^{1}H NMR (400 MHz, $CDCl_3$) δ 0.88 (s, 3H) 1.22–1.28 (m, 24H) 1.58 (dt, 2H), 2.13 (t, 2H), 3.38 (m, 4H), 3.50 (s, 2H), 5.97 (s, 1H), 6.56 (s, 1H), 7.22 (d, 2H), 8.56 (d, 2H); ^{13}C NMR (100 MHz, $CDCl_3$) δ 14.1, 22.7, 25.7, 25.7, 29.2, 29.3, 29.5, 29.6, 29.6, 29.7, 29.7, 31.9, 36.6, 36.6, 39.6, 41.0, 42.8, 42.9, 124.4, 150.0, 150.1, 170.1, 174.9; HRMS (FSB$^+$) *m/z*: 419.3437 (calculated for $[M+H]^+$: 418.3434)

Preparation of FLAME. RITC (5.0 mg) was reacted with 22 µL of APTES in 0.35 mL of ethanol under dark conditions for 48 h. DSPC (5.0 mg, 6.3 µmol) and PAP (0.33 mg, 0.79 µmol) were dissolved in 3 mL of chloroform at 65 °C. The organic solvent was evaporated in a rotary evaporator at 65°C to obtain a thin film; solvent traces were removed by maintaining the lipid film under vacuum for 12 h. The film was hydrated with 3 mL of water using a bath-type sonicator for 10 min at 65°C. Then, 30 µL of PFCE was added to the emulsion, followed by homogenization (T10 basic ULTRA TURRAX, IKA) for 10 min and sonication by using a bath-type sonicator (Branson 1250) for 120 min. The emulsion was filtered with a 0.45-µm filter (hydrophilic PFPE, Millipore). Water (12 mL) and TEOS (0.10 mL) was added to the emulsion, and the mixture was then stirred for 48 h at RT. For fluorescence detection of the particles, 10 µL of RITC-conjugate APTES solution was then added and the solution was stirred for 24 h. The product of the silica-coated emulsion (FLAME) was purified by centrifugation (14,000 × *g*, 4°C, 30 min) and washed 3 times with water (20 mL) and isopropyl alcohol (20 mL).

Preparation of FLAME-NH$_2$. The obtained FLAME nanoparticles were dispersed in isopropyl alcohol (40 mL) under argon atmosphere. After the mixture was heated to 80 °C, APTES (0.60 mL) was added, and the solution was stirred for 3 h. The product was separated by centrifugation (14,000 × *g*, 4 °C, 30 min), washed 3 times with ethanol (20 mL) and dry DMF (10 mL), and finally dispersed in dry DMF (10 mL).

Preparation of FLAME-COOH. FLAME-NH$_2$ dispersed in dry DMF (1.0 mL) was added slowly to a flask containing 2.0 M succinic anhydride in dry DMF under argon atmosphere. Anhydrous triethylamine was added to the mixture, which was then stirred for 24 h. The product was separated by centrifugation (14,000 × *g*, 4°C, 30 min) and washed 3 times with DMF (3.0 mL) and water (3.0 mL). FLAME-COOH nanoparticles were finally dispersed in water. The nanoparticle solution was filtered with a 0.8-µm filter (mixed cellulose esters, Millipore).

Preparation of FLAME-NHS. FLAME-COOH nanoparticles were dispersed in dry DMF (1.0 mL) under argon atmosphere. Then, WSCD·HCl (0.44 mg, 2.3 µmol), *N*-hydroxysuccinimide (0.27 mg, 2.3 µmol), and dry TEA (0.32 µL, 2.3 µmol) were added to the solution. The mixture was stirred for 3 h at 30 °C. The product was separated by centrifugation (14,000 × *g*, 4°C, 30 min), washed twice with dry DMF, and finally dispersed in dry DMF.

Preparation of ampicillin-modified FLAME (FLAME-Amp). FLAME-NHS was dispersed in dry DMF (1.0 mL) under argon atmosphere. Then, ampicillin (0.80 mg, 2.3 µmol) and dry TEA (0.32 µL, 2.3 µmol) were added to the solution. The mixture was stirred for 3 h at 30°C. The product was separated by centrifugation (14,000 × *g*, 4°C, 30 min), washed twice with DMF (1.0 mL), and finally dispersed in water (1.0 mL).

Preparation of PEGylated FLAME (FLAME-PEG). FLAME-NH$_2$ dispersed in dry DMF (1.0 mL) was mixed with 0.30 g of methoxy-PEG-(CH$_2$)$_5$-COO-NHS (MW 5,000, SUNBRIGHT® ME-050HS, NOF Corporation). Then, 35 mL of anhydrous TEA was added to the resulting solution and stirred at 40°C for 48 h. The resulting FLAME-PEG was collected by centrifugation (14,000 × *g*, 4°C, 30 min) and washed 3 times with DMF (3.0 mL) and water (3.0 mL) to remove any unreacted PEG. The nanoparticle solution was filtered with a 0.8-µm filter (mixed cellulose esters, Millipore).

^{19}F NMR relaxation time measurements. Nanoparticles were prepared in water containing 5% D_2O. The T_2 was measured by employing the spin-echo method.

MRI measurements. The RARE method was used for ^{1}H and ^{19}F MRI. For ^{1}H MRI, the matrix size was 128 × 128, slice thickness was 2 mm, and the RARE factor was 8. T_R and $T_{E,eff}$ were 1,000 ms and 31.4 ms, respectively. The number of averages was 1. For ^{19}F MRI, the matrix size was 64 × 64, slice thickness was 30 mm, and the RARE factor was 16. T_R and $T_{E,\mathrm{eff}}$ were 1,000 ms and 80 ms, respectively. The number of averages was 512.

DLS measurements. Particle size, size distribution, and ζ-potential of the obtained nanoparticles were measured at 25 °C with a 580 nm laser at a scattering angle of 90° for DLS size measurements and 173° for ζ-potential measurements. For the DLS size measurements, FLAME nanoparticles were suspended in water or ethanol. Suspensions of each material were prepared in H_2O for ζ-potential measurements.

In vitro MBP-BL assay using FLAME-Amp. The pET-21b(+)-MBP-BL was prepared according to our previously reported procedure.[4] Ampicillin (0.10 g mL^{-1}, 10 µL) and stocked cells (MBP-BL) were added to 10 mL of Luria-Bertani medium, followed by incubation for 16 h at 37°C. The culture solution was added to 50 mL of Luria-Bertani medium and incubated for 4 h at 37°C. Isopropyl-D-thiogalactopyranoside (1.0 M, 20 µL) was added to the culture solution, and the solution was then incubated for 18 h at 25 °C. The supernatant was obtained by centrifugation (3,600 × *g*, 20 min, 4°C) and discarded. Then, 30 mL of column buffer (20 mM HEPES, pH 7.4, 0.20 M NaCl, 1.0 mM EDTA) was added to the pellet, and the suspension was sonicated using a probe-type sonicator (SONIFIRE250, Duty Cycle: 50%, Output Control: 5). The supernatant was collected from the suspension by centrifugation (20,000 × *g*, 30 min, 4°C) and then applied to 1.0 mL of amylose resin equilibrated with column buffer. The amylose resin was then washed with 20 mL of column buffer. A dispersion of FLAME-Amp (C_{PFCE} = 9.7 mM, 500 µL) in column buffer was applied to the amylose resin and incubated for 1 h at 4°C. The resin was washed with 20 mL of column buffer. Then, a fraction (0.5–1.0 mL) of the protein solution was collected by using the elution buffer (20 mM HEPES, pH 7.4, 0.20 M NaCl, 1.0 mM EDTA, 10 mM maltose).

^{19}F MRI detection of gene expression in HEK293T cells with FLAME-Amp. HEK293T cells were cultured in DMEM (Invitrogen) containing 10% fetal bovine serum at 37°C under 5% CO_2. The cells were transfected with a plasmid encoding the BL-tagged EGFR by using Lipofectamine 2000 (Invitrogen). After 6 h, the culture medium was replaced with DMEM containing 10% fetal bovine serum and kanamycin (0.10 mg mL^{-1}), and cells were incubated at 37 °C for 24 h under 5% CO_2. Next, the cells were washed with PBS, harvested with trypsin-EDTA, washed with PBS, and mixed with PBS containing FLAME-Amp, FLAME-COOH (C_{PFCE} = 2.6 mM), and F-Amp ($C_{\mathrm{F\text{-}Amp}}$ = 9.6 mM). After incubation at 4°C for 5 min, the cells were diluted with PBS, washed with PBS 3 times by centrifugation (500 × g, 3 min), and dispersed in PBS containing 5% D_2O (500 µL). The cells were transferred into a glass tube (ϕ 8 mm), and ^{19}F NMR and ^{1}H/^{19}F MRI were then performed. For the ^{1}H MRI, the matrix size was 128 × 128 with a field of view of 50 × 50 mm, a slice depth of 1 mm, and a RARE factor of 16.

Tumor model and in vivo experimental procedure for MRI. At 7–9 weeks after inoculation of 1.0×10^5 cells in the flank, female mice (Balb/cA, 20 to 25 g bodyweight) bearing colon-26 tumors (size of the tumor of about 2,400 mm^3) were administered FLAME-PEG or FLAME-COOH (0.20 mL, C_{PFCE} = 2.6 mM) through tail vein injection. For MRI measurements, mice were anesthetized using 2.0% isoflurane at a flow rate of 0.2 L min^{-1} and scanned.

Fluorescence imaging of tumor and organ sections. After MRI, mice were killed followed by perfusion fixation. Then, tumors, livers, and spleens were harvested and fixed with 4% formaldehyde. The tissues were transferred to PBS containing 30% sucrose for over 12 h and embedded in optimal cutting temperature compound. The tissues were sectioned by using a cryomicrotome (Leica CM3050S) at a thickness of 10 µm and mounted on glass slides. The sections were co-stained with Hoechst33342 (100 ng mL^{-1}) for 30 min. Excitation wavelength ranges were 510–550 nm for RITC and 330–385 nm for Hoechst33342.

Preparation of mouse organ lysates. After MRI, mice were killed. Then, livers, spleens, lungs, brains, kidneys, hearts, and tumors were harvested and fixed with 4% formaldehyde. These organs were homogenized in 100 mM PBS (pH 7.4) using a homogenizer. D_2O was added to the homogenates and ^{19}F NMR spectra were acquired.

References

1. Matagne, A.; Lamotte-Brasseur, J.; Frére, J.-M. *Biochem. J.* **1998**, *598*, 581–598.
2. Belaaouaj, A.; Lapoumeroulie, C.; Caniça, M. M.; Vedel, G.; Névot, P.; Krishnamoorthy, R.; Paul, G. *FEMS Microbiol. Lett*. **1994**, *120,* 75–80.
3. Farzaneh, S.; Chaibi, E. L. B.; Peduzzi, J.; Barthelemy, M.; Labia, R.; Blazquez, J.; Baquero, F. *Antimicrob. Agents Chemother* **1996**, *40*, 2434–2436.
4. Mizukami, S.; Watanabe, S.; Hori, Y.; Kikuchi, K. *J. Am. Chem. Soc.* **2009**, *131*, 5016–5017.
5. Mizukami, S.; Watanabe, S.; Akimoto, Y.; Kikuchi, K. *J. Am. Chem. Soc.* **2012**, *134*, 1623–1629.
6. Watanabe, S.; Mizukami, S.; Akimoto, Y.; Hori, Y.; Kikuchi, K. *Chem. Eur. J.* **2011**, *17*, 8342–8349.
7. Yoshimura, A.; Mizukami, S.; Hori, Y.; Watanabe, S.; Kikuchi, K. *ChemBioChem* **2011**, *12*, 1031–1034.
8. Mizukami, S.; Yamamoto, T.; Yoshimura, A.; Watanabe, S.; Kikuchi, K. *Angew. Chem. Int. Ed.* **2011**, *50*, 8750–8752.
9. Sadhu, K. K.; Mizukami, S.; Watanabe, S.; Kikuchi, K. *Mol. BioSyst.* **2011**, *7*, 1766–1772.
10. Ruiz-Cabello, J.; Barnett, B. P.; Bottomley, P. A.; Bulte, J. W. M. *NMR Biomed*. **2011**, *2*, 114–129.
11. Ahrens, E. T.; Flores, R.; Xu, H.; Morel, P. A. *Nat. Biotechnol*. **2005**, *23*, 983–987.
12. Srinivas, M.; Boehm-Sturm, P.; Figdor, C. G.; de Vries, I. J.; Hoehn, M. *Biomaterials* **2012**, *33*, 8830–8840.
13. Liu, J.; Lee, L. S. *Environ. Sci. Technol.* **2007**, *41*, 5357–5362.
14. Tanaka, K.; Kitamura, N.; Chujo, Y. *Bioconjug. Chem.* **2011**, *22*, 1484–1490.
15. Takaoka, Y.; Sakamoto, T.; Tsukiji, S.; Narazaki, M.; Matsuda, T.; Tochio, H.; Shirakawa, M.; Hamachi, I. *Nat. Chem*. **2009**, *1*, 557–561.
16. Huang, X.; Huang, G.; Zhang, S.; Sagiyama, K.; Togao, O.; Ma, X.; Wang, Y.; Li, Y.; Soesbe, T. C.; Sumer, B. D.; Takahashi, M.; Sherry, A. D.; Gao, J. *Angew. Chem. Int. Ed.* **2013**, *52*, 8074–8078.
17. Tanaka, K.; Kitamura, N.; Naka, K.; Chujo, Y. *Bioconjug. Chem*. **2008**, *22*, 1484–1490.
18. Flögel, U.; Ding, Z.; Hardung, H.; Jander, S.; Reichmann, G.; Jacoby, C.; Schubert, R.; Schrader, J. *Circulation* **2008**, *118*, 140–148.
19. Díaz-López, R.; Tsapis, N.; Fattal, E. *Pharm. Res.* **2010**, *27*, 1–16.
20. Ahrens, E. T.; Bulte, J. W. M. *Nat. Rev. Immunol*. **2013**, *13*, 755–763.

21. Kabalnov, A. S.; Shchukin, E. D. *Adv. Colloid Interface Sci.* **1992**, *38*, 69–97.
22. Freire, M. G.; Dias, A. M. a; Coelho, M. A. Z.; Coutinho, J. A. P.; Marrucho, I. M. J. *Colloid Interface Sci.* **2005**, *286*, 224–232.
23. Arlauskas, R. A.; Klein, D. H.; Weers, J. G.; Diego, S. *Art. Cells, Blood Subs., Immob. Biotech.* **1994**, *22*, 1317–1323.
24. Vivero-Escoto, J. L.; Huxford-Phillips, R. C.; Lin, W. *Chem. Soc. Rev.* **2012**, *41*, 2673–2685.
25. Kunzmann, A.; Andersson, B.; Vogt, C.; Feliu, N.; Ye, F.; Gabrielsson, S.; Toprak, M. S.; Buerki-Thurnherr, T.; Laurent, S.; Vahter, M.; Krug, H.; Muhammed, M.; Scheynius, A.; Fadeel, B. *Toxicol. Appl. Pharmacol.* **2011**, *253*, 81–93.
26. Li, M.; Lam, J. W. Y.; Mahtab, F.; Chen, S.; Zhang, W.; Hong, Y.; Xiong, J.; Zheng, Q.; Tang, B. Z. *J. Mater. Chem. B* **2013**, *1*, 676–684.
27. Korzeniowska, B.; Nooney, R.; Wencel, D.; McDonagh, C. *Nanotechnology* **2013**, *24*, 442002.
28. Wu, X.; Chang, S.; Sun, X.; Guo, Z.; Li, Y.; Tang, J.; Shen, Y.; Shi, J.; Tian, H.; Zhu, W. *Chem. Sci.* **2013**, *4*, 1221–1228.
29. Shi, Y.; Zhang, H.; Yue, Z.; Zhang, Z.; Teng, K.-S.; Li, M.-J.; Yi, C.; Yang, M. *Nanotechnology* **2013**, *24*, 375501.
30. Westcott, S. L.; Oldenburg, S. J.; Lee, T. R.; Halas, N. J. *Langmuir* **1998**, *7463*, 5396–5401.
31. Qhobosheane, M.; Santra, S.; Zhang, P.; Tan, W. *Analyst* **2001**, *126*, 1274–1278.
32. Beck, C.; Härtl, W.; Hempelmann, R. *Angew. Chem. Int. Ed.* **1999**, *38*, 1297–1300.
33. Watanabe, S.; Ozaki, H.; Mitsuhashi, K.; Nakahama, S. *Makromol. Chem.* **1992**, *193*, 2781–2792.
34. Wang, S.; Zhang, M.; Wang, D.; Zhang, W.; Liu, S. *Microporous Mesoporous Mater.* **2011**, *139*, 1–7.
35. Guana, C.; Lib, P.; Riggs, P. D.; Inouyeb, H. *Gene* **1988**, *67*, 21–30.
36. Maina, C. V; Riggs, P. D.; Iii, A. G. G.; Slatko, B. E.; Moran, L. S.; Tagliamonte, J. A. McReynolds, L. A.; di Guan, C. *Gene* **1988**, *74*, 365–373.
37. Matsumura, Y.; Maeda, H. *Cancer Res.* **1986**, *46*, 6387–6392.
38. Maeda, H. *Bioconjug. Chem.* **2010**, *21*, 797–802.
39. Maeda, H. *Adv. Enzyme Regul.* **2001**, *41*, 189–207.
40. Maeda, H.; Wu, J.; Sawa, T.; Matsumura, Y.; Hori, K. *J. Control. Release* **2000**, *65*, 271–284.
41. Hashizume, H.; Baluk, P.; Morikawa, S.; McLean, J. W.; Thurston, G.; Roberge, S.; Jain, R. K.; McDonald, D. M. *Am. J. Pathol.* **2000**, *156*, 1363–1380.

42. Normann, S. J. *Infect. Immun.* **1970**, *1*, 327–333.
43. Yoo, B.; Cheal, S. M.; Torchon, G.; Dilhas, A.; Yang, G.; Pu, J.; Punzalan, B.; Larson, S. M.; Ouerfelli, O. *Bioconjug. Chem.* **2013**, *24*, 2088–2103.
44. Akerman, M. E.; Chan, W. C. W.; Laakkonen, P.; Bhatia, S. N.; Ruoslahti, E. *Proc. Natl. Acad. Sci. U. S. A.* **2002**, *99*, 12617–12621.
45. Brannon-Peppas, L.; Blanchette, J. O. *Adv. Drug Deliv. Rev.* **2004**, *56*, 1649–1659.
46. Liu, J.; Yu, M.; Ning, X.; Zhou, C.; Yang, S.; Zheng, J. *Angew. Chem. Int. Ed.* **2013**, *52*, 12572–12576.
47. Pirollo, K. F.; Chang, E. H. *Trends Biotechnol*. **2008**, *26*, 552–558.
48. Yue-Jian, C.; Juan, T.; Fei, X.; Jia-Bi, Z.; Ning, G.; Yi-Hua, Z.; Ye, D.; Liang, G. *Drug Dev. Ind. Pharm*. **2010**, *36*, 1235–1244.
49. Jokerst, J. V; Lobovkina, T.; Zare, R. N.; Gambhir, S. S. *Nanomedicine* **2011**, *6*, 715–728.
50. Sanada, Y.; Akiba, I.; Sakurai, K.; Shiraishi, K.; Yokoyama, M.; Mylonas, E.; Ohta, N.; Yagi, N.; Shinohara, Y.; Amemiya, Y. *J. Am. Chem. Soc.* **2013**, *135*, 2574–2582.
51. Koole, R.; van Schooneveld, M. M.; Hilhorst, J.; Castermans, K.; Cormode, D. P.; Strijkers, G. J.; de Mello Donegá, C.; Vanmaekelbergh, D.; Griffioen, A. W.; Nicolay, K.; Fayad, Z. A.; Meijerink, A.; Mulder, W. J. M. *Bioconjug. Chem.* **2008**, *19*, 2471–2479.
52. Feshitan, J. A.; Boss, M. A.; Borden, M. A. *Langmuir* **2012**, *28*, 15336–43.
53. Gref, R.; Dombb, A.; Quelled, P.; Blunk, T.; Miillerd, R. H.; Verbavatz, J. M.; Langerf, R. *Adv. Drug Deliv. Rev.* **1995**, *16*, 215–233.
54. Stolnik, S.; Illum, L.; Davis, S. S. *Adv. Drug Deliv. Rev.* **1995**, *16*, 195–214.

Chapter 3 Development of a reduction-responsive ^{19}F MRI nanoprobe (FSG)

In the previous chapter, the author described novel contrast agents with a core-shell structure, FLAMEs, for highly sensitive ^{19}F MRI. Next, the author attempted to develop a stimuli-responsive ^{19}F MRI nanoprobe for further in vivo biomedical applications.

3-1 Design strategy and hypothesis for stimuli-responsive ^{19}F MRI nanoprobe based on PRE effect

The author focused on the PRE effect of the Gd^{3+} complex for controlling the T_2 of FLAME.[1–6] The PRE for the Γ_2 transverse relaxation rate is conventionally described by the Solomon—Bloembergen equation (1):[7–10]

$$\Gamma_2 = \frac{1}{15}\left(\frac{\mu_0}{4\pi}\right)^2 \gamma_I^2 g^2 \mu_B^2 s(s+1)\{4J_{SB}(0)+3J_{SB}(\omega_I)\} \tag{1}$$

Where s is the electron spin quantum number, g is the electron g-factor, γ_I is the fluorine gyromagnetic ratio, μ_o is the permeability of a vacuum, μ_B is the magnetic moment of the free electron, and $\omega_I/2\pi$ is the Larmor frequency of the fluorine. $J_{SB}(\omega)$ is the spectral density function:[11–13]

$$J_{SB}(\omega) = r^{-6}\frac{\tau_c}{1+(\omega\tau_c)^2} \tag{2}$$

The correlation time τ_c is defined as $(\tau_r^{-1} + \tau_s^{-1})^{-1}$, where τ_r is the rotational correlation time of the molecule, and τ_s is the effective electron relaxation time. As shown in eq. (2), the magnitude of the PRE is proportional to r^{-6}.

The distance between fluorine and the Gd^{3+} of Gd-FC-lac was calculated as 23 Å by molecular mechanics method. In contrast, the distance between PFCE molecules in a FLAME and the Gd^{3+} on the shell surface was greater than 60 Å because of the thickness of the silica shell. Thus, it is predicted that the Γ_2 of FLAME is extremely low, corresponding to 0.32% of that of Gd-FC-lac. However, the intermolecular Γ_2 is linearly dependent on the concentration of Gd^{3+} complex.[14] The addition of paramagnetic species causes an increase in the transverse relaxation rate ($1/T_2$). $1/T_2$ is defined as R_2.

$$\Gamma_2 = R_{2,\text{paramagnetic}} - R_{2,\text{diamagnetic}} = r_2[Gd^{3+}] - R_{2,\text{diamagnetic}} \tag{3}$$

Γ_2 is explained in the Equation (3), where $R_{2,\text{paramagnetic}}$ is the observed ^{19}F relaxation rate in the presence of a paramagnetic ion and $R_{2,\mathrm{diamagnetic}}$ is the diamagnetic relaxation rate in the absence of a paramagnetic ion. Although $R_{2,\mathrm{paramagnetic}}$ represents the sum of the intramolecular and intermolecular PRE effects, it is not necessary to consider the intramolecular PRE effect in the case of FLAME. r_2 is defined as the slope of this dependence in units of $\mathrm{mM}^{-1}\cdot\mathrm{s}^{-1}$.

Furthermore, the T_2 of PFCE in FLAME would be affected by the combined PRE effect of all Gd^{3+} ions on the silica surface because of the free molecular mobility of PFCE in the nanoparticle.[12,13] Therefore, the T_2 of a PFCE molecule in FLAME can be potentially decreased by a large number of Gd^{3+} complexes on the surface of the silica shell.

To test this hypothesis, the author synthesized Gd^{3+} complex-functionalized FLAME (F-Gd) under different concentrations of Gd^{3+} ions (Scheme 1).

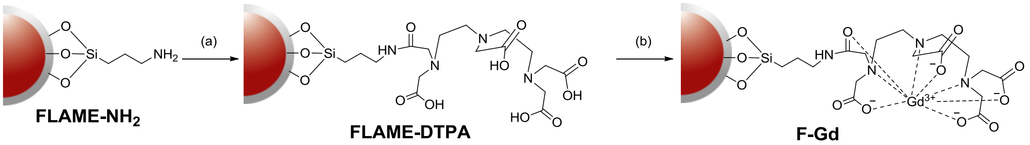

Scheme 1. Synthetic route to FLAME-DTPA-Gd. (a) DTPA bisanhydride, TEA, DMF (b) $GdCl_3\cdot 6H_2O$, methanol

Table 1. Synthetic conditions for FLAME-DTPA-Gd and ζ-potential of F-Gd.

Materials	[Gd^{3+}] for synthesis of FLAME-DTPA-Gd / mM	ξ-potential / mV
FLAME-DTPA	0	-38.8 ± 0.9
F-Gd1	1	-34.0 ± 1.0
F-Gd2	10	-22.5 ± 1.4
F-Gd3	100	-21.6 ± 1.6

^{19}F NMR analyses of F-Gd nanoparticles were performed. Although the ^{19}F NMR spectrum of Gd^{3+}-free FLAME showed a sharp single peak, the corresponding peak in the ^{19}F NMR spectrum of F-Gd1, F-Gd2, and F-Gd3 was broader because of the

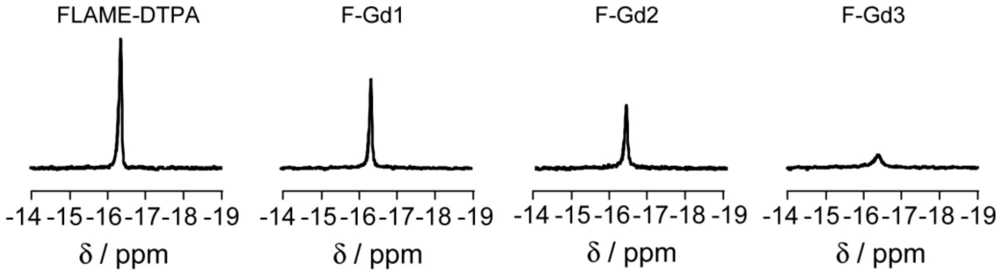

Figure 1. ^{19}F NMR spectra and T_2 measurements of F-Gd nanoparticles (C_{PFCE} = 600 μM). The accumulation time was 1 min 22 s.

Table 2. T_2 measurements of F-Gd nanoparticles.

Materials	T_2 / ms
FLAME-DTPA	222 ± 11
F-Gd1	19 ± 5
F-Gd2	13 ± 2
F-Gd3	8 ± 5

intramolecular PRE effect (Figure 1). The T_2 values of PFCE decreased in a Gd^{3+}-concentration dependent manner (Table 2).

Next, these samples were measured by ^{19}F MRI under different $T_{E,\,eff}$ to weight the T_2 difference (Figure 2). As a result, almost no ^{19}F MRI signals were observed from F-Gd1, F-Gd2, and F-Gd3, although a few ^{19}F MRI signals were detected from F-Gd1 at an echo time of 25.6 ms. These results demonstrated that Gd^{3+} complexes on the surface of silica shell had a sufficiently strong PRE effect to attenuate the ^{19}F MRI signal of FLAME.

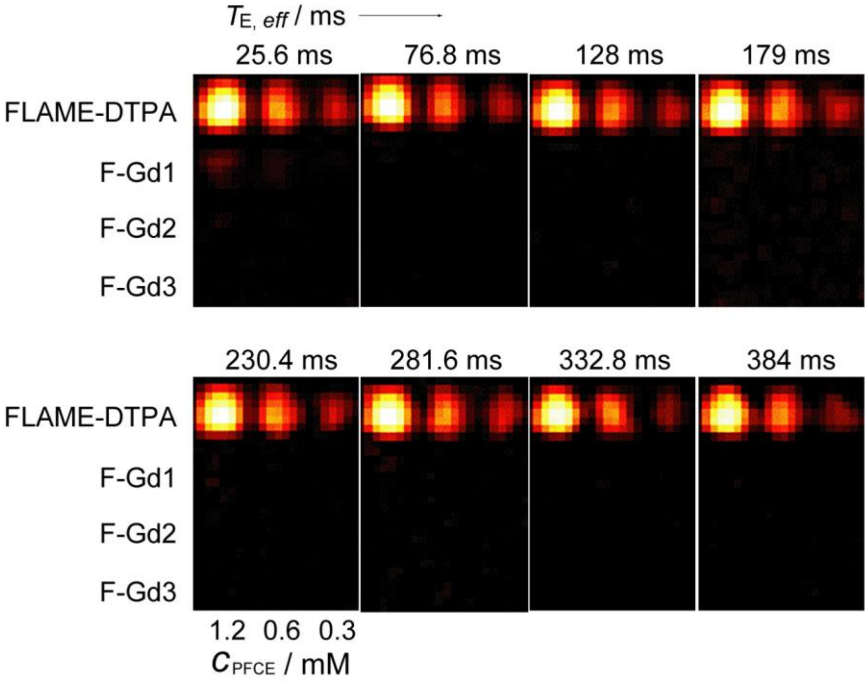

Figure 2. ^{19}F MRI measurement of FLAME-DTPA-Gd nanoparticles. The matrix size was 128 × 64, and the slice thickness was 30 mm. T_R was 1000 ms. The NEX was 64. The acquisition time was 12 min 48 s.

3-2 Development of reduction-responsive ^{19}F MRI nanoprobe (FSG)

In this chapter, the author developed a stimulus-responsive ^{19}F MRI nanoprobe to apply a Gd^{3+}-based design strategy as a turn-on signal switch (Figure 3).

Biological redox reactions play crucial roles in many biological processes. Abnormal levels of redox reactions are implicated in various disease states including liver damage, skin lesions, and slow growth, *etc*.[15–22] Therefore, it is important to monitor biological redox reactions,[22–30] and the development of reduction-responsive ^{19}F MRI probes is important in the field of MR imaging.

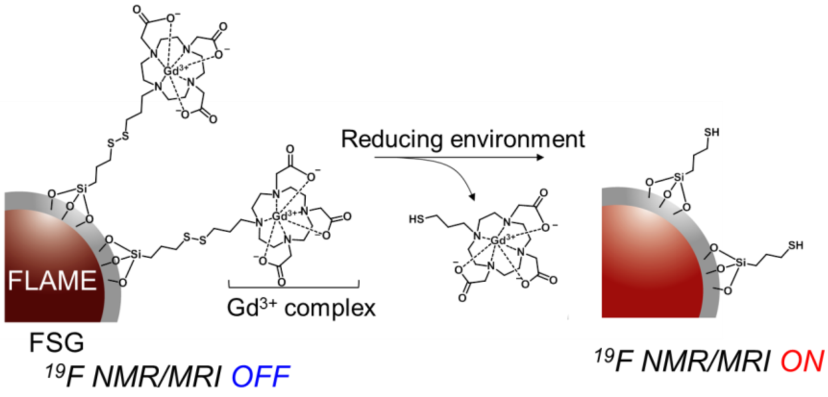

Figure 3. Structure of FSG and principles of ^{19}F MRI detection of reductive reactions.

Herein, the author reports the design and synthesis of a novel ^{19}F MRI nanoprobe, FLAME-SS-Gd (FSG), which detects the reduction level. FSG consists of FLAME and Gd^{3+} complexes conjugated by a short disulfide-containing linker. Cleavage of the disulfide linker by reductive reactions allows the Gd^{3+} complexes to diffuse from

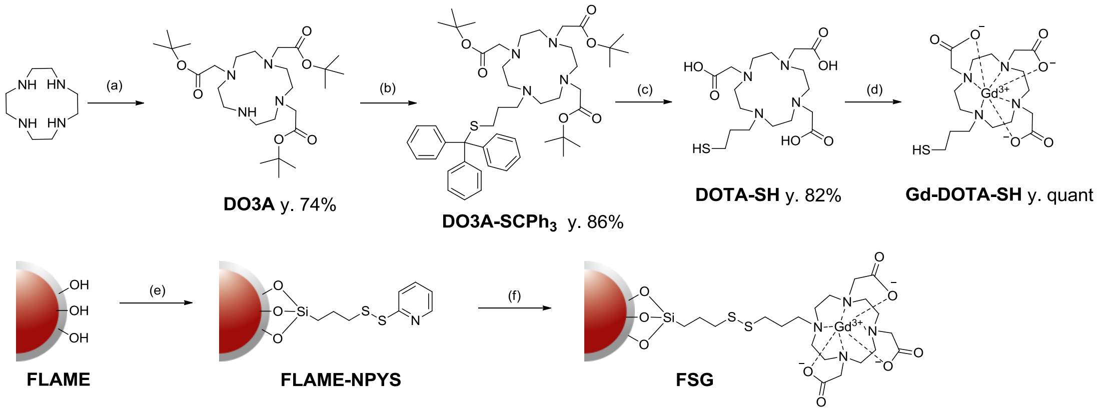

Scheme 2. Synthetic route to FLAME-SS-DOTA-Gd. (a) *tert*-butyl bromoacetate, K_2CO_3, MeCN; (b) 1-bromo-3-tritylthiopropane, K_2CO_3, MeCN; (c) TFA, triethylsilane, butanethiol; (d) $GdCl_3 \cdot 6H_2O$, methanol; (e) TMOS-Npys, isopropanol; (f) Gd-DOTA-SH, MeOH

FLAME, resulting in a decrease in intermolecular PRE effect-mediated quenching and in a specific increase in ^{19}F MRI signal intensity.

The synthetic scheme of FSG is presented in Scheme 2. The author prepared FSG1~3, which has a different amount of Gd^{3+} complexes on the FLAME for optimization of the ^{19}F MRI nanoprobe (Table 3). The amounts of Gd^{3+} in FSG were quantified by ICP-MS.

Table 3. Synthetic conditions for FSG, ζ-potentials of FSG, and molar ratios of PFCE to Gd^{3+}.

Materials	[TMOS-Npys] / mM	[Gd-DOTA-SH] / mM	ζ-potential / mV	n_{Gd}/n_{PFCE}
FSG1	0.4	2	-12.6 ± 2.4	0.011
FSG2	4	20	3.9 ± 1.4	0.026
FSG3	40	200	5.7 ± 1.5	0.038

Then, the effect of reductive stress on the nanoparticles was tested using a chemical reductant, TCEP.[31,32] FSG nanoparticles were incubated with TCEP, and the ^{19}F NMR peak was obtained (Figure 4a). The ^{19}F NMR spectra of FSG without TCEP were broader in descending order of Gd^{3+} content because of the intramolecular PRE effect. In contrast, a single strong ^{19}F NMR peak appeared at approximately -16.4 ppm from FSG treated with TCEP.

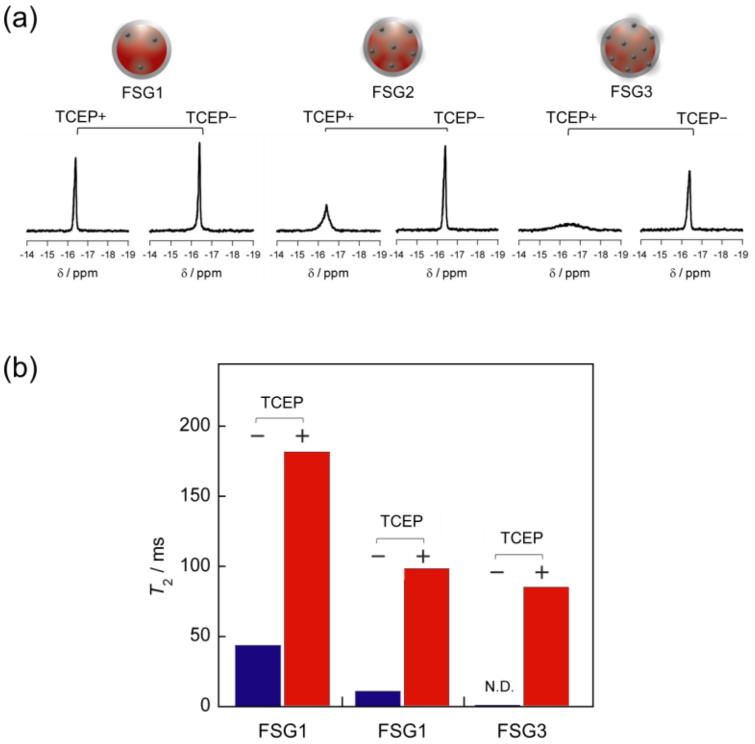

Figure 4. (a) ^{19}F NMR spectra of FSG incubated with or without TCEP. C_{PFCE}: 0.6 mM, C_{TCEP}: 1 mM, incubation time: 4 h, accumulation time: 1 min 22s. (b) T_2 of FSG incubated with or without TCEP. N.D. means that the value could not be determined.

These results are compatible with the T_2 measurements shown in Figure 4b. The T_2 of fluorine atoms was largely decreased and that of FSG3 was not precisely determined because of the overwhelming PRE effect. After reductive reactions, the T_2 was considerably increased.

Next, ^{19}F MRI images of FSG nanoparticles with TCEP are shown in Figure 5a. ^{19}F MR images are obtained at different $T_{E,eff}$ to weight the T_2 difference.[33–36] Although FSG2 and FSG3 showed no signal in the ^{19}F MRI phantom images, reductive reactions with TCEP induced a noticeable signal enhancement. Although ^{19}F MRI signal enhancement of FSG1 could be observed, the ^{19}F MRI signal was also detected in the

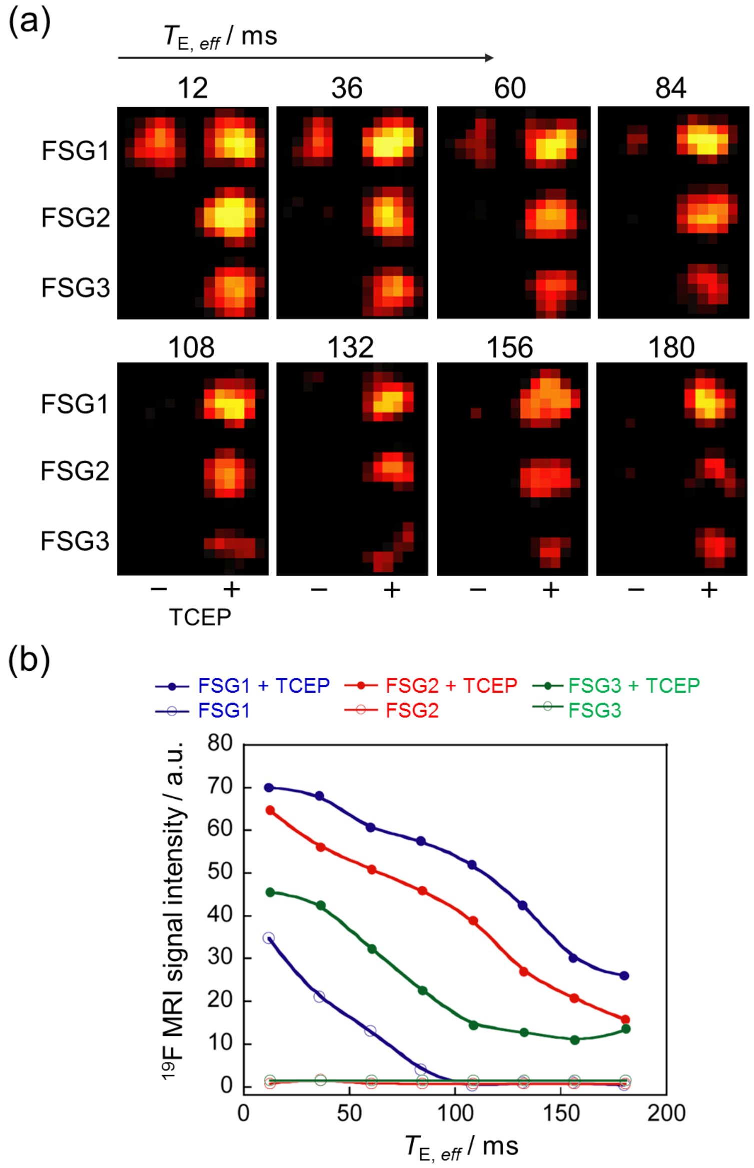

Figure 5. ^{19}F MRI measurements of FSG in the presence or absence of TCEP. C_{PFCE}: 0.6 mM, C_{TCEP}: acquisition time: 25 min 36 s. T_R: 3000 ms. (b) ^{19}F MRI signal intensity of FSG at the different T_E.

absence of TCEP at the short echo time. Furthermore, the increased of echo time was able to decrease undesirable ^{19}F MRI signals. The ^{19}F MRI signal intensity of FSG is shown in Figure 5b. These results indicate that no ^{19}F MRI signal of FSG1 was detected at an echo time of 108 ms and the highest-contrast image of FSG2 was obtained at an echo time of 12 ms. Therefore, FSG2 is the most suitable for reduction-responsive ^{19}F MRI nanoprobe. The author demonstrated that the PRE-based probe design strategy was useful for the nanoparticle-based ^{19}F MRI contrast agent, FLAME.

As shown in Figure 6a, the ^{19}F MRI signals of FSG2 were increased in a TCEP concentration-dependent manner. These results show that FSG2 has the potential to monitor the reduction level as a ^{19}F MRI nanoprobe.

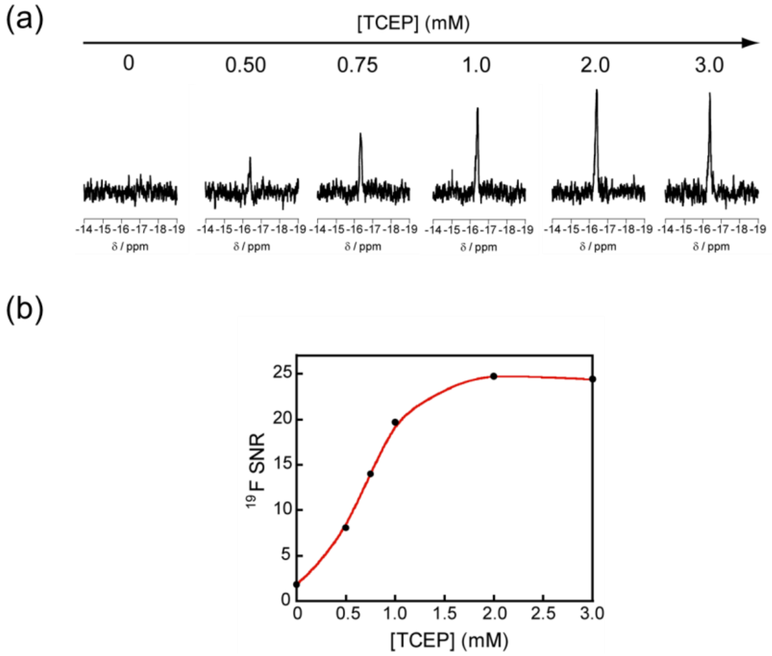

Figure 6. (a) ^{19}F NMR spectra of FSG2 incubated with different concentrations of TCEP. C_{PFCE}: 0.15 mM, incubation time: 3 h, accumulation time: 10 min 55s. (b) ^{19}F NMR signal intensity of FSG2.

Finally, ^{19}F NMR analyses of reductive reaction were performed by treating FSG2 with thiol-based reduction agents such as GSH, Cys, and DTT (Figure 7). As a result, ^{19}F NMR signals of FSG2 were increased by the addition of reduction agents. In particular, addition of GSH induced the highest enhancement of the ^{19}F NMR signal. GSH, which is the most abundant intracellular nonprotein thiol (0.5–10 mM), serves many cellular functions, including maintenance of intracellular redox activities, xenobiotic metabolism, intracellular signal transduction, and gene regulation.[15,16,37–40]

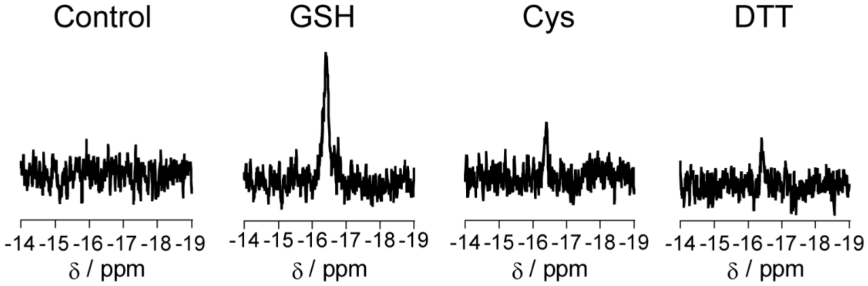

Figure 7. ^{19}F NMR spectra of FSG (0.15 mM) incubated with several types of thiol-based reduction agent (3 mM). GSH, Cys, and DTT are glutathione, cysteine, and dithiothreitol, respectively. The accumulation time was 1 min 22 s.

Therefore, ^{19}F MRI detection of intracellular GSH level with FSG would be useful for these biomedical applications.

Experimental Sections

Materials and instruments. General chemicals were of the highest grade available, supplied by Tokyo Chemical Industries, NOF Corporation, Wako Pure Chemical, and Aldrich Chemical Co., and used without further purification. NMR spectra and the T_1 and the T_2 relaxation times were measured on a JEOL JNM-AL 400 instrument at 400 MHz for ^{1}H, at 100.4 MHz for ^{13}C NMR using tetramethylsilane as an internal standard, and at 376 MHz for ^{19}F NMR using sodium trifluoroacetate as an internal standard. Mass spectra were obtained on a Waters LCT-Premier XE for ESI. MR images were recorded on a Bruker Avance II 500WB spectrometer equipped with a wide-bore (89 mm), 11.7-T magnet and a micro-2.5-imaging probe head operating at frequencies of 500 MHz for ^{1}H and 471 MHz for ^{19}F measurements. A volume coil with a diameter of 25 mm was used. Image acquisition and processing were conducted using ParaVision software (Bruker BioSpin). Particle size distribution and ζ-potential were measured by DLS on a nano partica SZ-100 particle analyzer from Horiba.

Synthesis of compounds

Preparation of FLAME-DTPA. FLAME-NH_2 was prepared according to procedures described in Chapter 2. FLAME-NH_2 dispersed in dry DMF (1.0 mL) was added slowly to a flask containing 2.0 M DTPA bisanhydride in dry DMF under an argon atmosphere. Anhydrous TEA was added to the mixture, which was then stirred at 40°C for 24 h. The product was separated by centrifugation (14,000 × *g*, 4°C, 30 min) and washed three times with DMF (3.0 mL) and methanol (3.0 mL). FLAME-DTPA nanoparticles were finally dispersed in methanol.

Preparation of F-Gd. FLAME-DTPA nanoparticles were added slowly to an Eppendorf tube containing 1, 10, and 100 mM $GdCl_3·6H_2O$ in methanol (1.0 mL). The mixture was shaken at 50°C for 24 h. The product was separated by centrifugation (14,000 × *g*, 4°C, 30 min) and washed three times with methanol (1.0 mL) and water (1.0 mL). F-Gd nanoparticles were finally dispersed in H_2O.

Synthesis of DO3A. A solution of tert-butyl bromoacetate (6.79 g, 34.82 mmol, 5.14 mL) in CH_3CN (10 mL) was added drop-wise to a suspension of cyclen (2.00 g, 11.62mmol) and sodium acetate (2.85 g, 34.8 mmol) in CH_3CN (25 mL) at 0ºC. The reaction mixture was stirred at room temperature for 24 h, after which it was poured into water (125 mL) to give a clear yellow solution. Solid $NaHCO_3$ was added portionwise until DO3A precipitated as a white solid. The precipitate was collected by filtration and dissolved in $CHCl_3$ (150 mL). The solution was washed with water (75 mL), dried with $MgSO_4$, filtered, and concentrated to approximately 20 mL. Ether (150mL) was added, after which DO3A crystallized as a white fluffy solid (9.1 mmol, y. 78%). ^{1}H NMR (400 MHz, $CDCl_3$) δ 1.38 (27H, s), 2.78–2.88 (12H, m), 3.01 (4H, m), 3.21 (2H, br s), 3.30 (4H, br s), 10.18 (1H, br s); MS (ESI$^+$) *m/z* 515.34 (Calcd for $[M+H]^+$: 515.38)

Synthesis of DO3A-CSPh$_3$. 1-Bromo-3-tritylthiopropane (1.9 g, 4.7 mmol, 1.2 eq) and K_2CO_3 (4.3 g, 31.1 mmol) were added to a solution of DO3A (2.0 g, 3.9 mmol) in dry CH_3CN (40 mL) and the mixture was heated at 60ºC. After 4 h, the reaction mixture was filtered and the filtrate evaporated to dryness under reduced pressure. The residue was dissolved in DCM (100 mL) and the resulting solution was washed with 1M HCl (50 mL) twice, followed by saturated aqueous $NaHCO_3$ (50 mL) and brine. The organic layer was dried ($MgSO_4$), filtered, and concentrated in vacuo. The residue was subjected to flash chromatography on a silica gel, with elution in DCM/MeOH (25:1) to give DO3A-CSPh$_3$ (2.8 g, 3.4 mmol, 86%) as a white foam. ^{1}H NMR ($CDCl_3$, 400 MHz) δ 1.42–1.47 (m, 27H, -^{t}Bu) 1.8–3.1 (m, 28H, -CH_2-) 7.19 (m, 3H) 7.23–7.29 (m, 6H) 7.36–7.41 (m, 6H); MS (ESI$^+$) *m/z* 831.50 (calculated for $[M+H]^+$: 831.51); ^{13}C NMR ($CDCl_3$, 100 MHz) δ 28.0, 28.1, 47.9, 50.1, 51.6, 52.3, 52.8, 55.1, 56.8. 77.2, 81.8, 126.9, 128.1, 129.5, 144.6, 169.9

Synthesis of DOTA-SH. TFA (20 mL) was added dropwise to a mixture of DO3A-CSPh$_3$ (2.0 g, 2.4 mmol), triethylsilane (0.30 g, 2.6 mmol, 415 μL), and butanethiol (20 mL). The mixture was stirred overnight at room temperature. Volatiles were removed in vacuo, a minimum amount of MeOH was added to a solution, and ether (30 mL) was added. The precipitated white solid was collected by filtration and purified by flash chromatography on a silica gel, with elution in $CHCl_3$/MeOH (5:3) to give DOTA-SH as a waxy solid (0.83 g, 1.97 mmol, 82%). ^{1}H NMR ($CDCl_3$, 400 MHz) δ 2.98–3.94 (m, 28H, -CH_2-); MS (ESI$^+$) *m/z* 421.00 (calculated for $[M+H]^+$: 421.21); ^{13}C NMR ($CDCl_3$, 100 MHz) δ 24.0, 28.2, 53.2, 56.0, 58.5, 60.2, 62.2, 170.0

Synthesis of Gd-DOTA-SH. $GdCl_3 \cdot 6H_2O$ (69.2 mg, 0.207mmol) was added to a solution of DOTA-SH (0.83 mg, 0.207 mmol) in MeOH (10 mL), and the mixture was stirred at 50 ºC for 24 h. The solution was purified by Chelex®100 (cation exchange resin) to remove any unreacted gadolinium ion. MS (ESI$^+$) *m/z* 576.12 (calculated for $[M+H]^+$: 576.11)

Synthesis of TMOS-Npys. A solution of (3-mercaptopropyl)-trimethoxysilane (1.0 g, 5.1 mmol) in dry CH_2Cl_2 (5.0 mL) was added dropwise at room temperature over a period of 2 h to a solution of 2,2-dithiodipyridine (3.4 g, 15 mmol) in CH_2Cl_2 (20 mL). The initially colorless solution turned yellow immediately after the addition of (3-mercaptopropyl)-trimethoxysilane because of the production of pyridine-2-thione. After the complete addition of (3-mercaptopropyl)-trimethoxysilane, the solution was stirred an additional 2 h, and the solvent was removed in vacuo. The unsymmetrical disulfide was then extracted with dry diethyl ether and dried under vacuum to give TMOS-Npys as clear liquid (1.5 g, 4.8 mmol, y. 95%). ^{1}H NMR (400 MHz, $CDCl_3$) δ 0.71 (m, 2H), 1.77 (quintet, 2H), 2.8 (t, 2H), 3.48 ppm (s, 3H), 7.06–8.42 ppm (m, 5H of the pyridyl group); ^{13}C NMR (100 MHz, $CDCl_3$) δ 8.8, 22.9, 42.1, 50.8, 61.1, 119.7, 120.9, 137.4, 149.9.

Preparation of FLAME-Npys. The FLAME nanoparticles were dispersed in MeOH (20 mL) under argon atmosphere. After the nanoparticles were sonicated for 30 min to be well-dispersed, the mixture was heated to 40°C. Then, 2.4, 34, and 244 mg of TMOS-Npys was added to the mixture for FSG1, FSG2 and FSG3, respectively. After the solutions were stirred for 24 h, the products were separated by centrifugation (14,000 × *g*, 30 min), washed three times with methanol (15 mL), and finally dispersed in MeOH (10 mL).

Preparations of FSG1, FSG2, and FSG3. The obtained FLAME-Npys nanoparticles were dispersed in MeOH (1 mL), and sonicated for 30 min for dispersion. Then, 1.10, 11.0, and 111 mg of Gd-DOTA-SH was added to the mixture for FSG1, FSG2, and FSG3, respectively. After the mixtures were shaken at 40ºC for 24 h, the products were separated by centrifugation (14,000 × *g*, 30 min), washed three times with methanol (15 mL), and finally dispersed in DMSO (0.5 mL).

^{19}F NMR relaxation time measurement. Nanoparticles were prepared in water containing 5% D_2O. The T_2 was measured by employing the spin-echo method.

MRI measurement. The RARE method was used for ^{1}H and ^{19}F MRI. For ^{1}H MRI, the matrix size was 128 × 128, the slice thickness was 2 mm, and the RARE factor was 8. T_{R} and $T_{\mathrm{E},eff}$ were 1,000 ms and 31.4 ms, respectively. The number of averages was 1. For ^{19}F MRI, the matrix size was 64 × 64, the slice thickness was 30 mm, and the RARE factor was 16. T_{R} and $T_{\mathrm{E,eff}}$ are described in the figure legends. The number of averages was 512.

DLS measurements. The particle size, size distribution, and ζ-potential of the obtained nanoparticles were measured at 25°C with a 580 nm laser at a scattering angle of 90° for DLS size measurements and 173° for ζ-potential measurements. For the DLS size measurements, FLAME nanoparticles were suspended in water or ethanol. Suspensions of each material were prepared in H_2O for ζ-potential measurements.

References

1. Neubauer, A. M.; Myerson, J.; Caruthers, S. D.; Hockett, F. D.; Winter, P. M.; Chen, J.; Gaffney, P. J.; Robertson, J. D.; Lanza, G. M.; Wickline, S. A. *Magn. Reson. Med.* **2008**, *60*, 1066–1072.
2. Luo, K.; Liu, G.; She, W.; Wang, Q.; Wang, G.; He, B.; Ai, H.; Gong, Q.; Song, B.; Gu, Z. *Biomaterials* **2011**, *32*, 7951–7960.
3. Mizukami, S.; Takikawa, R.; Sugihara, F.; Hori, Y.; Tochio, H.; Wälchli, M.; Shirakawa, M.; Kikuchi, K. *J. Am. Chem. Soc.* **2008**, *130*, 794–795.
4. Chalmers, K. H.; Kenwright, A. M.; Parker, D.; Blamire, A. M. *Magn. Reson. Med.* **2011**, *66*, 931–936.
5. Mizukami, S.; Takikawa, R.; Sugihara, F.; Shirakawa, M.; Kikuchi, K. *Angew. Chem. Int. Ed.* **2009**, *48*, 3641–3643.
6. Belorizky, E.; Fries, P. H.; Helm, L.; Kowalewski, J.; Kruk, D.; Sharp, R. R.; Westlund, P.-O. *J. Chem. Phys.* **2008**, *128*, 052315.
7. Nordenskiold, L.; Laaksonen, A.; Kowalewski, J. *J. Am. Chem. Soc.* **1982**, *104*, 379–382.
8. Solomon, I. *Phys. Rev.* **1955**, *99*, 559–595.
9. Crull, G. B.; Kennington, J. W.; Garber, A. R.; Ellis, P. D.; Dawson, J. H. *J. Biol. Chem.* **1989**, *264*, 2649–2655.
10. Bloembergen, N.; Morgan, L. O. *J. Chem. Phys.* **1961**, *34*, 842–850.
11. Clore, G. M.; Tang, C.; Iwahara, J. *Curr. Opin. Struct. Biol.* **2007**, *17*, 603–616.
12. Iwahara, J.; Clore, G. M. *Nature* **2006**, *440*, 1227–1230.
13. Iwahara, J.; Schwieters, C. D.; Clore, G. M. *J. Am. Chem. Soc.* **2004**, *126*, 5879–

5896.

14. Lauffer, R. B. *Chem. Rev.* **1987**, *87*, 901–927.
15. Townsend, D. M.; Tew, K. D.; Tapiero, H. *Biomed. Pharmacother.* **2003**, *57*, 145–155.
16. Herzenberg, L. A.; De Rosa, S. C.; Dubs, J. G.; Roederer, M.; Anderson, M. T.; Ela, S. W.; Deresinski, S. C. *Proc. Natl. Acad. Sci. U. S. A.* **1997**, *94*, 1967–1972.
17. Shahrokhian, S. *Anal. Chem.* **2001**, *73*, 5972–5978.
18. Seshadri, S.; Beiser, A. N. *Engl. J. Med.* **2002**, *346*, 476–483.
19. Savage, D. G.; Lindenbaum, J.; Stabler, S. P.; Allen, R. H. *Am. J. Med.* **1994**, *96*, 239–246.
20. Klee, G. G. *Clin. Chem.* **2000**, *46*, 1277–1283.
21. Ray, J. G.; Laskin, C. A. *Placenta* **1999**, *20*, 519–529.
22. Hwang, C.; Sinskey, A. J.; Lodish, H. F. *Science* **1992**, *257*, 1496–1502.
23. Cannon, M. B.; Remington, S. *J. Protein Sci.* **2006**, *15*, 45–57.
24. Li, H.-Y.; Zheng, X.-M.; Che, M.-X.; Hu, H.-Y. *PLoS One* **2012**, *7*, e35628.
25. Raghunand, N.; Jagadish, B.; Trouard, T. P.; Galons, J.-P.; Gillies, R. J.; Mash, E. A. *Magn. Reson. Med.* **2006**, *55*, 1272–1280.
26. Peng, H.; Chen, W.; Cheng, Y.; Hakuna, L.; Strongin, R.; Wang, B. *Sensors* **2012**, *12*, 15907–15946.
27. Chen, X.; Zhou, Y.; Peng, X.; Yoon, J. *Chem. Soc. Rev.* **2010**, *39*, 2120–2135.
28. Araki, Y.; Sako, A. *J. Chromatogr.* **1987**, *422*, 43–52.
29. Piggott, A. M.; Karuso, P. *Anal. Chem.* **2007**, *79*, 8769–8773.
30. Yuan, L.; Lin, W.; Zhao, S.; Gao, W.; Chen, B.; He, L.; Zhu, S. *J. Am. Chem. Soc.* **2012**, *134*, 13510–135123.
31. Getz, E. B.; Xiao, M.; Chakrabarty, T.; Cooke, R.; Selvin, P. R. *Anal. Biochem.* **1999**, *273*, 73–80.
32. Cline, D. J.; Redding, S. E.; Brohawn, S. G.; Psathas, J. N.; Schneider, J. P.; Thorpe, C. *Biochemistry* **2004**, *43*, 15195–15203.
33. Demer, J. L.; Dushyanth, A. J. *AAPOS* **2011**, *15*, 17–23.
34. Lutterbey, G.; Wattjes, M. P.; Kandyba, J.; Harzheim, M.; Falkenhausen, M. V; Morakkabati, N.; Schild, H.; Gieseke, J. *Br. J. Radiol.* **2007**, *80*, 668–673.
35. Tien, R. D.; Felsberg, G. J.; MacFall, J. Neuroradiology 1992, 35, 38–41.
36. Werpy, N. M.; Ho, C. P.; Garcia, E. B.; Kawcak, C. E. *Vet. Radiol. Ultrasound* **2013**, *54*, 31–35.
37. Lillig, C. H.; Berndt, C. *Biochim. Biophys. Acta* **2013**, *1830*, 3137–3138.
38. Lu, S. C. *Biochim. Biophys. Acta* **2013**, *1830*, 3143–3153.

39. Bachhawat, A. K.; Thakur, A.; Kaur, J.; Zulkifli, M. *Biochim. Biophys. Acta* **2013**, *1830*, 3154–3164.
40. Wu, G.; Fang, Y.; Yang, S.; Lupton, J. R.; Turner, N. D. *J. Nutr.* **2004**, *134*, 489–492.

Chapter 4 ^{19}F MRI traceable anti-cancer drug carrier, mFLAME, for theragnostics

Introduction

Nanostructured biomaterials have been investigated for their potential applications in biomedical imaging, diagnosis, and therapy.[1–7] In view of these applications, multifunctional nanoparticles have been reported, including micelles,[8,9] liposomes,[10–13] polymers,[14,15] and dendrimers.[16–20] Among these various nanomaterials, MSNs have been examined with the aim of providing multifunctional platforms for fluorescence,[21–24] magnetism,[25–28] and therapeutic functions.[29–31] MSNs have attractive properties such as extremely large surface areas (1000 $m^2 g^{-1}$), well-defined and tunable pore sizes (1.5–10 nm), and ease of functionalization by various synthetic approaches.[32–38] Among functional MSNs, magnetite nanoparticle-doped MSNs were reported as ^{1}H MRI-traceable drug carriers.[22,25–27] ^{1}H MRI is a non-invasive in vivo molecular imaging technique used in both clinical and research fields. It not only provides high-resolution anatomical images of biological tissues, but also enables the assessment of disease pathogenesis with contrast agents.[39,40] However, ^{1}H MRI is not ideal for the tracking of a particular signal with contrast agents owing to the background signal in living bodies.

To overcome this intrinsic limitation of ^{1}H MRI, the author focused on ^{19}F MRI, which has a relatively high sensitivity (83% of ^{1}H) and no detectable background signal. Many smart ^{19}F MRI probes for monitoring biological phenomena have been reported that make use of these advantages.[41–43] However, the biggest limitations of ^{19}F MRI in practical applications are the low MRI signals, which require high probe concentrations, and the long accumulation time, which results in low spatial resolution.[44] The author developed a highly sensitive ^{19}F MRI contrast agent, which comprises a PFCE core and

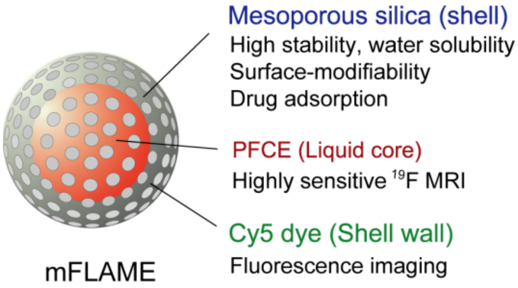

Figure 1. The components of mFLAME.

a silica shell.[45] The design strategy of the nanoparticle is based on the increase of uniform fluorine whose mobility is retained in the liquid phase core. The author showed that the ^{19}F MRI contrast agent was useful for the detection of gene expression in live cells and in vivo tumor imaging. By using this core-shell structure-based design strategy, the author developed a novel biomaterial named mFLAME, with a PFCE core and mesoporous silica shell for ^{19}F MRI- and fluorescence-traceable drug release (Figure 1).

4-1 Design, preparation, and characterization of ^{19}F MRI- and fluorescence-traceable drug delivery carrier.

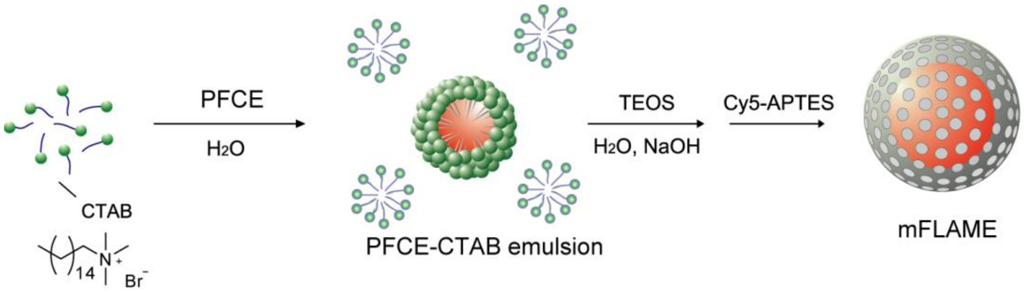

Scheme 1. Synthetic scheme of mFLAME.

The procedure for the fabrication of mFLAME is illustrated in Scheme 1. PFCE was chosen as a highly sensitive ^{19}F MRI marker owing to its twenty magnetically identical fluorine atoms. Generally, PFCE requires surfactants for biological applications because of its extremely low water solubility.[42,46–48] The author discovered that CTAB, which is commonly used for the synthesis of MSNs,[49] was capable of dispersing PFCE in water. Furthermore, the core-shell type nanoparticles that constitute a PFCE core and the mesoporous silica shell were produced from the PFCE emulsions by a sol-gel process. To impart fluorescence imaging capability, Cy5 dye was covalently modified with a mesoporous silica shell by silica polymerization in the presence of Cy5-conjugated APTES.

The characterization of the nanomaterials was performed by DLS (Figure 2a, b). The ζ-potential and hydrodynamic diameter of PFCE emulsion were +51.0 mV and 78 nm, respectively. In contrast, those of mFLAME were -21.1 mV and 165 nm, respectively. The DLS data showed that mFLAME did not form aggregates in the aqueous solution. The increase in size and the decrease in ζ-potential were due to the formation of the silica shell. The N_2 adsorption/desorption isotherms of mFLAME showed a typical mesoporous structure[50] with a BET surface area of 715 $m^2\ g^{-1}$, pore volume of 1.21 $cm^3\ g^{-1}$, and pore width of 6.7 nm (Figure 2c). The core-shell structures of the nanoparticles were clearly observed by TEM (Figure 2d). The average diameter of the particles was

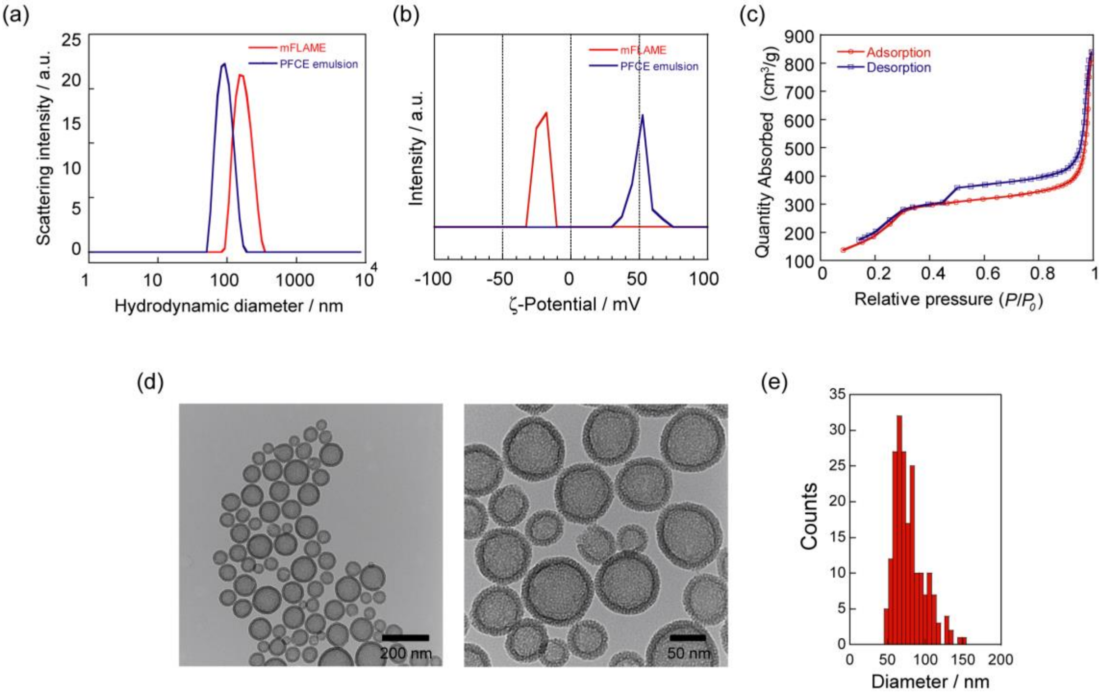

Figure 2. Characterization of FLAME. (a) Hydrodynamic diameter of the PFCE emulsion and mFLAME by DLS. (b) ξ-potential graphs of the PFCE emulsion and mFLAME. (c) N_2 adsorption/desorption isotherms of mFLAME. (d) TEM image of mFLAME. (e) Particle size distribution histogram calculated from TEM images (n = 200).

79 ± 20 nm, which was calculated from the TEM image.

Inclusion of PFCE in the particle was confirmed by NMR spectroscopy. The mFLAME was dispersed in PBS solution and ^{19}F NMR showed a PFCE-derived single peak at -16.4 ppm (Figure 3a). The transverse relaxation, T_2, of FLAME was 0.211 s, which was almost the same as that of PFCE emulsion (T_2 = 0.242 s). The result suggests that the silica coating did not affect the ^{19}F MRI sensitivity of PFCE. ^{19}F MRI measurements using capillary phantoms showed that strong ^{19}F MRI signals were observed from phantoms, including mFLAME, and the ^{19}F MRI contrast intensity was proportional to the PFCE concentration (Figure 3b). Then, in vivo MRI was performed after the injection of carboxylated mFLAME (mFLAME-COOH) (Scheme S1) into a living mouse (Figure 3c). Strong ^{19}F MRI signals of mFLAME were detected from the liver. This result indicates that mFLAME had enough sensitivity for in vivo ^{19}F MRI application. Then, the optical property was analyzed and mFLAME showed the typical fluorescence emission of Cy5 (Figure 3d).

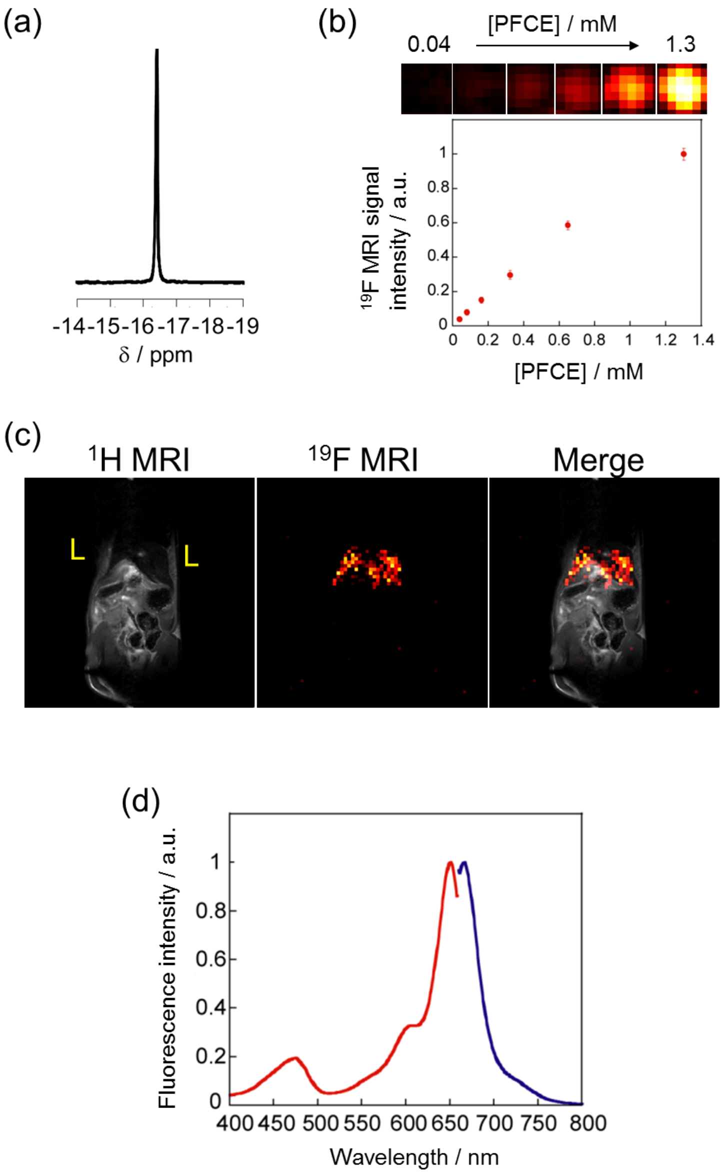

Figure 3. (a) ^{19}F NMR spectra of mFLAME. (b) (top) ^{19}F MRI of phantoms filled with mFLAME in PBS (500 µL). (right) Plot of normalized ^{19}F MRI signal intensity versus PFCE. (c) In vivo ^{1}H/^{19}F MRI of mFLAME-COOH in mouse. The positions of the liver are represented as L. (d) Excitation and emission spectra of mFLAME.

4-2 Specific Cellular Uptake of Folate-functionalized mFLAME.

To demonstrate the efficient delivery of mFLAMEs for cancer therapy, the author focused on the folate receptor, which is a 38-kDa glycophosphatidylinositol-linked membrane protein and is overexpressed on the surface of most solid tumors, including colorectal carcinoma.[51–53] Recently, it was reported that the folate receptor-mediated uptake was exploited to facilitate the entry of nanomaterials into the cells.[51,54–56] Hence, a folate-functionalized mFLAME nanoparticle (mFLAME-FA, Figure 4) was synthesized as shown in Scheme 2.

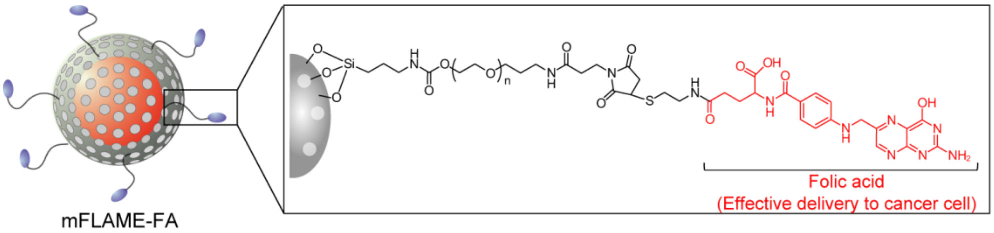

Figure 4. The chemical structure of mFLAME-FA

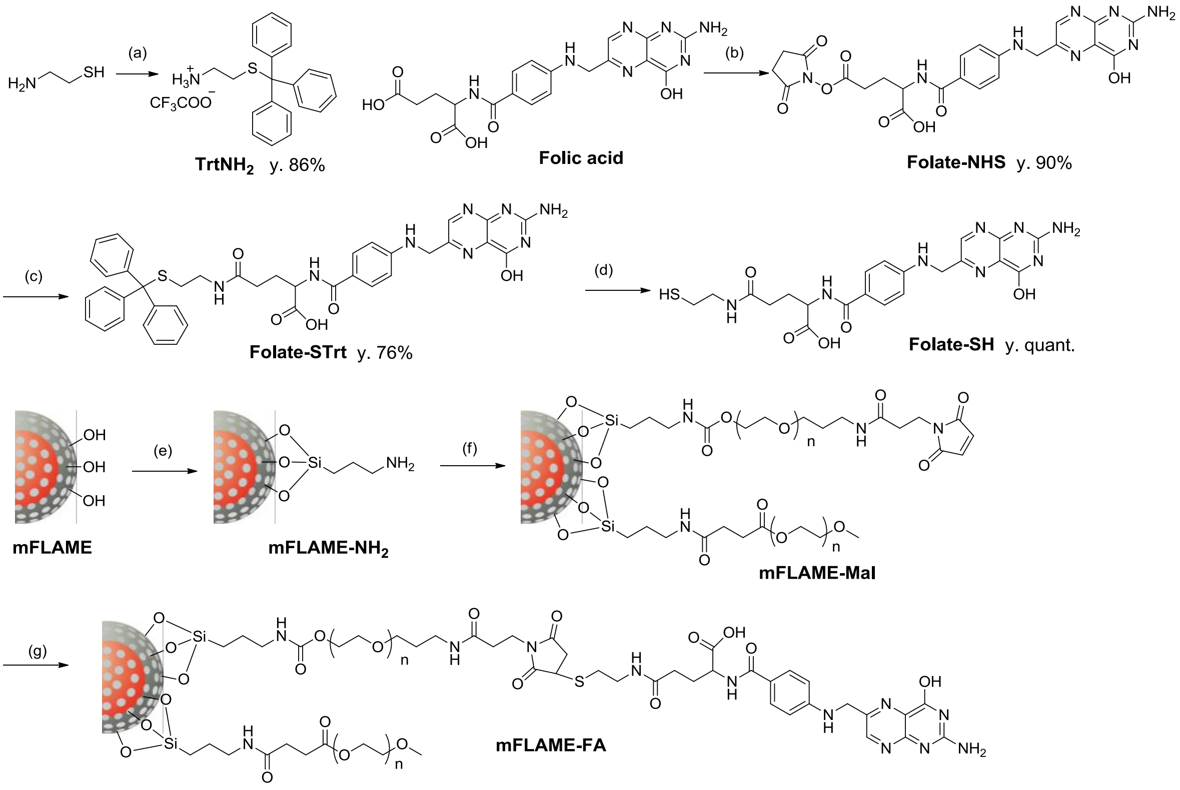

Scheme 2. Synthetic route to mFLAME-FA. (a) TFA; (b) *N*-hydroxysuccinimide, WSCD・HCl, HOBt, TEA, DMSO; (c) TrtNH$_2$, DMSO; (d) TFA, triisopropylsilane, H_2O; (e) APTES, 2-propanol; (f) MAL-$(CH_2)_2$CONH$(CH_2)_3$-O-PEG-COO-NHS (MW 5,000), methoxy-PEG-$(CH_2)_5$-COO-NHS (MW 5,000), TEA, DMF; (g) Folate-SH, TEA, DMSO.

Table 1. ζ-Potential values and hydrodynamic diameters of mFLAMEs

Materials	Hydrodynamic diameter (nm)	ζ-Potential (mV)
mFLAME	165 ± 8	-21.1 ± 2.5
mFLAME-NH_2	284 ± 23	18.4 ± 5.6
mFLAME-Mal	134 ± 3	-40.1 ± 3.1
mFLAME-FA	142 ± 3	-45.1 ± 2.3

The ζ-potential value of mFLAME-FA was -51 mV in contrast to +14.1 mV for the amino-functionalized mFLAME-NH_2. A PEGylated mFLAME (mFLAME-PEG) was also prepared for the control experiment (Scheme S1). The ultraviolet (UV) spectra of mFLAME-PEG and mFLAME-FA show that only mFLAME-FA had the characteristic absorption peaks of folate (280 and 362 nm), which confirmed the folate modification (Figure 5a). The mean diameters of mFLAME-FA in water at 0, 1, 3, 5, and 7 days after the synthesis were determined by DLS analysis, and almost no change in particle size was observed for 7 days. This result suggests that the mFLAME-FA possesses satisfactory stability in aqueous solutions (Figure 5b). Next, the cytotoxicity of the mFLAME nanoparticles to KB cells was evaluated by MTT assay, which indicated that the cell viability was not affected by up to 0.32 mg mL^{-1} of PFCE (Figure 5c). This result suggests that the mFLAMEs are biocompatible and safe for in vivo applications.

FLAMEs.

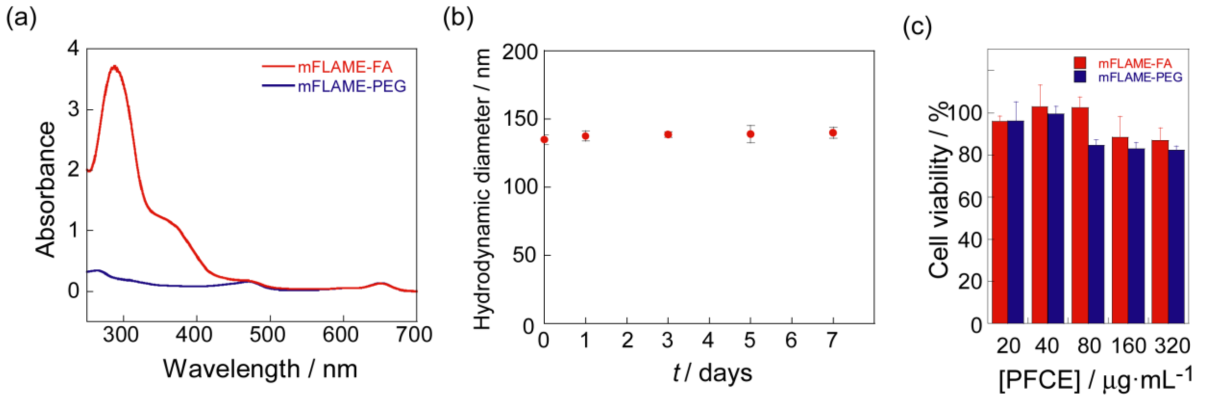

Figure 5. (a) UV-Visible spectra of mFLAME-FA and mFLAME-PEG. (b) DLS analysis of FLAME-FA followed over time at 4°C storage temperature. (c) Cytotoxicity of mFLAME-FA and mFLAME-PEG against cultured KB cells.

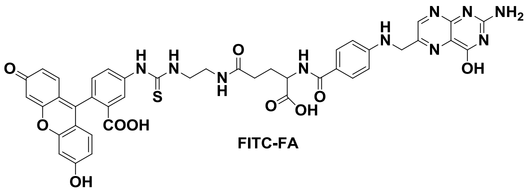

Figure 6. Chemical structure of fluorescent probe FITC-FA for folate-receptor.

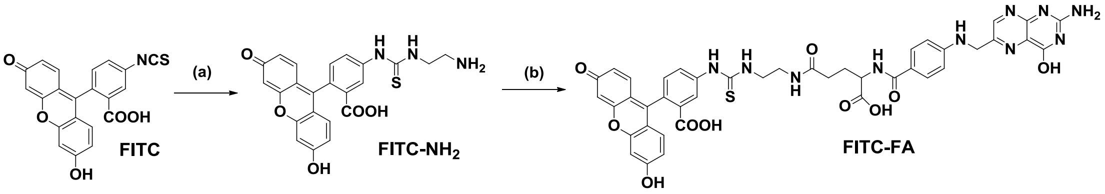

Scheme 3. Synthetic route to FITC-FA. (a) Ethylenediamine, DMF; (b) FA-NHS, DMF, TEA.

To further investigate the potential of the biomedical applications of mFLAMEs, their uptakes into specific cells were compared via fluorescence imaging and ^{19}F MRI. The expression of folate receptors on the cell surface was confirmed by a small-molecule imaging agent, FITC-FA (Figure 6). FITC-FA was synthesized from FITC in 2 steps (Scheme 3). As reported in previous research,[57] KB cells were overexpressed with folate receptors, while there was no folate receptor on A549 cells (Figure 7).

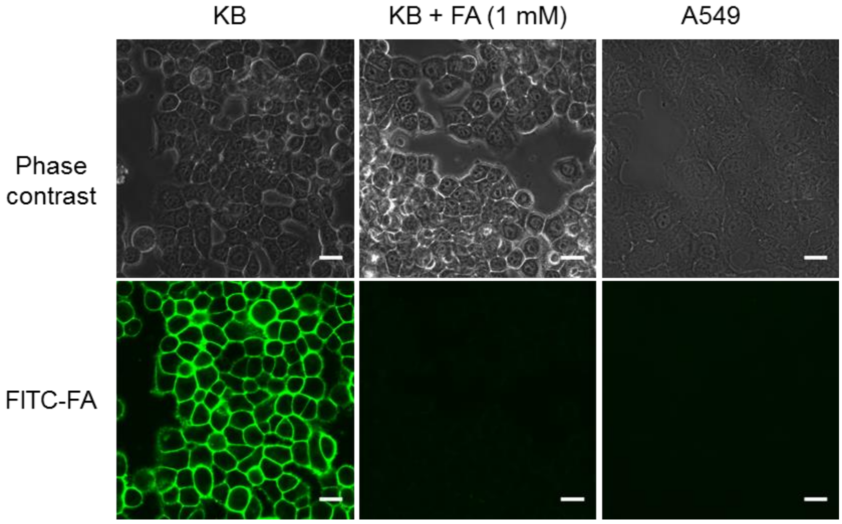

Figure 7. Fluorescence imaging of KB cells and A549 cells treated with FITC-FA (5 μM) for 30 min. Scale bar is 20 μm.

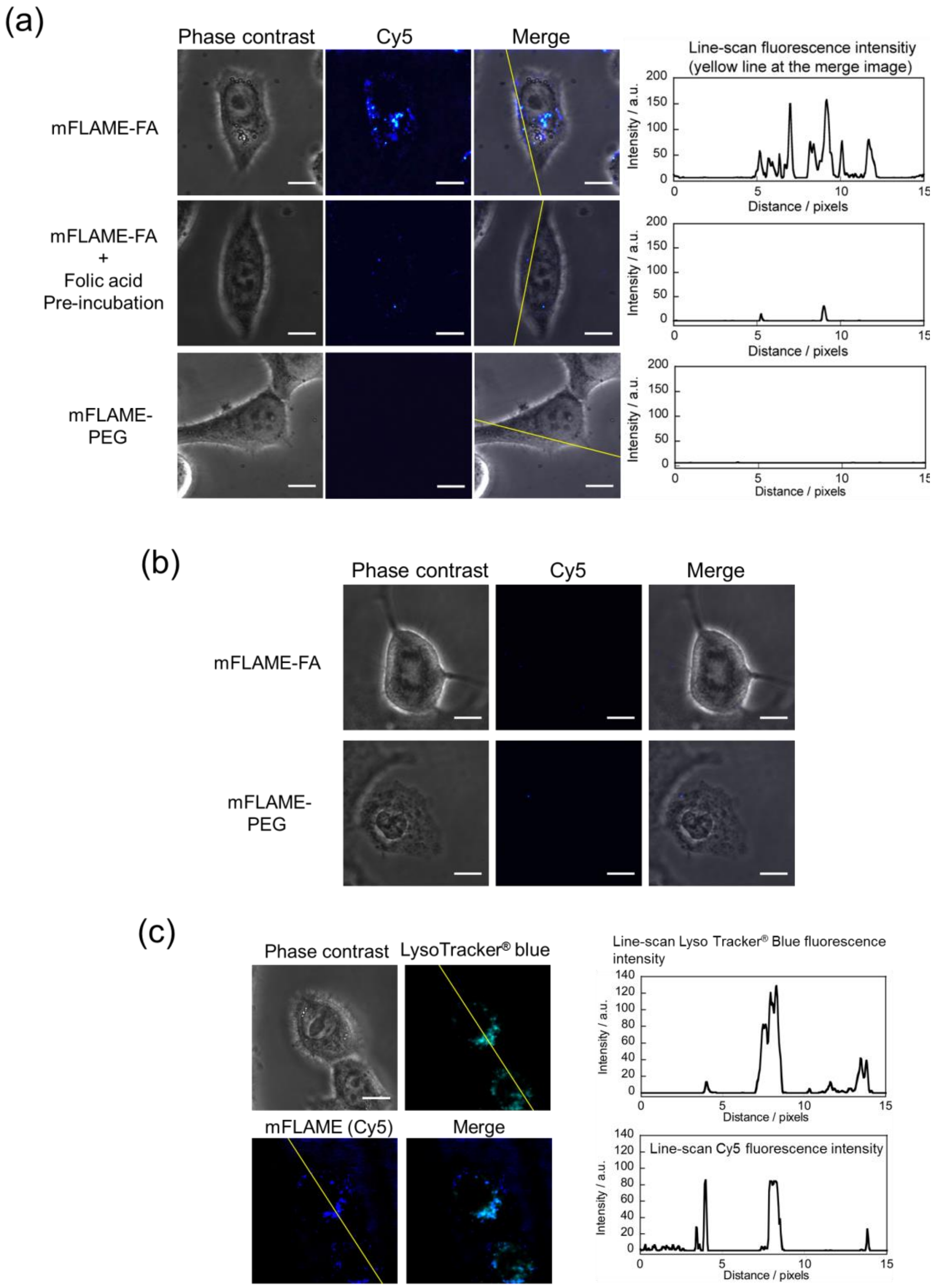

Figure 8. (a) Confocal laser scanning microscopy images of KB cells incubated with mFLAME-FA or mFLAME-PEG with or without folic acid for 4 h. Measurement condition: Cy5 was excited at 635 nm and detected at 660–760 nm. Scale bar: 10 µm. (b) Fluorescence imaging of A549 cells treated with mFLAME nanoparticles. Scale bar is 10 µm. (c) Fluorescence imaging of KB cells treated with mFLAME-FA and LysoTracker® blue. Scale bar is 10 µm.

The Cy5 in the nanoparticles allowed direct visualization of the nanoparticle uptake into cells (Figure 8a). The fluorescence image of KB cells after 4 h of incubation with mFLAME-FA clearly showed a significant uptake of the nanoparticles. The author also demonstrated that the specific uptake was blocked by preincubation for 1 h with free folic acid before the treatment of mFLAME-FA. In contrast, no fluorescence was observed from KB cells treated with mFLAME-PEG. In addition, almost no fluorescence was observed from A549 cells treated with mFLAME-FA or mFLAME-PEG (Figure 8b). These results indicate that the mFLAME-FA uptake was associated with folate receptor binding. The spot-like fluorescence image also indicates that mFLAME-FA was internalized via endocytosis, and almost all nanoparticles remained in endosomes (Figure 8c).

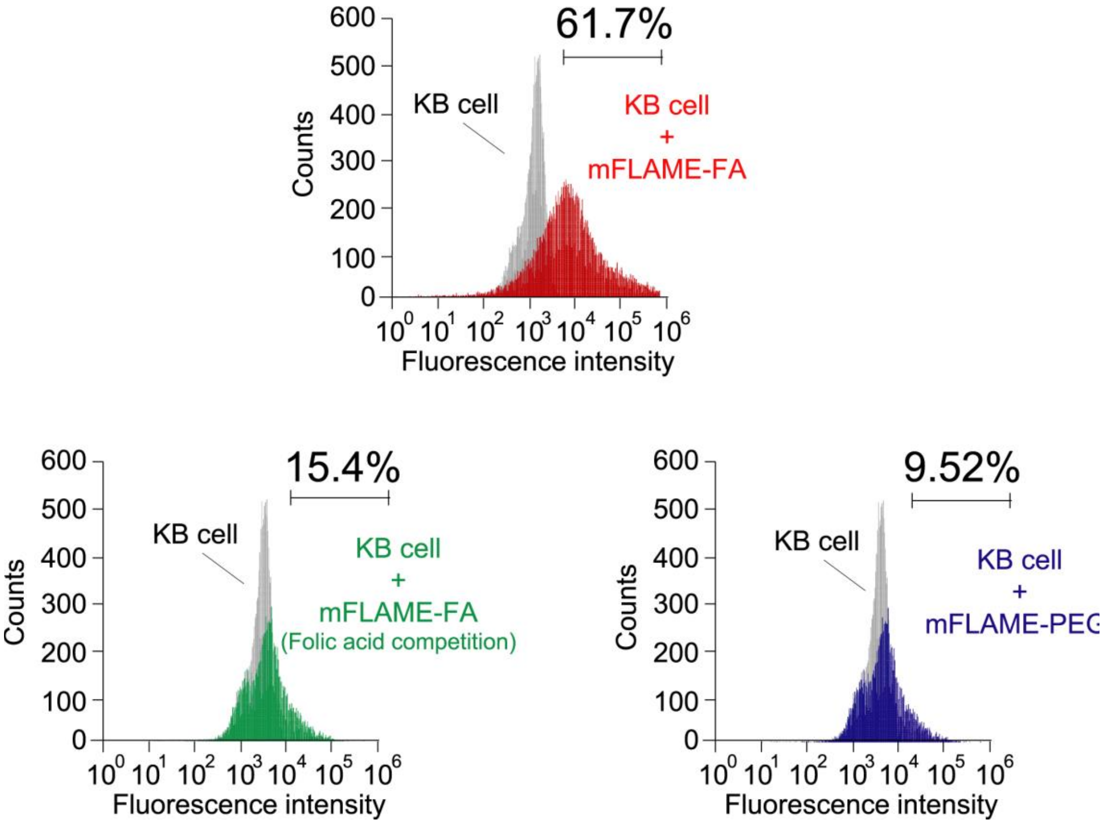

Figure 9. Flow-cytometric analysis of cellular uptake. The gray histograms show the distribution of non-treated cells.

Flow cytometric analysis was also applied to investigate the cellular uptake behaviors of KB cells for mFLAME (Figure 9). The results showed that KB cells took up more mFLAME-FA than mFLAME-PEG (nearly 6.5-fold). By the competitive binding of free folic acid to the folate receptor, endocytosis of mFLAME-FA was decreased by more than 75%.

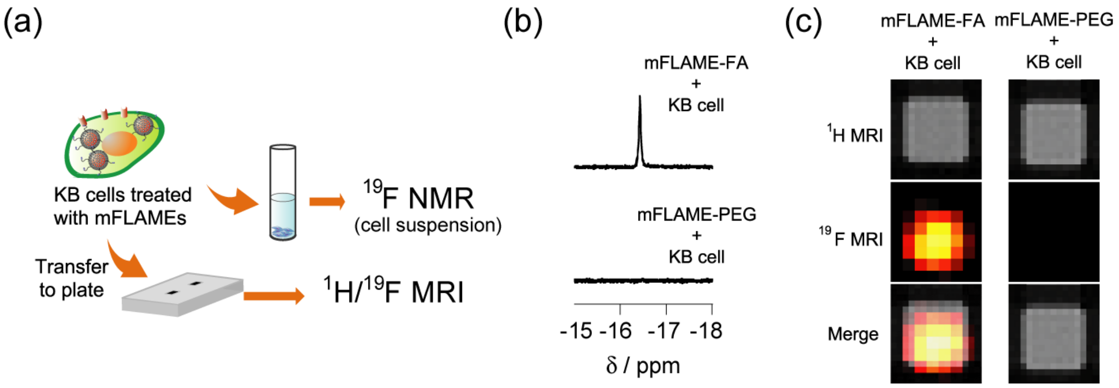

Figure 10. (a) Illustration of the experimental procedure for the MRI detection of mFLAME-FA taken by KB cells. (b) ^{19}F NMR of cell suspension treated with mFLAME-FA or mFLAME-PEG. (c) ^{1}H/^{19}F MR images of KB cells treated with mFLAME-FA or mFLAME-PEG.

The PFCE core of mFLAME-FA allowed direct visualization of the nanoparticle uptake into cells by ^{19}F NMR and MRI. After mFLAME-FA was incubated with KB cells for 4 h and washed with PBS, KB cells were transferred to a well of a microtiter plate and ^{1}H/^{19}F MRI experiments were performed (Figure 10). Figure 10c shows MR images of the microtiter plate, including KB cells treated with mFLAMEs. The strong ^{19}F MRI signals were observed from mFLAME-FA, while no ^{19}F MRI signal was observed from the control sample. These results demonstrate that mFLAME can be used as a multimodal probe for ^{19}F MRI and fluorescence imaging.

4-3 Drug encapsulation and cellular toxicity of drug-loaded mFLAMEs.

To examine the potential of mFLAMEs for drug delivery, a chemotherapeutic agent DOX, which is well-known as an anti-cancer drug,[58–60] was loaded into mFLAMEs. The loading amount of DOX in mFLAME was determined by the difference in the UV

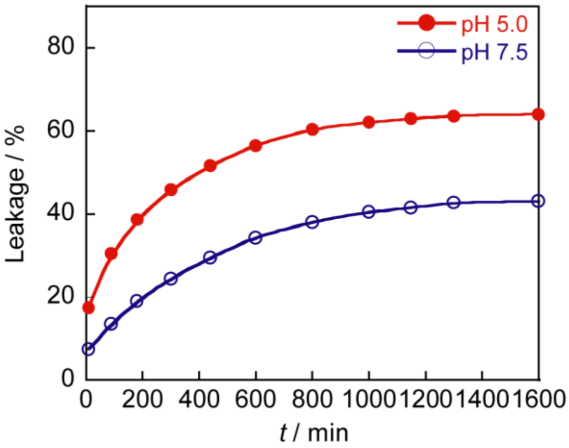

Figure 11. Release profile of DOX loaded mFLAME-FA in citric acid buffer (pH 7.5 and 5.0) at 37°C.

spectra before and after the loading. The author then evaluated the release profiles of the encapsulated DOX at different pH by UV-visible absorption spectroscopy. Encapsulated-DOX was released gradually from mFLAMEs in a time-dependent manner (Figure 11). Interestingly, the release rates from mFLAMEs at pH 5.0 were faster than those at pH 7.5, which suggests that the surrounding pH change affects the electrostatic interaction between mFLAMEs and DOX. These results also indicate that

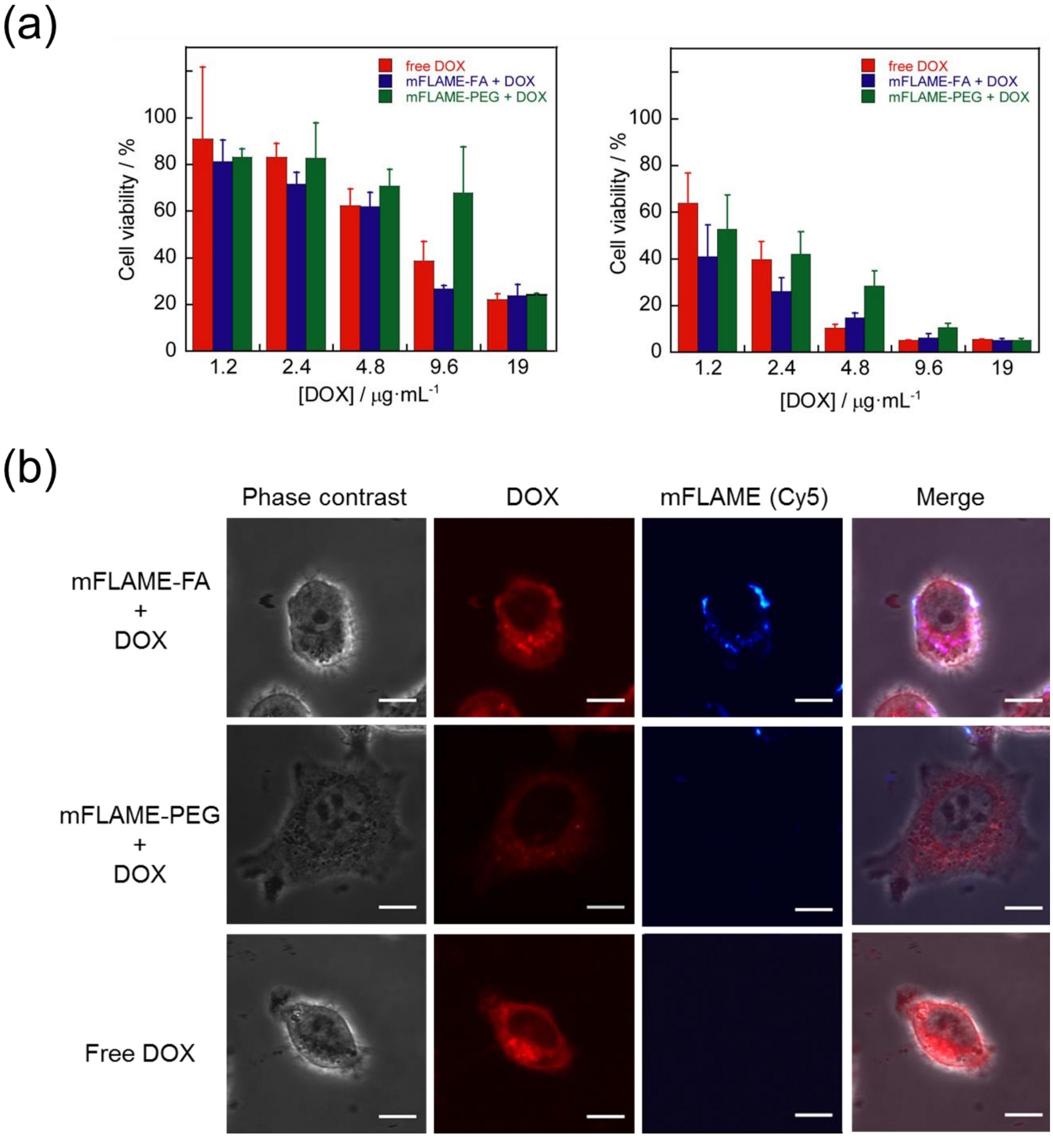

Figure 12. Concentration-dependent cell survival data of folate receptor positive-KB cells treated with free DOX or DOX-loaded mFLAMEs for (left) one day or (right) two days. (b) Fluorescence imaging of KB cells treated with DOX-loaded mFLAME-FA, DOX-loaded mFLAME-PEG and free DOX for 6 h. DOX concentrations were 9.6 μg mL^{-1}. Measurement condition: Cy5 was excited at 635 nm and detected at 660–760 nm. DOX was excited at 559 nm and detected at 570–670 nm. Scale bar: 10 μm.

mFLAME-FA showed efficient drug release ability in the endosome/lysosome (pH 5.0–5.5), which have a lower pH than other cellular components, such as cytosol.[61,62]

Then, the DOX-loaded mFLAMEs were also evaluated by measuring the viability of KB cells (Figure 12a). DOX-loaded mFLAME-FA had a greater cytotoxic effect on KB cells compared with mFLAME-PEG. The cellular uptake of DOX-loaded nanoparticles was analyzed by CLSM (Figure 12b). Similar intensities of fluorescence from DOX were observed from KB cells treated with DOX-loaded mFLAME-FA and cells treated with free DOX. In contrast, the cells treated with DOX-loaded mFLAME-PEG showed weaker fluorescence. These results indicate that the strong cytotoxic effect of DOX-loaded mFLAME-FA on KB cells is due to the efficient cellular internalization and drug release in the cells.

Experimental Sections

General Methods. General chemicals were of the highest grade available, supplied by Tokyo Chemical Industries, NOF Corporation, Wako Pure Chemical, and Aldrich Chemical Co., and used without further purification. Sulfo-Cy5 NHS ester was purchased from Lumiprobe. APTES, CTAB, and TEOS were purchased from Tokyo Chemical Industry. PFCE was supplied by Wako Pure Chemical. MAL-$(CH_2)_2CONH(CH_2)_3$-O-PEG-COO-NHS (PEG is poly(ethylene glycol); molecular weight (MW) 5,000, SUNBRIGHT® MA-050TS) and methoxy-PEG-$(CH_2)_5$-COO-NHS (MW 5,000, SUNBRIGHT® ME-050HS) were purchased from NOF Corp. Folic acid was purchased from Aldrich Chemical Co. They were used without further purification. NMR spectra and T_1 and T_2 relaxation times were measured on a JEOL JNM-AL 400 instrument at 400 MHz for ^{1}H, and at 100.4 MHz for ^{13}C NMR using tetramethylsilane as an internal standard, and at 376 MHz for ^{19}F NMR using sodium trifluoroacetate as an internal standard. Fluorescence spectra were recorded using a Hitachi F4500 spectrometer. The slit width was 5.0 nm for both excitation and emission. The photomultiplier voltage was 700 V. MRIs were recorded on a Bruker Avance II 500WB spectrometer equipped with a wide bore (89 mm), 11.7-T magnet, and a micro-2.5-imaging probe head operating at frequencies of 500 MHz for ^{1}H and 471 MHz for ^{19}F measurements. A volume coil of 25 mm diameter was used. Image acquisition and processing were carried out using the ParaVision software (Bruker BioSpin). TEM images were acquired using the HITACHI H-9000 (300 V). Particle size distribution and ζ-potential were measured by DLS on the particle analyzer nano partica SZ-100 from HORIBA. Fluorescence microscopic images were obtained using the Olympus FV10i-LIV confocal laser scanning microscope equipped with a ×60 lens. The emission filter sets used were Olympus BA490–540 for FITC-FA, and Olympus BA660–760 for mFLAME. All the captured microscopic images were analyzed with ImageJ software. In Figure S5, Fluorescence microscopic images were obtained using the IX71 (Olympus) for the inverted fluorescence microscope, Cool SNAP HQ (Photometrics) for the cooled CCD camera, and a light engine (Lumencor Spectra X®, Olympus) with emission filters (Semrock). The imaging software MetaMolph (Universal Imaging Corporation) was used for data analysis. Flow cytometric analysis was performed by cell analyzer EC 800 (Sony Biotechnology Inc.). The emission filter set used was BP700.

Synthesis of mFLAME. Sulfo-Cy5 NHS ester (2.0 mg) was reacted with APTES (10 μL) in ethanol (0.20 mL) in the dark for one day. CTAB (50 mg) was first dissolved in deionized water (6 mL). PFCE (30 μL) was added to the CTAB solution and the resulting solution was sonicated for 2 h at 50°C. The aqueous CTAB-PFCE solution was filtered through a 0.45-μm syringe filter to remove any large aggregates or contaminants. The aqueous CTAB-PFCE solution was added to a solution of deionized water (23 mL) and 2 M sodium hydroxide (0.15 mL), and heated to 70°C while stirring. Then, TEOS (0.25 mL), the Cy5-APTES solution (40 μL), and ethyl acetate (1.0 mL) were slowly added to the reaction solution and the resulting solution was stirred for 4 h. The synthesized materials were centrifuged (14,000 × *g*, 30 min) and washed with ethanol and H_2O three times and dispersed in 40 mL of isopropanol.

Synthesis of mFLAME-NH_2. The mFLAME dispersed in isopropanol (40 mL) was heated to 80 °C while stirring. Then, APTES (200 μL) was slowly added into the resulting solution and stirred for 4 h under Ar. The resulting materials were washed with ethanol three times. The CTAB surfactants were removed from the mesoporous silica nanoparticles by dispersing the mFLAME-NH_2 in a solution of ammonium nitrate (160 mg) and 95% ethanol (60 mL) and heating the mixture at 60°C for 1 h. The resulting materials were centrifuged (14,000 × *g*, 30 min) and washed with ethanol three times. mFLAME-NH_2 was dispersed in 20 mL of DMF.

Synthesis of mFLAME-Mal. The mFLAME-NH_2 dispersed in dried DMF (10 mL) was heated to 40°C while stirring. Then, MAL-$(CH_2)_2CONH(CH_2)_3$-O-PEG-COO-NHS (0.40 g) and dried TEA (50 μL) were added to the resulting solution and stirred for 2 days under Ar atmosphere. The resulting materials were washed with DMF three times (14,000 × *g*, 30 min). mFLAME-Mal was dispersed in 10 mL of DMSO.

Synthesis of mFLAME-FA. The synthesis method of thiol-functionalized folic acid (FA-SH) has been reported.[15] mFLAME-Mal dispersed in dimethyl sulfoxide (10 mL) was heated to 40°C while stirring. Then, FA-SH (50 mg) and dried triethylamine (50 µL) were added into the resulting solution and stirred for 2 days under Ar atmosphere. The resulting materials were washed with DMSO and H_2O three times (14,000 × *g*, 30 min). mFLAME-FA was dispersed in 5 mL of H_2O.

Synthesis of FITC-NH$_2$. Ethylenediamine (600 µL, 9.0 mmol) was dissolved in 3.0 mL of DMF. Then, FITC (150 mg, 0.39 mmol) dissolved in DMF was added dropwise to the solution. The mixture was stirred for 12 h at RT and evaporated under reduced pressure. The residue was washed three times with diethyl ether to produce FITC-NH$_2$ (y. 84%). ^{1}H NMR (400 MHz, DMSO-d_6) δ 2.75 (t, 2H), 2.88 (s, 1H), 3.05 (dd, 2H), 3.15 (s, 1H), 6.45–6.49 (m, 4H), 6.63–6.65 (m, 2H), 7.08 (d, 1H), 7.99 (s, 1H), 8.16 (s, 1H); MS (ESI$^+$) *m/z*: 450.07 (calculated for $[M+H]^+$): 450.11.

Synthesis of FITC-FA. The synthesis method of FA-NHS has been reported.[15] FITC-NH$_2$ (18 mg, 0.040 mmol) and FA-NHS (108 mg, 0.20 mmol) were dissolved in 6.0 mL of DMF. TEA (29 µL, 0.20 mmol) was added to the solution. The mixture was stirred at RT for 12 h. After the reaction solution was evaporated, the product was purified by RP-HPLC and eluted with H_2O/acetonitrile containing 0.1% formic acid to yield FITC-FA (y. 18%). ^{1}H NMR (DMSO-d_6, 400 MHz) δ 2.23 (t, 2H), 2.33 (s, 1H), 2.67 (s, 1H), 3.12 (m, 2H), 3.39 (s, 2H) 3.50 (s, 1H), 4.47 (d, 2H), 5.73 (s, 1H), 6.54–6.86 (m, 8H), 6.90–7.00 (m, 2H), 7.20 (d, 1H), 7.63 (d, 2H), 8.01–8.10 (m, 2H), 8.21 (s, 1H); HRMS (FAB$^-$) *m/z*: 871.2264 (calculated for $[M+H]^+$): 871.2324.

MRI measurements. RARE method was used for ^{1}H and ^{19}F MRI. For the ^{1}H MRI, the matrix size was 128 × 128, slice thickness was 2 mm, and the RARE factor was 8. T_R and $T_{E,eff}$ were 1,000 ms and 31.4 ms, respectively. The number average was 1. For the ^{19}F MRI, the matrix size was 64 × 64, slice thickness was 30 mm, and the RARE factor was 16. T_R and $T_{E,eff}$ were 1,000 ms and 80 ms, respectively. The number average was 512.

^{19}F NMR relaxation time measurements. Nanoparticles were prepared in water containing 5% D_2O. The transverse relaxation time T_2 was measured by the spin-echo method.

DLS Measurements. The particle size, the size distribution, and the ζ-potential of the obtained nanoparticles were measured at 25°C with a 580 nm laser at a scattering angle of 90° for the DLS size measurement, and 173° for the ζ-potential measurement. For the DLS size measurement, mFLAME nanoparticles were suspended in water or ethanol. Suspensions of each material in water were prepared for the ζ-potential measurements.

Fluorescence imaging of cells treated with mFLAMEs. KB cells (folate receptor-positive cells) and A549 cells (folate receptor-negative cells) were seeded into glass-bottom dishes, and then cultured at 5% CO_2 for 24 h. For free folate competition studies, 1 mM folic acid was added into the medium and then incubated at 5% CO_2 for 1 h. The cells were washed once with Hank's balanced salt solution (HBSS), and incubated with mFLAMEs or DOX-loaded mFLAMEs (C_{PFCE} = 0.26 mM) for 4 h or 6 h, respectively. In Figure 8c, Lysotracker® blue (10 μM, Invitrogen) was used within 1 h of the treatment of the nanoparticles. After a triple HBSS rinse, the fluorescence images were acquired by CLSM.

Cellular uptake evaluated by flow cytometer. KB cells were seeded into a 24-well plate and then cultured at 5% CO_2 for 24 h. For folate competition studies, 1 mM folic acid was added to the incubation medium and then incubated at 5% CO_2 for 1 h. The cells were washed once with PBS and incubated with mFLAMEs for 4 h. After a triple PBS rinse, the cells were harvested with trypsin-EDTA and washed with PBS. The cells were then resuspended in PBS and analyzed by a flow cytometer.

^{19}F MRI detection of cellular uptake. KB cells were seeded into a 24-well plate and then cultured at 5% CO_2 for 24 h. The cells were washed once with PBS and incubated with mFLAMEs (C_{PFCE} = 0.52 mM) for 4 h. After a triple PBS rinse, the cells were harvested with trypsin-EDTA and washed with PBS. The cells (1.0×10^5 cells) were resuspended in PBS and transferred to a customized 384-well plate for MRI measurement, and then ^{1}H/^{19}F MRI was performed.

Cell cytotoxicity assessment of mFLAMEs. The cell cytotoxicity of mFLAMEs in vitro was evaluated by the typical MTT reduction assays. KB cells were seeded into a 96-well plate at 5,000 cells well^{-1} and cultured in 5% CO_2 for 24 h. mFLAMEs (1.5 mg) were suspended in DOX solution and stirred for 24 h. The DOX-loaded mFLAMEs were separated by centrifugation (14,000 × *g*, 30 min) and washed with H_2O. DOX-loaded FLAMEs were dispersed in the culture media (folic acid-free RPMI1640) with different concentrations of DOX (1.2, 2.4, 4.8, 9.6, and 19 μg·mL^{-1}) and then added into the wells. After co-incubation for 24 or 48 h at 37°C in 5% CO_2, the culture media were removed and 100 μL aliquots of MTT solution were added. After co-incubation for 4 h, the culture media were replaced with DMSO (100 μL $well^{-1}$) and the absorbance at 590 nm was measured by a microplate reader. The cell cytotoxicity was finally expressed as the percentage of cell viability relative to the untreated control cells.

In vivo experimental procedure for MRI. Female mice (Balb/cA, 20 to 25 g bodyweight) were administered mFLAME-COOH (0.20 mL, C_{PFCE} = 2.6 mM) through tail vein injection. For MRI measurements, mice were anesthetized using 2.0% isoflurane at a flow rate of 0.2 L min^{-1} and scanned.

Fluorescence imaging of folate receptors with FITC-FA. KB cells and A549 cells were seeded into glass-bottom dishes and then cultured at 5% CO_2 for 24 h. The cells were washed once with HBSS and treated with FITC-FA (5 μM) for 30 min. After a triple HBSS rinse, the fluorescence images were acquired by CLSM.

Drug release studies. DOX-loaded mFLAMEs were prepared in the same way as for cell cytotoxicity assessment. DOX-loaded mFLAMEs were dispersed in citric acid buffer (pH 7.5 and 5.0). At a certain time, an aliquot was separated by centrifugation (14,000 × *g*, 30 min) to remove the nanoparticles. The release of the DOX from the pores to the aliquot solution was monitored via the absorbance of the DOX at 480 nm. The total release amount of DOX was calculated from the absorbance.

Supplementary information

Surface modifications of mFLAME for control experiments.

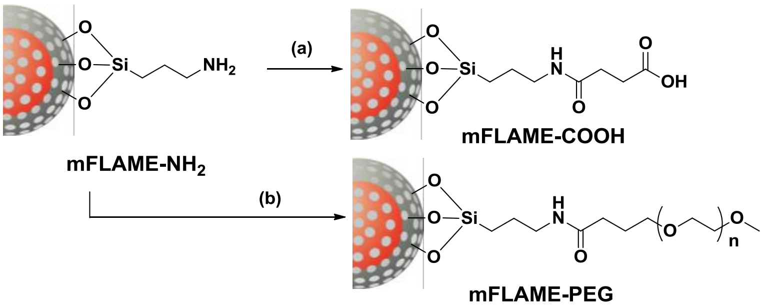

Scheme S1. Synthetic scheme of mFLAME-COOH and mFLAME-PEG. (a) Succinic anhydride, DMF, TEA; (b) methoxy-PEG-$(CH_2)_5$-COO-NHS (MW 5000), TEA, DMF.

Preparation of mFLAME-COOH. mFLAME-NH_2 dispersed in dry DMF (1.0 mL) was added slowly to a flask containing 2.0 M succinic anhydride in dry DMF under Ar atmosphere. Anhydrous TEA was added to the mixture, which was stirred at 40°C for 24 h. The product was separated by centrifugation (14,000 × *g*, 4°C, 30 min) and washed three times with DMF (3.0 mL) and water (3.0 mL). Finally, mFLAME-COOH nanoparticles were dispersed in 3 mL of water.

Preparation of mFLAME-PEG. The mFLAME-NH_2 dispersed in 10 mL of dried DMF was heated to 40°C while stirring. Then, methoxy-PEG-$(CH_2)_5$-COO-NHS (0.40 g) and dried TEA (50 μL) were added to the resulting solution and stirred for 2 days under Ar atmosphere. The resulting materials were washed with DMF and H_2O three times (14,000 × *g*, 30 min). mFLAME-PEG was dispersed in 5 mL of H_2O.

Table S1. ζ-Potential values and hydrodynamic diameters of the PFCE emulsion and mFLAMEs.

Materials	Hydrodynamic diameter/nm	ζ-Potential/mV
mFLAME-COOH	121 ± 5	-55.1 ± 2.3
mFLAME-PEG	125 ± 6	-20.5 ± 2.1

Fluorescent probe, FITC-FA, for folate receptors

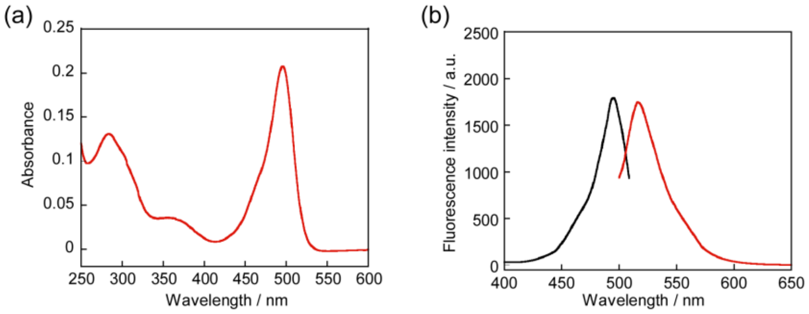

Figure S1. (a) Absorption spectra of FITC-FA (7.5 µM) in 200 mM PBS (pH 7.4). (b) Emission and excitation spectra of FITC-FA (750 nM) in 200 mM PBS (pH 7.4). Ex_{max}: 496 nm, Em_{max}: 517 nm.

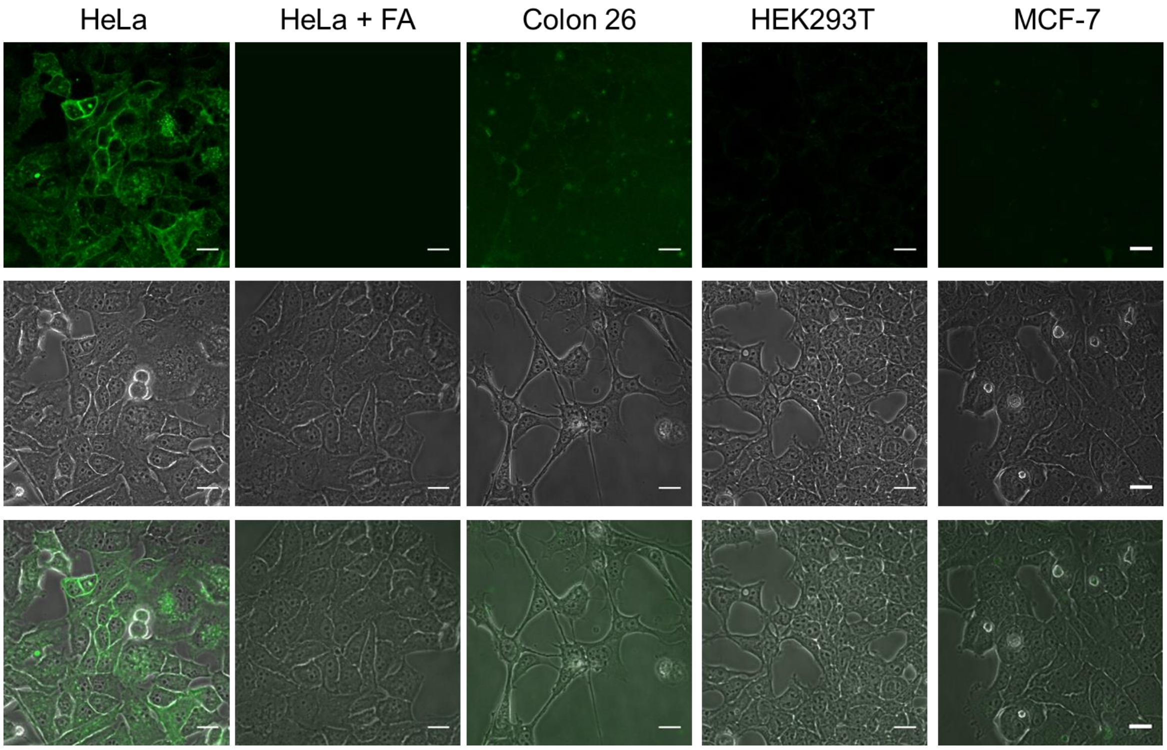

Figure S2. Fluorescence imaging of HeLa, colon26, and HEK293T, MCF-7 cells treated with FITC-FA (5 µM) for 30 min. Scale bar is 20 µm.

Folate receptors were also over-expressing on the HeLa cells, however, the expression levels of folate receptors on KB cells were higher than that on HeLa cells.

Fluorescence imaging of cells treated with mFLAMEs for 7 h.

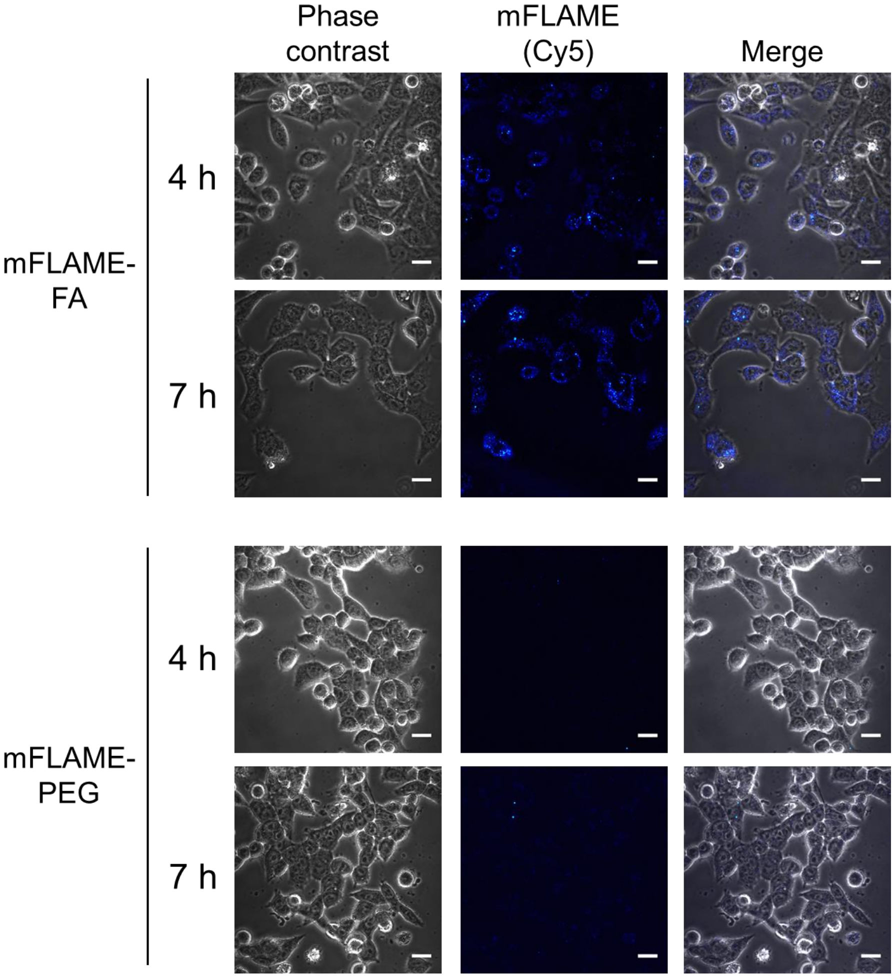

Figure S3. Confocal laser scanning microscopy images of KB cells incubated with mFLAME-FA or mFLAME-PEG for 4 h or 7 h. Measurement condition: Cy5 was excited at 635 nm and detected at 660–760 nm. Scale bar: 10 µm.

Fluorescent imaging revealed that cellular uptake of mFLAME-FA was increased in the time-dependent manner.

Fluorescence imaging of anti-cancer drug, DOX

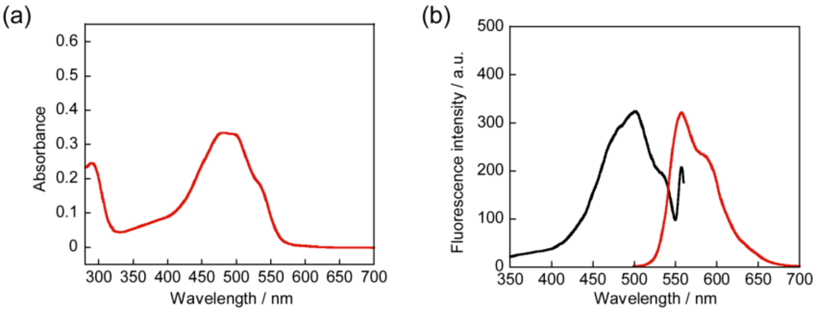

Figure S4. (a) Absorption spectra of DOX (30 μM) in 100 mM HEPES (pH 7.4). (b) Emission and excitation spectra of FITC-FA (3 μM) in 100 mM HEPES (pH 7.4). Ex_{max}: 448 nm, Em_{max}: 557 nm.

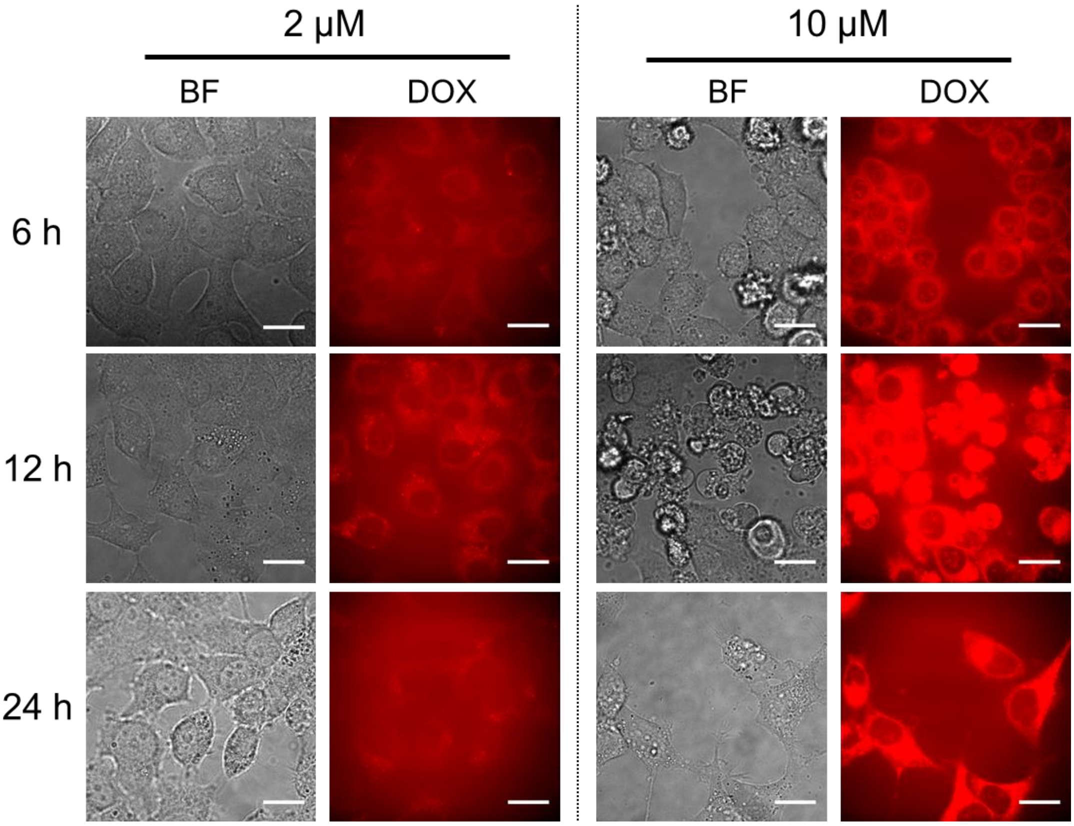

Figure S5. Fluorescence imaging of KB cells incubated with DOX (2 or 10 μM) for 6, 12, or 24 h. Scale bar: 20 μM.

References

1. Chan, K. W. Y.; Liu, G.; Song, X.; Kim, H.; Yu, T.; Arifin, D. R.; Gilad, A. a; Hanes, J.; Walczak, P.; van Zijl, P. C. M.; Bulte, J. W. M.; McMahon, M. T. *Nat. Mater.* **2013**, *12*, 268–275.
2. Johnson, T. D.; Christman, K. L. *Expert Opin. Drug Deliv.* **2013**, *10*, 59–72.
3. Li, H.; He, X.; Kang, Z.; Huang, H.; Liu, Y.; Liu, J.; Lian, S.; Tsang, C. H. A.; Yang, X.; Lee, S.-T. *Angew. Chem. Int. Ed.* **2010**, *49*, 4430–4434.
4. Mitragotri, S.; Lahann, J. *Adv. Mater.* **2012**, *24*, 3717–3723.
5. Kelkar, S. S.; Reineke, T. M. *Bioconjug. Chem.* **2011**, *22*, 1879–903.
6. Janib, S. M.; Moses, A. S.; MacKay, J. A. *Adv. Drug Deliv. Rev.* **2010**, *62*, 1052–1063.
7. Torchilin, V. P. *Adv. Drug Deliv. Rev.* **2006**, *58*, 1532–1555.
8. Li, Y.; Qian, Y.; Liu, T.; Zhang, G.; Liu, S. *Biomacromolecules* **2012**, *13*, 3877–3886.
9. Yue-Jian, C.; Juan, T.; Fei, X.; Jia-Bi, Z.; Ning, G.; Yi-Hua, Z.; Ye, D.; Liang, G. *Drug Dev. Ind. Pharm.* **2010**, *36*, 1235–1244.
10. Gabizon, A. A. *Clin. Cancer Res.* **2001**, *7*, 223–225.
11. Silindir, M.; Erdoğan, S.; Özer, a Y.; Doğan, a L.; Tuncel, M.; Uğur, Ö.; Torchilin, V. P. *J. Liposome Res.* **2013**, *23*, 20–27.
12. Li, S.; Goins, B.; Zhang, L.; Bao, A. *Bioconjug. Chem.* **2012**, 23, 1322–1332.
13. Zhu, L.; Kate, P.; Torchilin, V. P. *ACS Nano* **2012**, *6*, 3491–3498.
14. Cho, H.; Bae, J.; Garripelli, V. K.; Anderson, J. M.; Jun, H.-W.; Jo, S. *Chem. Commun.* **2012**, 6043–6045.
15. Zhu, C.; Liu, L.; Yang, Q.; Lv, F.; Wang, S. *Chem. Rev.* **2012**, *112*, 4687–4735.
16. Wen, S.; Li, K.; Cai, H.; Chen, Q.; Shen, M.; Huang, Y.; Peng, C.; Hou, W.; Zhu, M.; Zhang, G.; Shi, X. *Biomaterials* **2013**, *34*, 1570–1580.
17. Zong, H.; Thomas, T. P.; Lee, K.-H.; Desai, A. M.; Li, M.; Kotlyar, A.; Zhang, Y.; Leroueil, P. R.; Gam, J. J.; Banaszak Holl, M. M.; Baker, J. R. *Biomacromolecules* **2012**, *13*, 982–991.
18. Luo, K.; Liu, G.; She, W.; Wang, Q.; Wang, G.; He, B.; Ai, H.; Gong, Q.; Song, B.; Gu, Z. *Biomaterials* **2011**, *32*, 7951–7960.
19. Qin, T.; Wiedemair, W.; Nau, S.; Trattnig, R.; Sax, S.; Winkler, S.; Vollmer, A.; Koch, N.; Baumgarten, M.; List, E. J. W.; Müllen, K. *J. Am. Chem. Soc.* **2011**, *133*, 1301–1303.
20. Amir, R. J.; Albertazzi, L.; Willis, J.; Khan, A.; Kang, T.; Hawker, C. J. *Angew. Chem. Int. Ed.* **2011**, *50*, 3425–3429.

21. Ferris, D. P.; Lu, J.; Gothard, C.; Yanes, R.; Thomas, C. R.; Olsen, J.-C.; Stoddart, J. F.; Tamanoi, F.; Zink, J. I. *Small* **2011**, *7*, 1816–1826.
22. Lee, J. E.; Lee, N.; Kim, H.; Kim, J. J. H.; Choi, S. H.; Kim, T.; Song, I. C.; Park, S. P.; Moon, W. K.; Hyeon, T. *J. Am. Chem. Soc.* **2010**, *132*, 552–557.
23. Yang, X.; Li, Z.; Li, M.; Ren, J.; Qu, X. *Chem. Eur. J.* **2013**, *19*, 15378–15383.
24. Zhang, X.; Zhang, X.; Wang, S.; Liu, M.; Zhang, Y.; Tao, L.; Wei, Y. *Chem. Eur. J.* **2013**, *5*, 1943–1947.
25. Kim, T.; Momin, E.; Choi, J.; Yuan, K.; Zaidi, H.; Kim, J.; Park, M.; Lee, N.; McMahon, M. T.; Quinones-Hinojosa, A.; Bulte, J. W. M.; Hyeon, T.; Gilad, A. A. *J. Am. Chem. Soc.* **2011**, *133*, 2955–2961.
26. Hsiao, J.-K.; Tsai, C.-P.; Chung, T.-H.; Hung, Y.; Yao, M.; Liu, H.-M.; Mou, C.-Y.; Yang, C.-S.; Chen, Y.-C.; Huang, D.-M. *Small* **2008**, *4*, 1445–1452.
27. Taylor, K. M. L.; Kim, J. S.; Rieter, W. J.; An, H.; Lin, W.; Lin, W. *J. Am. Chem. Soc.* **2008**, *130*, 2154–2155.
28. Chen, Y.; Chen, H.; Zeng, D.; Tian, Y.; Chen, F.; Feng, J.; Shi, J. *ACS Nano* **2010**, *4*, 6001–6013.
29. Rosenholm, J. M.; Mamaeva, V.; Sahlgren, C.; Lindén, M. *Nanomedicine* **2012**, *7*, 111–120.
30. Lu, J.; Liong, M.; Zink, J. I.; Tamanoi, F. *Small* **2007**, *3*, 1341–1346.
31. Chen, Y.; Chen, H.; Zhang, S.; Chen, F.; Zhang, L.; Zhang, J.; Zhu, M.; Wu, H.; Guo, L.; Feng, J.; Shi, J. *Adv. Funct. Mater.* **2011**, *21*, 270–278.
32. Wu, S.-H.; Mou, C.-Y.; Lin, H.-P. *Chem. Soc. Rev.* **2013**, *42*, 3862–3875.
33. Vivero-Escoto, J. L.; Huxford-Phillips, R. C.; Lin, W. *Chem. Soc. Rev.* **2012**, *41*, 2673–2685.
34. Hoffmann, F.; Cornelius, M.; Morell, J.; Fröba, M. *Angew. Chem. Int. Ed.* **2006**, *45*, 3216–3251.
35. Wan, Y.; Zhao, D. *Chem. Rev.* **2007**, *107*, 2821–2860.
36. Slowing, I. I.; Trewyn, B. G.; Giri, S.; Lin, V. S.-Y. *Adv. Funct. Mater.* **2007**, *17*, 1225–1236.
37. Vivero-Escoto, J. L.; Slowing, I. I.; Trewyn, B. G.; Lin, V. S.-Y. *Small* **2010**, *6*, 1952–1967.
38. Wang, S. *Microporous Mesoporous Mater.* **2009**, *117*, 1–9.
39. Jasanoff, A. *Curr. Opin. Neurobiol.* **2007**, *17*, 593–600.
40. Weissleder, R.; Moore, A.; Mahmood, U.; Bhorade, R.; Benveniste, H.; Chiocca, E. A.; Basilion, J. P. *Nat. Med.* **2000**, *6*, 351–355.
41. Srinivas, M.; Boehm-Sturm, P.; Figdor, C. G.; de Vries, I. J.; Hoehn, M.

Biomaterials **2012**, *3*3, 8830–8840.

42. Díaz-López, R.; Tsapis, N.; Fattal, E. *Pharm. Res.* **2010**, *27*, 1–16.
43. Partlow, K. C.; Chen, J.; Brant, J. A.; Neubauer, A. M.; Meyerrose, T. E.; Creer, M. H.; Nolta, J. A.; Caruthers, S. D.; Lanza, G. M.; Wickline, S. A. *FASEB J.* **2007**, *21*, 1647–1654.
44. Ruiz-Cabello, J.; Barnett, B. P.; Bottomley, P. A.; Bulte, J. W. M. *NMR Biomed.* **2011**, *2*, 114–129.
45. Matsushita, H.; Mizukami, S.; Sugihara, F.; Nakanishi, Y.; Yoshioka, Y.; Kikuchi, K. *Angew. Chem. Int. Ed*. **2014**, *53*, 1008–1011.
46. Mason, R. P.; Antich, P. P.; Babcock, E. E.; Gerberich, J. L.; Nunnally, R. L. *Magn. Reson. Imaging* **1989**, *7*, 475–485.
47. Flögel, U.; Ding, Z.; Hardung, H.; Jander, S.; Reichmann, G.; Jacoby, C.; Schubert, R.; Schrader, J. *Circulation* **2008**, *118*, 140–148.
48. Ahrens, E. T.; Flores, R.; Xu, H.; Morel, P. A. *Nat. Biotechnol.* **2005**, *23*, 983–987.
49. Soulard, M.; Werner, A.; Zana, R. *Langmuir* **2000**, *16*, 9049–9057.
50. Union, I.; Pure, O. F.; *Chemistry, A. Pure Appl. Chem.* **1985**, *57*, 603–619.
51. Sega, E. I.; Low, P. S. *Cancer Metastasis Rev.* **2008**, *27*, 655–664.
52. Chen, C.; Ke, J.; Zhou, X. E.; Yi, W.; Brunzelle, J. S.; Li, J.; Yong, E.-L.; Xu, H. E.; Melcher, K. *Nature* **2013**, *500*, 486–489.
53. Salazar, M. D.; Ratnam, M. *Cancer Metastasis Rev.* **2007**, *26*, 141–152.
54. Zhang, C.; Gao, S.; Jiang, W.; Lin, S.; Du, F.; Li, Z.; Huang, W. *Biomaterials* **2010**, *31*, 6075–6086.
55. Ke, C.-Y.; Mathias, C. J.; Green, M. A. *Nucl. Med. Biol.* **2003**, *30*, 811–817.
56. Schroeder, J. E.; Shweky, I.; Shmeeda, H.; Banin, U.; Gabizon, A. *J. Control. Release* **2007**, *124*, 28–34.
57. Choi, H.; Choi, S. R.; Zhou, R.; Kung, H. F.; Chen, I.-W. *Acad. Radiol.* **2004**, *11*, 996–1004.
58. Hickman, J. A. *Cancer Metastasis Rev*. **1992**, *11*, 121–139.
59. Son, K. J.; Yoon, H.-J.; Kim, J.-H.; Jang, W.-D.; Lee, Y.; Koh, W.-G. *Angew. Chem. Int. Ed.* **2011**, *50*, 4782–4789.
60. Shen, B.; Jeon, J.; Palner, M.; Ye, D.; Shuhendler, A.; Chin, F. T.; Rao, J. *Angew. Chem. Int. Ed.* **2013**, *52*, 10511–10514.
61. Casey, J. R.; Grinstein, S.; Orlowski, J. *Nat. Rev. Mol. Cell Biol.* **2010**, *11*, 50–61.
62. York, N.; Thomas, J. A.; Buchsbaum, R. N.; Zimniak, A.; Racker, E. *Biochemistry* **1979**, *18*, 2210–2218.

Conclusion and Perspective

In conclusions, the author developed that several ^{19}F MRI probes and confirmed their usefulness for biomedical applications.

First, the author developed PRE-based ^{19}F MRI probes for monitoring gene expression via activity of reporter enzymes such as β-gal and β-lac. In particular, the author developed a ^{19}F MRI detection system with a specific probe for β-lac and cell-surface displayed β-lac to monitor gene expression in living cells. To the best of my knowledge, this is the first report to describe the ^{19}F MRI detection of gene expression in living cells.

In Chapter 2, the author successfully developed novel contrast agents with a core-shell structure, FLAMEs, for highly sensitive ^{19}F MRI. With a surface coating of silica, FLAMEs demonstrated practical properties such as chemical surface modifiability, dispersibility in water, biocompatibility, and high stability. FLAMEs were proven to be useful ^{19}F MRI contrast agents to overcome two major limitations of current ^{19}F MRI probes, i.e., impractical surface modification of nanoemulsions and low sensitivity of small-molecule-based probes. The author demonstrated that the ^{19}F MRI technique using FLAMEs was useful for monitoring biological phenomena such as gene expression and tumors. These biological applications represent only a fraction of the forthcoming applications. The author believes that this innovative technology can be used for biomedical in vivo imaging of diseased tissues such as atherosclerosis plaques with clot-binding peptides and bone neoplasms with bisphosphonate.

In Chapter 3, the author combined PRE-based probe design strategy with FLAME for development of a stimulus-responsive ^{19}F MRI nanoprobe for in vivo applications. To demonstrate this concept, reduction-responsive ^{19}F MRI nanoprobes with disulfide linkers were synthesized. The T_2 of nanoprobes was increased drastically by the reductive reaction, resulting in recovery of the ^{19}F MRI signal. The author believes that a PRE-based nanoprobe design strategy could lead to the development of an ^{19}F MRI nanoprobe for activity of hydrolases neutrophili elastase, cathepsin, and caspase, which play a role in various autoimmune phenomena.

In Chapter 4, the author has described a novel drug carrier, mFLAME, consisting of a PFCE core and a mesoporous silica shell. The silica shell of mFLAME has various practical properties such as dispersibility in water, chemical surface modifiability, biocompatibility, and efficient drug loading and releasing capacity. The author demonstrated the dual-mode sensing of folate receptor-mediated cellular uptake by ^{19}F MRI and fluorescence microscopy. In addition, drug-doped mFLAME-FA exhibited cellular uptake and drug release efficacy toward folate receptor over-expressing tumor cells. In the near future perspectives, mFLAME should be tested in tumor-bearing mice to achieve simultaneous in vivo analysis of drug efficacy and the bio-distribution. The combination of mFLAMEs and the stimulus-responsive capping strategy should lead to innovative drug carriers that control drug release and ^{19}F MRI signal intensity. For example, SPIO would be attached to mFLAMEs as the gate keepers of mesopores and quenchers for ^{19}F MRI signals of mFLAME. SPIO has not only the ability to prevent drug leakage from mesopores but also strong T_2 relaxivity for NMR signals. The author believes that mFLAME is therefore a fundamental technology for next-generation smart biomaterials to provide promising theragnostic approaches.

Appendix

Development of Enzyme-responsive Nanocarrier for ^{19}F MRI and Drug Release

Introduction

Stimuli-responsive mesoporous silica nanoparticles have great potential for useful applications in biomedicine due to their unique responsiveness and high stability.[1] In particular, these nanocarriers equipped with gatekeepers are enormously appealing not only as sensor but also as drug delivery vehicles. A variety of stimuli-responsive gatekeepers have been introduced onto the surface of mesoporous silica shell to control the release of guest molecules in response to external stimuli, such as pH,[2] light,[3] and redox potential.[4] Although these systems have been investigated as controlled release systems or potential drug delivery vehicles, the author still needs to optimize their performances such as stability and enhanced sensitivity to external stimuli to expand their potentials in variety of area.

Design and synthesis of SPIO-encapsulated mesoporous silica nanoparticle with β-cyclodextrin capping

The author designed a drug carrier consisting of a mesoporous silica nanoparticle that involves superparamagnetic iron oxide nanoparticles (SPM). Superparamagnetic iron oxide nanoparticles have the strong T_2 relaxavity for the NMR signal.[5–8] Therefore, ^{19}F MRI signal of ^{19}F-containing functional compounds in SPM would be quenched. In addition, cyclodextrin would be attached to the surface of silica shell as the gatekeepers of mesopores and responsiveness to α-amylase.[9] The torous shaped cyclodextrin was initially chosen to block the porous channel of SPM. The cyclodexrtin moiety of the

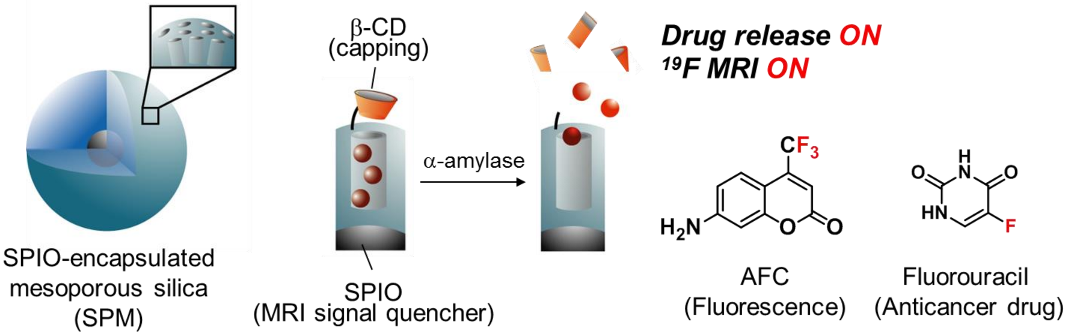

Figure 1. Cyclodextrin capped SPM and control of ^{19}F MRI signal and drug release by α-amlyase.

gatekeeper can be hydrolysed by α-amylase to exhibit enzyme-responsive characteristics in the release of guest. Thus, ^{19}F MRI signal intensity and drug release of cyclodextrin-capped SPM including ^{19}F-containing compounds should be controlled by α-amylase activity.

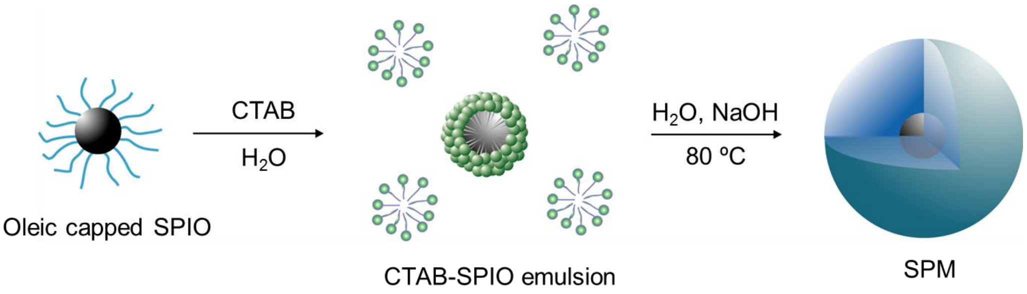

Scheme 1. Preparation of SPM.

The schematic preparation processs of SPM was represented in Scheme 1. The oleic capped superparamagnetic iron oxide was prepared by thermal decomposition of iron-oleate complexes in a solution of oleic acid surfactants and octadecene solvent.[10,11] The average diameter of the particles was 11 ± 2 nm, which was calculated from the TEM images (n = 50). The hydrophobic iron oxide nanoparticles dissolved in chloroform were transferred to the water phase by mixing them with an aqueous CTAB solution and evaporating the organic solvent. Using this method, the hydrophobic tail of the CTAB surfactant interacts strongly with the hydrophobic oleate ligand on the surface of the oleate-capped iron oxide, and the hydrophilic charged headgroup of CTAB makes the hydrophobic iron oxide nanoparticles water soluble. The TEOS was added into the aqueous solution containing CTAB-coated iron oxide nanoparticle, CTAB, and sodium hydroxide to yield SPM nanoparticle. The SPIO-encapsulating and mesopore structures of SPM were clearly observed by TEM.

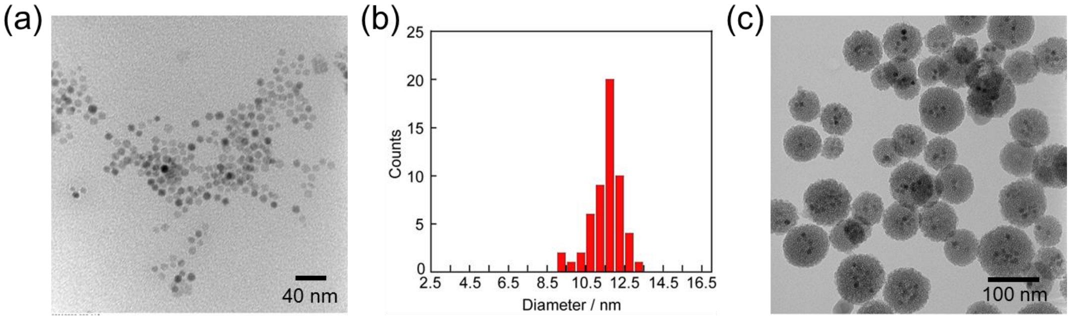

Figure 2. (a) TEM image of oleate-capped iron oxide (b) Particle size distribution histogram calculated from TEM images (c) TEM images of SPM.

Then, cyclodextrin-capped SPM was prepared as shown Scheme 2. Cyclodextrin was introduced into the surface of SPM in the presence of AFC (Figure 1), which is fluorine-containing fluorescent molecule, to accumulate in the mesopore of SPM.

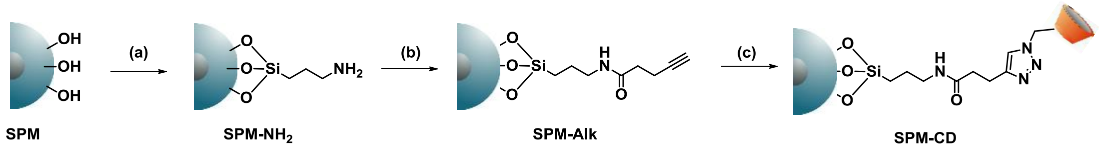

Scheme 2. Synthetic route to SPM-CD (a) 3-APTES, 2-propanol; (b) Alk-NHS, TEA, DMF; (c) AFC, β-CD-N_3, $CuSO_4$, Sodium ascorbate.

Table 1. ζ-Potential values and hydrodynamic diameters of SPM nanoparticles.

Materials	Hydrodynamic diameter (nm)	ζ-Potential (mV)
SPM	145 ± 5	-17.1 ± 0.3
SPM-NH_2	167 ± 2	9.6 ± 1.1
SPM-Alk	159 ± 6	-3.4 ± 0.8
SPM-CD	142 ± 4	-42.0 ± 3.5

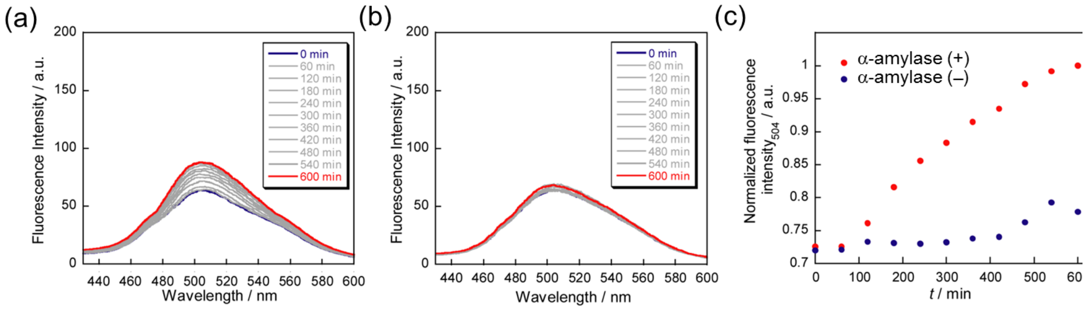

Figure 3. Time dependent emission of SPM-CD in presence of α-amylase (a) or in the absence of α-amylase (b). (c) Change of fluorescence intensity at 517 nm with time. Condition: HEPES buffer (pH 7.4, 10 mM), 3% DMSO.

Then, α-amylase was used as external stimulus to trigger the enzyme-responsive of AFC in order to investigate the controlled release behaviour of SPM-CD. Encapsulated-AFC was released gradually from SPM-CD with 10 hours after addition of α-amylase, thus suggesting a good response to α-amylase (Figure 3). This result shows that the cyclodextrin capping were broken, thus leading to a drug release to α-amylase.

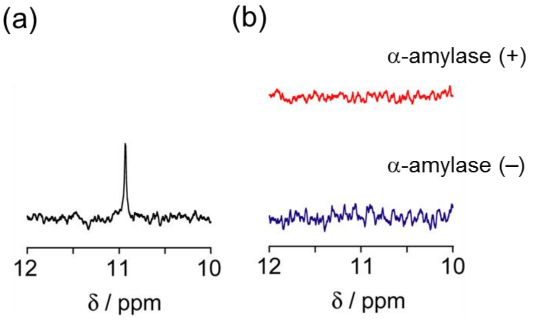

Figure 4. (a) ^{19}F NMR spectrum of AFC (b) ^{19}F NMR spectra of SPM-CD in the presence or absence of α-amylase.

Next, SPM-CD treated with α-amylase were analysed by ^{19}F NMR. However, no ^{19}F NMR signal was detected from the solution including SPM because of low loading amount of AFC in mesopore.

Experimental section

Materials and instruments. General chemicals were of the highest grade available, supplied by Tokyo Chemical Industries, Wako Pure Chemical, and Aldrich Chemical Co., and used without further purification. NMR spectra were measured on a JEOL JNM-AL 400 instrument at 400 MHz for ^{1}H, at 100.4 MHz for ^{13}C NMR using tetramethylsilane as an internal standard, and at 376 MHz for ^{19}F NMR using sodium trifluoroacetate as an internal standard. Mass spectra were taken on a JEOL JMS-DX for fast atom bombardment and on a Waters LCT-Premier XE for ESI. Fluorescence spectra were recorded using a Hitachi F4500 spectrometer. The slit width was 5.0 nm for both excitation and emission. The photomultiplier voltage was 700 V. TEM images were acquired by using the HITACHI H-9000 (300 V). Particle size distribution and ζ-potential were measured by DLS on the particle analyzer nano partica SZ-100 from HORIBA.

Synthesis of iron-oxide nanoparticle. The iron oxide nanoparticles were synthesized by the thermal decomposition of iron-oleate complexes in a solution of oleic acid surfactants and octadecene solvent. First, 2.2 g of iron trichloride hexahydrate and 7.4 g of sodium oleate were dissolved in a mixture of 16.3 mL of absolute ethanol and 12.2 mL of water and mixed with 28.5 mL of hexane. The solution was refluxed for 4 h. The mixture was then washed with water several times in a separatory funnel, and the hexane was removed from the mixure by evaporation. The synthesized iron-oleate complex was then dried under vacuum overnight. 1.0 g of the iron-oleate complex was dissolved in a solution of 177 μL of oleic acid and 7.1 mL of octadecene. The mixture was stirred under argon flow at room temperature. After 30 min, the reaction solution was heated to 320°C at a rate of 5°C min^{-1}, and kept at that temperature for 1 hour. After the mixture had cooled to room temperature, 5 mL of hexane was added, and the nanoparticles were precipitated by adding of an excess of ethanol. The nanoparticles were then washed twice in a solution of 1:3 hexane-ethanol and dried under vacuum.

Synthesis of SPM. 0.5 mL of the iron-oxide nanoparticle (6.7 mg mL^{-1}) in chloroform was poured into 5 mL of 0.055 M aqueous CTAB solution and the resulting solution was stirred vigorously for 30 min. The formation of oil-in-water microemulsion resulted in a turbid brown solution. Then, the mixture was heated up to 60°C and aged at that temperature for 10 min under stirring to evaporate the chloroform, resulting in a transparent black iron oxide/CTAB solution. The resulting solution was added to a mixture of 45 mL of water and 0.3 mL of 2 M NaOH solution and the mixture was heated up to 70°C under stirring. Then, 0.5 mL of TEOS was added and the solution was stirred for 3 h. The synthesized SPM nanoparticles were washed three times with ethanol to remove the unreacted species and dispersed in 20 mL of ethanol.

Synthesis of SPM-NH_2. The SPM dispersed in isopropanol (40 mL) was heated to 80°C while stirring. Then, APTES (200 μL) was slowly added into the resulting solution and stirred for 4 h under Ar. The resulting materials were washed with ethanol three times. The CTAB surfactants were removed from the mesoporous silica nanoparticles by dispersing the SPM-NH_2 in a solution of ammonium nitrate (160 mg) and 95% ethanol (60 mL) and heating the mixture at 60°C for 1 h. The resulting materials were centrifuged (14,000 × *g*, 30 min) and washed with ethanol three times. SPM-NH_2 was dispersed in 20 mL of DMF.

Synthesis of SPM-Alk. SPM-NH_2 dispersed in dry DMF (1.0 mL) was added slowly to a flask containing Alk-NHS in dry DMF under Ar atmosphere. Anhydrous TEA was added to the mixture, which was stirred at 40°C for 24 h. The product was separated by centrifugation (14,000 × *g*, 4°C, 30 min) and washed three times with DMF (3.0 mL) and water (3.0 mL). Finally, SPM-Alk nanoparticles were dispersed in 3 mL of water.

Synthesis of SPM-CD. SPM-Alk nanoparticles were dispersed in 100 mM PBS containing 30% DMF and AFC (1 mM), and stirred for 24 h. Then, β-CD-N_3 (34 mg) $CuSO_4 \cdot 5H_2O$ (30 mg), and Sodium ascorbate (40 mg) were added to the mixture, which was stirred at RT for 48 days. The product was separated by centrifugation (14,000 × *g*, 4°C, 30 min) and washed three times with DMF (3.0 mL) and water (3.0 mL). Finally, AFC-loaded SPM-Alk nanoparticles were dispersed in 2.0 mL of water.

References

1. Lu, J.; Liong, M.; Zink, J. I.; Tamanoi, F. *Small* **2007**, *3*, 1341–1346.
2. Lee, C.-H.; Cheng, S.-H.; Huang, I.-P.; Souris, J. S.; Yang, C.-S.; Mou, C.-Y.; Lo, L.-W. *Angew. Chem. Int. Ed.* **2010**, *49*, 8214–8219.
3. Park, C.; Lee, K.; Kim, C. *Angew. Chem. Int. Ed*. **2009**, *48*, 1275–1278.
4. Luo, Z.; Cai, K.; Hu, Y.; Zhao, L.; Liu, P.; Duan, L.; Yang, W. *Angew. Chem. Int. Ed.*

2011, *50*, 640–643.

5. Kato, Y.; Artemov, D. *Magn. Reson. Med*. **2009**, *61*, 1059–1065.
6. Wang, H.; Wang, S.; Liao, Z.; Zhao, P.; Su, W.; Niu, R.; Chang, J. *Int. J. Pharm.* **2012**, *430*, 342–349.
7. Li, Q.; Tang, G.; Xue, S.; He, X.; Miao, P.; Li, Y.; Wang, J.; Xiong, L.; Wang, Y.; Zhang, C.; Yang, G.-Y. *Biomaterials* **2013**, *34*, 4982–4992.
8. Lee, J. E.; Lee, N.; Kim, H.; Kim, J. J. H.; Choi, S. H.; Kim, T.; Song, I. C.; Park, S. P.; Moon, W. K.; Hyeon, T. *J. Am. Chem. Soc.* **2010**, *132*, 552–557.
9. Park, C.; Kim, H.; Kim, S.; Kim, C. *J. Am. Chem. Soc.* **2009**, *131*, 16614–16615.
10. Lynch, J.; Zhuang, J.; Wang, T.; LaMontagne, D.; Wu, H.; Cao, Y. C. *J. Am. Chem. Soc*. **2011**, *133*, 12664–12674.
11. Park, J.; An, K.; Hwang, Y.; Park, J.-G.; Noh, H.-J.; Kim, J.-Y.; Park, J.-H.; Hwang, N.-M.; Hyeon, T. *Nat. Mater*. **2004**, *3*, 891–895.

List of publications

1. ^{19}F MRI Detection of β-Galactosidase Activity for Imaging of Gene Expression
   S. Mizukami, **H. Matsushita**, R. Takikawa, F, Sugihara, M. Shirakawa, and K. Kikuchi
   Chem. Sci. **2011**, *2*, 1151–1155. DOI 10.1039/clsc00071c
2. ^{19}F MRI monitoring of Gene Expression in Living Cells via Cell Surface β-Lactamase Activity
   H. Matsushita, S. Mizukami, Y. Mori, F, Sugihara, M. Shirakawa, Y. Yoshioka, and K. Kikuchi
   ChemBioChem **2012**, *13*, 1579–1583. DOI 10.1002/cbic.201200331
3. Multifunctional Core-shell Silica Nanoparticles for Highly Sensitive ^{19}F Magnetic Resonance Imaging
   H. Matsushita, S. Mizukami, F, Sugihara, Y. Nakanishi, Y. Yoshioka, and K. Kikuchi
   Angew. Chem. Int. Ed. **2014**, *53*, 1008–1011. DOI 10.1002/anie.201308500

4. Mesoporous Silica Nanoparticles for ^{19}F Magnetic Resonance Imaging, Fluorescence Imaging, and Drug Delivery
   H. Matsushita, F, Sugihara, Y. Yoshioka, S. Mizukami, and K. Kikuchi
   In preparation.
5. Gadolinium based-^{19}F MRI Nanoprobe for Monitoring Reducing Species
   H. Matsushita, F, Sugihara, T. Nakamura, Y. Yoshioka, S. Mizukami, and K. Kikuchi
   In preparation.

Presentations at International Conferences

1. ○**Matsushita, H.**; Mizukami, S.; Sugihara, F.; Shirakawa, M.; Kikuchi, K. "Development of ^{19}F MRI Probes for Imaging Gene Expression" World Molecular Imaging Congress (Kyoto, Japan, September 2010).
2. ○**Matsushita, H.**; Mizukami, S., and Kikuchi, K., "^{19}F MRI Probes for Imaging Gene Expression", 2010 International Chemical Congress of Pacific Basin Societies (Hawaii, USA, December, 2010)
3. ○**Matsushita, H.**; Mizukami, S.; Sugihara, F.; Shirakawa, M.; Kikuchi, K. "Development of ^{19}F MRI Probes for Imaging Gene Expression" Imaging in 2020

Bridging Molecular Imaging and Therapy (Wyoming, U.S.A. September 2011)

4. ○**<u>Matsushita, H.</u>**; Mizukami, S.; Sugihara, F.; Shirakawa, M.; Kikuchi, K. "Development of ^{19}F MRI Probes for Imaging Gene Expression" JSPS Sweden-Japan Joint Colloquium Direct imaging in Bio/Medical science (Lund, Sweden, January 2011).
5. ○**<u>Matsushita, H.</u>**; Mizukami, S.; Mori, Y.; Sugihara, F.; Shirakawa, M., Yoshioka, Y.; Kikuchi, K. "Development of ^{19}F MRI Probes for Imaging Gene Expression" The 11th Global COE international Symposium:Bio-Environmental Chemistry (Osaka, Japan, December 2011).
6. ○**<u>Matsushita, H.</u>**; Mizukami, S.; Sugihara, F.; Shirakawa, M.; Kikuchi, K. "Development of ^{19}F MRI Probes for Imaging Gene Expression" Bioorganic Chemistry Gordon Research Conference (New Hampshire, U.S.A. June 2012)
7. ○**<u>Matsushita, H.</u>**; Mizukami, S.; Sugihara, F.; Shirakawa, M.; Kikuchi, K. "Development of ^{19}F MRI Probes for Monitoring Gene Expression and Tumor Detection" Towards Comprehensive Understanding of Immune Dynamism 2012 (Osaka, Japan October, 2012)

Awards

1. The 11th Global COE international Symposium: Bio-Environmental Chemistry, *Best Presentation Award* (**2011**).

Acknowledgements

The author is most grateful to Professor Kazuya Kikuchi for his continuous guidance, support, and encouragement throughtout this study. The author expresses his sincere thanks to Dr. Shin Mizukami for his valuable guidance and discussion. The author also expresses his cordial thanks to Dr. Yuichiro Hori, Dr. Toshiyuki Kowada, Dr. Yuko Kamikawa, and Dr. Masafumi Minoshima for their kind help and valuable discussions.

The author is deeply grateful to Professor Yoshioka Yoshioka and Dr. Yuki Mori at Osaka University for support in MRI measurements. The author his sincerely thanks to Dr. Fuminori Sugihara at Osaka University for his technical support and valuable advice regard MRI measurements, in vivo animal experiments, TEM measurements and Flow cytometer analysis. The author expresses his gratitude to Dr. Takao Sakata and the Research Center for Ultra-High Votage Electron Microscopy at Osaka University for their support on the measurement of TEM. The author is grateful to Professor Nobuhito Imanaka and Dr. Toshiyuki Masui for their support on the measurement of N_2 absorption/desorption isotherm measurements. The author is also grateful to Professor Shirakawa Masashiro at Kyoto University for his valuable discussions.

The author would like to thank Professor Shunichi Fukuzumi and Professor Shinobu Ito for their helpful discussions and suggestions. The author also thanks all of the members of the Kikuchi laboratory for their kind help, teaching, and friendship.

The author acknowledges financial support from the Japan Society for the Promotion of Science (JSPS) for Young Scientists and the Global Centers of Excellence (GCOE) Program ‘‘Global Education and Research Center for Bio-Environment Chemistry’’ of Osaka University.

Finally, the author appreciates the tremendous support and continuous encouragement from his family and friends.

Osaka, Japan
January, 2014

Hisashi Matsushita

Division of Advanced Science and Biotechnology
Department of Materials and Life Science
Graduate School of Engineering, Osaka University